University of Bergen

Department of Physics and Technology

Measurement of the relative branching fraction $\mathscr{B}(B_s^0 \to \psi(2S)\phi)$ / $\mathscr{B}(\ B_s^0 \to\ J/\psi\phi)$ with the ATLAS experiment at $\sqrt{s} = 13$ TeV

Håkon Midthun Kolstø

Master's Thesis in Particle Physics
June 2018

Abstract

In this thesis we present the result of the relative branching fraction of the two hadronic B_s^0 modes $B_s^0 \to \psi(2S)\phi$ and $B_s^0 \to J/\psi\phi$. In order to guarantee identical topologies we only look at the modes where $J/\psi \to \mu^+\mu^-$, $\psi(2S) \to \mu^+\mu^-$ and $\phi \to K^+K^-$. The first observation of the rare decay of $B_s^0 \to \psi(2S)\phi$ was reported by the CDF collaboration at the Fermilab Tevatron in 2006 and the relative branching faction was reported to be $\mathscr{B}(B_s^0 \to \psi(2S)\phi)/\mathscr{B}(\ B_s^0 \to J/\psi\phi) = 0.52 \pm 0.13(\text{stat}) \pm 0.04(\text{syst}) \pm 0.06(\text{BR})$ [1]. This measurement was repeated by the D0 collaboration in 2009 and LHCb in 2012 measuring $0.53 \pm 0.10(\text{stat}) \pm 0.07(\text{syst}) \pm 0.06(\text{BR})$ [2] and $0.489 \pm 0.026(\text{stat}) \pm 0.021(\text{syst}) \pm 0.012(\text{BR})$ [3], respectively.

Looking at run-2 data from 2016 collected by the ATLAS detector at $\sqrt{s} = 13$ TeV, we present a measurement of the relative branching fraction of

$$\frac{\mathscr{B}(B_s^0 \to \psi(2S)\phi)}{\mathscr{B}(B_s^0 \to J/\psi\phi)} = 0.55 \pm 0.04(\text{stat}) \pm 0.09(\text{syst})$$

determined through the relative efficiency-corrected yields of the two decay modes and the world average branching fractions of the charmonium mesons to dimuons. Mass measurement of the B_s^0 has also been performed yielding $m_{B_s^0} = 5367.22 \pm 0.24(\text{stat}) \pm 1.92(\text{syst})$ MeV/c^2 being in well agreement with the current world average.

Acknowlegdements

First of all I would like to thank my supervisor Prof. Gerald Eigen for all the guidance throughout this thesis which has been of utmost importance. Thank you for sharing your expertise and experience with me - I am truly grateful.

Next on the list, Are Træet, thank you for all the technical information you provided me with in the start of this thesis - and for always having time for a question or two. Your help has been invaluable to me. Thank you.

To tired guys, Anders, Daniel, Helge, Karl, Magnus and Viljar, we could not have been more lucky. Thank you for making me wish that these five years would never come to an end.
My sincere appreciation goes to my family and friends. Thank you for always being so supportive and encouraging. You can't be thanked enough.
I would also like to thank Semen Turchikhin and Adam Barton from the B physics group at CERN for giving me important insights along the way.

Johanne, words quickly come to an end when describing my gratitude to you. All I can say is thank you. Thank you for being the most wonderful person in the world.

Contents

List of Figures

List of Tables

Chapter 1

Introduction

Motivation

All of us have been researchers at some point in life. We gaze towards the stars and contemplate trivial thoughts, which by no means have trivial solutions. At first sight, we considered only things, which we could see as part of our reality. Arguably, one would expect this true reality to be constituent of visible components, but our eyes can only see so much. As we kept the possibility of invisible matter open we sought this quest by improving our eyes and senses.

By the inherent curiosity embedded in us, we are forced to build machines several thousands of times heavier than ourselves - to probe the nature of these tiny invisible constituents. Such a machine is the ATLAS detector located at the European Organization for Nuclear Research (CERN) in Geneva, Switzerland.

Cogitating questions as *"why is there something, rather than nothing?"* may be demanding and can leave our head spinning. This particular question has been investigated extensively the last decades. In 1932 [9], the existence of antimatter was confirmed and questions regarding the asymmetry between the matter anti-matter abundance quickly emerged. Luckily for us, matter and antimatter are not exact mirror images of one another. If they were, however, I wouldn't be here to write - neither would you be to read.

The theoretical framework to describe this invisible world governing our universe is the known as the Standard Model (SM) of particle physics. The Standard Model actually predicts an asymmetry between matter and antimatter, but to an extent that is too small to explain the observed dissymmetry. One area in which the Standard model predicts such an asymmetry is in the B_s^0 meson sector. Neutral B-mesons can oscillate between their respective conjugate modes and the peculiar realization is that they are not mirror images of one another [10]. This dissym-

metry is encapsulated in the B_s^0 mixing phase $\phi_s^{J/\psi\phi}$[1]. Studies of rare decays like the $B_s^0 \to J/\psi\phi$ and $B_s^0 \to \psi(2S)\phi$ are directly linked to this mixing phase and can therefore provide important insight to the differences in the matter antimatter abundances.

The analysis presented in chapter 6 is performed by use of the ROOT libraries [12] and the scripts are mainly written in the object-oriented C++ programming language. We have performed a cut-based selection of candidates before optimizing the sensitivity $S/\sqrt{S+B}$ with respect to specific variables to further increase the signal to background ratio. Specific probability density functions (PDF) are fitted to data by maximizing likelihood functions from the Monte Carlo (MC) samples and are compared to the distributions seen in data. The analysis in chapter 7 is performed by data collected by the ATLAS experiment from 2016 in Run 2 at $\sqrt{s} = 13$ TeV.

[1] $\phi_s^{J/\psi\phi} \approx -2\arg(-V_{ts}V_{tb}^*/V_{cs}V_{cb}^*)$ [11] where V_{ij} are the Cabibbo–Kobayashi–Maskawa (CKM) matrix elements investigated in subsection 2.3.5.

Chapter 2

Standard Model

The Standard Model is today considered to be the most successful theory of physics. It describes the basic constituents of matter and the interactions between them, i.e. the forces. However, to this date, it fails to include gravity.

2.1 Origin of Particles

From an experimental view, the history of particles originates from the cathode ray experiment performed by J.J. Thomson in 1897 with the discovery of the negatively charged electron [13]. Of course, from a philosophical aspect, one could argue that the history of particles has its beginning from the Greeks with the famous atomist Democritus.

The discovery of the electron turned out to not only be the discovery of a new particle, but also the discovery of a truly fundamental subatomic particle - by definition, an *atom*[1]. Thomson's results showed that the electron was negatively charged and relatively light implying low mass-to-charge ratio. Further on, he deduced that this newly discovered particle was a fundamental constituent of the neutrally charged atom. Now two problems arose; what contributes to the additional mass and the positive charge to neutralize the atom?

In 1911 Rutherford came along with his scattering experiment where he fired charged α particles on a gold foil proving that the atom had most of its mass centered in a positively charged core - namely the *nucleus* [14]. The nucleus of the lightest atom, i.e. hydrogen, was named *proton* by Rutherford. Three years later, Bohr proposed a model where the negatively charged electron orbited the positively charged proton - like a planet orbiting the sun where gravity was now interchanged with the much alike Coulomb force. A problem arose when applying this model to

[1]Atom has its name from *atomos* which in Greek means something truly indivisible

heavier atoms. For instance, the helium atom should account for a mass twice the amount of hydrogen as it is constituted of 2 protons and electrons. However, its mass is roughly 4 times as much as the hydrogen. This problem was solved in 1932 by Chadwick [15] with the discovery of the *neutron*. The neutron is slightly heavier than the proton and is neutrally charged.

It is hard to determine by whom the photon was discovered. However, the quantization of light itself has its origin from 1900 when Planck [16] tried to explain the black-body spectrum of the electromagnetic radiation - i.e. radiation from a hot object. Assuming the following quantization he could avoid the ultraviolet catastrophe[2]

$$E = h\nu \tag{2.1}$$

where h is the Planck's constant and ν is the frequency of the light. In 1905, Einstein continued further on by predicting that light itself is a particle - the photon [17]. This was confirmed in 1923 by an experiment conducted by Compton. The photon is not like the three other particles mentioned above. It belongs to a family of particles named *bosons*, whereas the electron, proton and the neutron are *fermions*.

In 1930, another truly fundamental particle, the *neutrino*, was postulated by Pauli [18]. Conservation of energy in β-decay[3] led to the assumption of an extra particle emitted alongside with the electron. Continuing on with relativistic quantum mechanics Dirac (1927) [19] found an astonishing result when investigating free electrons at high velocities. Combining quantum mechanical operators with Einsteins famous equation [20]

$$E^2 = (pc)^2 + (mc)^2 \tag{2.2}$$

where p is the four-momentum vector, lead him to the Dirac equation

$$\left(\beta mc^2 + c\left(\sum_{n=1}^{3} \alpha_n p_n\right)\right)\psi(x,t) = i\hbar\frac{\partial\psi(x,t)}{\partial t} \tag{2.3}$$

where α and β are 4x4 Hermitian matrices and $\psi(x,t)$ is the wave function of an e^- with mass m, $\hbar$ is the reduced Planck constant and space-time coordinates x

[2]The ultraviolet catastrophe was a direct consequence of applying the much successful theory of Statistical Mechanics to electromagnetic fields. It led to the fact that the total power irradiated photons should be infinite.

[3]β-decay: $n \to p + e^{\pm} + \nu/\bar{\nu}$

and t.

In natural units[4] we get, using Einstein summation notation[5]

$$(i\gamma^\mu \partial_\mu - m)\psi = 0 \tag{2.4}$$

where γ^μ are the Dirac matrices.

By investigating equation (2.2) we can see that it gives rise to negative energy solutions. This was later postulated to be positive-energy states of a different particle, the positron, and discovered in 1931 by Anderson [9]. The positron is the anti particle of the electron and vice versa. It has exactly the same properties except an opposite charge. Postulated independently by Gell-Mann [21] and Zweig [22] in 1964 was the quark model. Hadrons are again categorized into baryons and mesons constituted by 3 or 2 quarks, respectively.

2.2 Brief overview of SM

As mentioned above, the Standard Model (SM) is a theory describing the elementary particles and their interactions. It's divided between the matter particles, i.e. the *fermions* having half integer spin and the force carrying particles having integer spin. Further on, the fermions are divided into leptons and quarks and can be represented as a set of left-handed doublets and right-handed singlets according to the weak isospin of the $SU(2)_L$ symmetry group [23].

Leptons

As shown in table 2.1 the leptons are divided into three families. This group consist of a set of charged leptons l where each has a neutrally charged companion - the neutrino ν_l. Neutrinos were believed to be massless until the detection of neutrino oscillations indicating a small but nonzero mass.

[4] $\hbar = c = 1$

[5] $x_\mu = \sum_{\nu=0}^{3} g_{\mu\nu} x^\mu \equiv g_{\mu\nu} x^\mu$ where $g_{\mu\nu}$ is the contravariant metric tensor given as $\mathrm{diag}(+1, -1, -1, -1)$ in Minkowski space.

Generation	Symbol	Charge $Q[e]$	$\mathbf{L}_e$	$\mathbf{L}_\mu$	$\mathbf{L}_\tau$	Spin	Mass [MeV/c^2]
I	e	-1	+1	0	0	1/2	0.511
	ν_e	0	+1	0	0	1/2	< 2.2
II	μ	-1	0	+1	0	1/2	105.7
	ν_μ	0	0	+1	0	1/2	< 0.17
III	τ	-1	0	0	+1	1/2	1777
	ν_τ	0	0	0	+1	1/2	< 15.5

Table 2.1: Generation of leptons. The lepton flavor numbers $\mathbf{L}_l$, $l = e, \mu, \tau$ are also shown. [8]

Quarks

As with the leptons, the quarks interact through the weak interaction. They also carry charge of two types: color charge and electrical charge of fractions seen in table 2.2. When introducing quantum chromodynamics later in this chapter we will have a deeper look at the concept of color. The quarks therefore interacts with all of the fundamental forces. See section 2.3.2 for a mathematical description.

Generation	Symbol	Charge $Q[e]$	I_3	**C**	**S**	**T**	**B**	Spin	Mass [MeV/c^2]
I	u	2/3	+1/2	0	0	0	0	1/2	$2.2^{+0.6}_{-0.4}$
	d	-1/3	-1/2	0	0	0	0	1/2	$4.7^{+0.5}_{-0.4}$
II	c	2/3	0	1	0	0	0	1/2	$(1.28 \pm 0.03) \times 10^3$
	s	-1/3	0	0	1	0	0	1/2	95 ± 5
III	t	2/3	0	0	0	1	0	1/2	$(173.1 \pm 0.6) \times 10^3$
	b	-1/3	0	0	0	0	1	1/2	$(4.18^{+0.5}_{-0.4}) \times 10^3$

Table 2.2: Generation of quarks. The quantum numbers **C** (charmness), **S** (strangeness), **T** (topness) and **B** (bottomness) are shown as well as the isospin I_3. [8]

Fundamental forces and interactions

The quarks and the leptons make up all the matter around us. If it weren't for the fundamental forces, however, the quarks would not be able to combine to form nucleons and neither could the leptons contribute to make up the atoms. Responsible for confining the quarks is the strong force mediated by the gluons. The gluons carry color charge, have no mass and can interact with themselves. The confinement limit of gluons is roughly 10^{-15}m. The electroweak force have infinite range[6] due to

[6]Strength falls as $\frac{1}{r}$.

the fact that the mediating particle, the photon, is massless and deconfined. This force acts between the electrically charged particles. The weak force is mediated by massive gauge bosons, namely the $W^{\pm}$ and Z. The fact that they are so heavy limits the range to 10^{-18}m [23]. The electromagnetic and the weak force are treated as different manifestations in the electroweak unification which can be found in section 2.3.3. The gravitational force is too weak to have a significant impact on the subatomic particles. Table 2.3 summarizes the known properties of the force carriers.

Force	Mediator	Symbol	Range (fm)	$Q[e]$	T_3	Relative Strength	Mass [MeV/c^2]
Electromagnetic	Photon	γ	∞	0	0	10^{-2}	0
Weak	W boson	W^-	10^{-3}	-1	1	10^{-13}	80385 ± 15
	Z boson	Z^0	10^{-3}	0	0	10^{-13}	91 187 ± 21
Strong	Gluon	g	$1-2$	0	0	10	0
Gravity	Graviton[a]	g^0	∞	0	0	10^{-42}	0

Table 2.3: Fundamental forces. [8]

[a]This has not been experimentally confirmed.

2.3 Quantum Field Theory and the Standard Model

To reach towards an understanding of quantum field theory (QFT), or field theories in general, we need to look into the concept of a *gauge theory*. A gauge theory is in the simplest terms a field theory in which the *Lagrangian*, $\mathcal{L}$, is invariant under certain Lie-group transformations.[7] The simplest of these is the unitary, $U(1)$, transformation which we will look more into when we get to QED.

The Lagrangian $\mathcal{L}$, in QFT, is a function of the fields ϕ and their derivatives $\partial_\mu\phi$ and will from now on be written as the Lagrangian density. The principle of action S is an important concept in the understanding of QFT. It is defined as the space-time integral of the Lagrangian over some arbitrary space-time region Ω.

$$S = \int_\Omega d^4x \mathcal{L}(\phi, \partial_\mu\phi) \tag{2.5}$$

where d^4x is the four-dimensional element $dx^0d^3\mathbf{x}$

[7]The Lagrangian, L, is given as the difference in kinetic- and potential energy (L = T-V). The density is defined from $L = \int \mathcal{L}dx^3$

Hamilton's principle states that the action integral for an actual path (e.g. trajectory by a classical particle) is stationary. This is a remarkable lemma as it says the variation δS is zero.

$$\begin{aligned}\delta S &= \int_\Omega d^4x \Big\{ \frac{\partial \mathcal{L}}{\partial \phi}\delta\phi + \frac{\partial \mathcal{L}}{\partial(\partial_\mu \phi)}\delta(\partial_\mu \phi) \Big\} \\ &= \int_\Omega d^4x \Big\{ \frac{\partial \mathcal{L}}{\partial \phi}\delta\phi + \partial_\mu\Big(\frac{\partial \mathcal{L}}{\partial(\partial_\mu \phi)}\Big)\delta\phi + \partial_\mu\Big(\frac{\partial \mathcal{L}}{\partial(\partial_\mu \phi)}\delta\phi\Big) \Big\} = 0\end{aligned} \tag{2.6}$$

By using Gauss' divergence theorem on the last term in equation (2.6) it can be converted into a surface integral over the four-dimensional space-time region Ω. As the fields are stationary on this surface we have $\delta\phi = 0$ and hence the last term vanishes.

From this, we get the *Euler-Lagrange* equation used to obtain the equation of motion for the field ϕ

$$\frac{\partial \mathcal{L}}{\partial \phi} - \partial_\mu\Big(\frac{\partial \mathcal{L}}{\partial(\partial_\mu \phi)}\Big) = 0 \tag{2.7}$$

Applying the equation above on the fermionic field ψ, we can easily derive the Dirac equation (2.4) by using the Euler-Lagrange equation [24].

2.3.1 Quantum Electrodynamics

Quantum Electrodynamics is a field theory describing the electromagnetic interaction carried out by the photon. Mathematically speaking it is an Abelian group meaning that its elements commute.[8] The basis of QED stems from the electric $\mathbf{E}$ and magnetic $\mathbf{B}$ fields, which can be expressed in terms of a vector field $\mathbf{A}$ and a scalar field ϕ

$$\mathbf{E}(x) = -\nabla\phi(x) - \frac{\partial \mathbf{A}(\mathbf{x})}{\partial t}, \qquad \mathbf{B}(x) = \nabla \times \mathbf{A}(\mathbf{x}) \tag{2.8}$$

[8]Elements of a group can be written in the following way: $g = \exp(i\alpha_i T_i)$ where $i = 1, ..., n$ and α_i is an arbitrary number and T_i is the generator of the group.

We can perform a gauge transformation by observing that the only quantities with any physical significance in equation (2.8) is $\mathbf{E}(\mathbf{x})$ and $\mathbf{B}(\mathbf{x})$. Note that the vector potentials $A_\mu(x) = (\phi(x), \mathbf{A}(\mathbf{x}))$ are auxiliary fields and hence not unique to the gauge invariance of the theory. The following step is known as a local gauge transformation of $A_\mu(x)$ [9]

$$A_\mu(x) \to A'_\mu(x) = A_\mu(x) + \partial_\mu \Lambda(x) \tag{2.9}$$

where $\Lambda(x)$ is an arbitrary function.

The Dirac Lagrangian for a free fermion of mass m given by the field $\psi(x)$ is

$$\mathcal{L} = \bar{\psi}(i\gamma^\mu \partial_\mu - m)\psi = \mathcal{L}_0 \tag{2.10}$$

where $\bar{\psi} \equiv \gamma^0 \psi^\dagger$. For the free electromagnetic field we have the following lagrangian

$$\mathcal{L}_\gamma = -\frac{1}{4} F^{\mu\nu} F_{\mu\nu} \tag{2.11}$$

where $F^{\mu\nu} = \partial^\mu A^\nu - \partial^\nu A^\mu$, which is the electromagnetic field tensor.

The local gauge transformation for the Dirac (fermion) field is given by a $U(1)$ symmetry, namely

$$\psi(x) \to \psi'(x) = U\psi(x) = e^{iqe\Lambda(x)}\psi \tag{2.12}$$

where q takes a value of ± 1 and e is the electric charge. The Lagrangian is invariant under global phase transformation, i.e. Λ is not a function of x^μ. Requiring a local gauge invariance and thus making the Lagrangian invariant under this $U(1)$ symmetry introduces interaction terms between the photon and the fermion. This can be done by substituting the derivative by a covariant derivative

$$\partial_\mu \to D_\mu = \partial_\mu + iqeA_\mu(x) \tag{2.13}$$

and inserting into the free fermion Lagrangian Eq. (2.10) we get

$$\mathcal{L} = \bar{\psi}(i\gamma^\mu D_\mu - m)\psi \tag{2.14}$$

$$= \bar{\psi}(i\gamma^\mu \partial_\mu - m)\psi + iqe\bar{\psi}\gamma_\mu A^\mu \psi = \mathcal{L}_0 + \mathcal{L}_{int} \tag{2.15}$$

[9] $A_\mu(x)$ is interpreted as the photon field.

Altogether, Eq.(2.11) with Eq.(2.15), gives the Lagrangian for quantum electrodynamics,

$$\mathcal{L}_{QED} = \bar{\psi}(i\gamma^\mu\partial_\mu - m)\psi + iqe\bar{\psi}\gamma_\mu A^\mu\psi - \frac{1}{4}F^{\mu\nu}F_{\mu\nu} \tag{2.16}$$

We obtained this Lagrangian by demanding local gauge invariance. Next, we will investigate the Lagrangian for quarks and the gluons - the force carrier of the strong interaction.

2.3.2 Quantum Chromodynamics

Quantum Chromodynamics or *QCD* is the theory of strong interactions. As viewed in table 2.2 quarks come in different types, or in *flavours* . Alongside with spin and electromagnetic charge (i.e. its coupling to the EM-field) comes another charge: namely *color*. We denote these colors *r,g*, and *b* i.e. red, green, and blue, respectively. This means that a quark of flavor f with e.g. color r has a unique wavefunction ψ_r^f. The free quark Lagrangian[10] will thus have the following form

$$\mathcal{L} = \sum_{f=u}^{t} \bar{\psi}_r^f(i\gamma^\mu\partial_\mu - m)\psi_r^f + \bar{\psi}_g^f(i\gamma^\mu\partial_\mu - m)\psi_g^f + \bar{\psi}_b^f(i\gamma^\mu\partial_\mu - m)\psi_b^f \tag{2.17}$$

or in a more elegant way

$$\mathcal{L}_0^{QCD} = \sum_{f=u}^{t} \bar{\Psi}^f(i\partial\!\!\!/ - m)\Psi^f \tag{2.18}$$

where we've introduced Ψ which is given as $\Psi^{f\dagger} = (\psi^{f\dagger}{}_r, \psi^{f\dagger}{}_g, \psi^{f\dagger}{}_b)$.

Let's now look at the global gauge transformation. Quantum chromodynamics is a non-abelian gauge theory meaning that the elements of the $SU(3)_c$, the index c corresponds to group is non-commutable. Looking at the generators $\lambda_i, (i = 1, ..., 8)$, which in QCD are the Gell-Mann matrices, an important relation arises

$$\left[\frac{\lambda^\gamma}{2}, \frac{\lambda^\delta}{2}\right] = i\frac{\lambda^\epsilon}{2}f^{\gamma\delta\epsilon} \tag{2.19}$$

[10] Again, I'm referring to the Lagrangian density

Where $f^{\gamma\delta\epsilon}$ is the totally antisymmetric structure constant.

These matrices are linearly independent Hermitian[11] matrices. The $SU(3)_c$ transformation operator takes the following form

$$U(\alpha) = e^{i\alpha_i\lambda_i/2} \tag{2.20}$$

where $\alpha_i, (i = 1, ..., 8)$ are arbitrary real numbers. This is a unitary transformation with the special[12] property that $\det U(\alpha) = 1$

$$\Psi^f(x) \to \Psi^{f'}(x) = U(\alpha)\Psi^f(x) \equiv e^{i\alpha_i\lambda_i/2}\Psi^f(x) \tag{2.21}$$
$$\bar{\Psi}^f(x) \to \bar{\Psi}^{f'}(x) = U^\dagger(\alpha)\bar{\Psi}^f(x) \equiv \bar{\Psi}e^{-i\alpha_i\lambda_i/2} \tag{2.22}$$

In order to obtain the full QCD Lagrangian we follow the same steps as we did for QED. The derivatives in $\mathcal{L}_0$ is replaced by covariant derivatives of the form

$$D^\mu(x) \equiv \partial^\mu + ig_s\frac{\lambda_j}{2}A_j^\mu(x) \tag{2.23}$$

where the introduction of eight real gauge fields $A_j^\mu(x)$ takes form. These are known as the gluon fields and excitations in these fields are known as the force carriers of the strong interaction - i.e *gluons*.

Substituting the derivative with the covariant derivative as well as applying the transformation of Ψ^f give us an interaction term $\mathcal{L}_I$

$$\mathcal{L}_I = -\sum_{f=u}^{t}\frac{1}{2}g_s\bar{\Psi}^f(x)\gamma_\mu\lambda_j\Psi^f A_j^\mu(x) \tag{2.24}$$

Analogous to the field strength tensor in QED describing the free photons we have similar terms describing free massless gluons. A gauge invariant term involving the gluon field strength tensor $G^{\mu\nu} \equiv \frac{\lambda_i}{2}G_i^{\mu\nu}$ can be shown to be given as

$$G_i^{\mu\nu} = \partial^\nu A_i^\mu(x) - \partial^\mu A_i^\nu(x) - g_s f_{ijk}A_j^\nu(x)A_k^\nu(x) \tag{2.25}$$

This field strength tensor leads to an outstanding fact: these massless vector

[11] Hermitian matrices have the nice feature that they're equal to the transpose complex conjugate.
[12] The SU groups are referred to as *special unitary groups*.

bosons are self interacting. In QED this last term was missing due to the commutable $U(1)$ group elements. Putting it all together, with the kinetic term $\mathcal{L}_g = -\frac{1}{4}G_{i\mu\nu}G_i^{\mu\nu}$ we get the total Lagrangian to be

$$\mathcal{L}_{QCD} = \mathcal{L}_0 + \mathcal{L}_I + \mathcal{L}g \tag{2.26}$$
$$\mathcal{L}_{QCD} = \sum_{f=u}^{t} \bar{\Psi}_f(i\gamma^\mu D_\mu - m)\Psi_f - \frac{1}{4}G_{i\mu\nu}G_i^{\mu\nu}$$

The fermions governed by QCD have some interesting properties: they are confined to colour space. Only colourless particles are to be observed, hence the quarks, which have colour charge, cannot be deconfined or observed as a single particle. There are options for a particle interacting with the strong force to be colourless: 1.) The particle is made up by a quark-antiquark pair i.e. *meson*[13]. 2.) The particle is composed by three quarks, i.e. *baryon* whose colour charge add up to white, or colourless. If one would try separate for instance a quark-antiquark pair it would require such a vast amount of energy to overcome the strong force in the separation that a new quark-antiquark pair would be created.

2.3.3 Electroweak Theory

Up to this point, we have been looking at $U(1)$ and $SU(3)_c$ symmetry, which are symmetries used to describe the electromagnetic and strong interaction, respectively. As with the electromagnetic and the strong force, the weak force also exhibits spin 1 bosons acting as force carriers, namely the charged $W^\pm$ bosons and the neutral Z^0 boson. As opposed to the photons and the gluons the mediating force particles of the weak interaction are quite heavy in the order of $80 - 90$ GeV/c^2 [8]. The lifetime of these particles are related to the uncertainty principle which gives us a decay length of about 10^{-3}fm.[14] Due to their high masses it takes a rather large amount of energy to produce them in the laboratory.

The prediction that the weak force was mediated by the exchange of a heavy charged boson had already been proposed in 1938 [24]. However, in the 1960s, Glashow, Salam and Weinberg [25] developed a theory that unified the electromagnetic and weak interactions in a way that has often been compared to the greatness of Maxwell's and Faraday's unification of the electric and magnetic fields. This unification had some remarkable predictions; it predicted the existence of a neutral vector boson Z^0. The processes where a Z^0 is involved are called *neutral-current* reactions. Interesting experimental evidence of weak interactions reveal that only

[13] An anti-quark has the corresponding *anti-colour* e.g. *anti-blue*

[14] Heisenberg's uncertainty principle states that $\Delta E \Delta t \leq \frac{\hbar}{2}$

leptons with left-handed chirality is present. Using the chirality projection operator the right or left component of the lepton state can be carried out with P_R and P_L, respectively, and they're given as

$$\left.\begin{aligned} P^L\psi(x) &= \psi^L(x) \\ P^R\psi(x) &= \psi^R(x) \end{aligned}\right\} = \frac{1 \pm \gamma^5}{2}\psi(x) \tag{2.27}$$

Our goal is to find a global phase transformation leading to conservation of leptonic currents. We can not have mass terms satisfying the new gauge theory so our masses are put to zero. Following on we have the free lepton Lagrangian[15]

$$\begin{aligned} \mathcal{L}_0 &= \overline{\psi}_l \partial\!\!\!/ \psi_l + \bar{\psi}^L_{\nu_l} \partial\!\!\!/ \psi^L_{\nu_l} && (2.28) \\ &= \bar{\psi}^R_l i\partial\!\!\!/ \psi^R_l + \bar{\psi}^L_l i\partial\!\!\!/ \psi^L_l + \bar{\psi}^L_{\nu_l} i\partial\!\!\!/ \psi^L_{\nu_l} \\ &= \bar{\Psi}^L i\partial\!\!\!/ \Psi^L_l + \bar{\psi}^R_l i\partial\!\!\!/ \psi^R_l && (2.29) \end{aligned}$$

Summation over different lepton flavours are implied by the l index. Note that here we have introduced the two-component spinors

$$\Psi^L_l(x) = \begin{pmatrix} \psi^L_{\nu_l}(x) \\ \psi^L_l(x) \end{pmatrix} \quad , \overline{\Psi}^L_l(x) = (\overline{\psi}^L_{\nu_l}(x) \quad \overline{\psi}^L_l(x)) \tag{2.30}$$

as well as the Dirac slash notation $A\!\!\!/ = \gamma_\mu A^\mu$ where A^μ is a four vector.

Moving on to the generators of this new symmetry we have

$$\tau_1 = \begin{pmatrix} 0 & 1 \\ 1 & 0 \end{pmatrix}, \tau_2 = \begin{pmatrix} 0 & -i \\ i & 0 \end{pmatrix}, \tau_3 = \begin{pmatrix} 1 & 0 \\ 0 & -1 \end{pmatrix}$$

These are known as the Pauli matrices in Dirac representation and have the following commutation relation,

$$[\tau_i, \tau_j] = 2i\epsilon_{ijk}\tau_k$$

We follow the same procedure as we did in section 2.3.2 where the unitarity operator

[15] We keep referring to the Lagrangian as the Lagrangian density.

$U(\omega_i)_L = e^{ig\omega_j\tau_j/2}$ gives us the following transformations

$$\Psi_l^L(x) \to \Psi_l'^L(x) = U(\omega_i)_L \Psi_l^L(x) = e^{ig\omega_j\tau_j/2}\Psi_l^L(x) \tag{2.31}$$
$$\overline{\Psi}_l^L(x) \to \overline{\Psi}'^L(x) = \overline{\Psi}_l^L(x) U(\omega_i)_L^\dagger = \overline{\Psi}_l^L(x) e^{-ig\omega_j\tau_j/2}$$
$$\psi_l^R(x) \to \psi_l^R(x) \tag{2.32}$$

The operators $U(\omega_i)_L$ are 2×2 unitary matrices with the special property that their determinant equals ± 1, thereby called $SU(2)_L$ transformations. These operators have this unitarity property for any three real numbers $\omega \equiv (\omega_1, \omega_2, \omega_3)$.

Using Noethers theorem on (2.29) leads to the following conserved current,

$$j^\mu = \overline{\Psi}_l^L \gamma^\mu g\omega_i \frac{\tau_i}{2} \Psi_l^L = \omega_i J_i^\mu \tag{2.33}$$

choosing ω_i to be arbitrary and writing

$$J_i^\mu = \overline{\Psi}_l^L \gamma^\mu \omega_i \frac{\tau_i}{2} \Psi_l^L \tag{2.34}$$

we obtain the 3 conserved weak isospin currents[16] Writing out the conserved currents one can arrive at the quantity *conserved hypercharge* Y related to the electric charge Q and the weak isocharge I_3^W in the following manner

$$Y = Q/e - I_3^W \tag{2.35}$$

where e is the electric charge.

Since both the electric charge Q and the weak isocharge I_3^W are conserved quantities, the hypercharge Y, by means, also needs to be a conserved quantity. This contributes to a new symmetry. Namely, the $U(1)_Y$ symmetry with the following operator

$$\psi \to e^{ig'Y\epsilon}\psi = U(\epsilon)_Y \psi \tag{2.36}$$

where the g' is a real coupling constant and ϵ is an arbitrary real number.

The true greatness of the work done above comes with the unification of the

[16]Note: $\partial_\mu j_i^\mu = 0$, thus $\partial_\mu J_i^\mu = 0$.

two symmetries, $SU(2)_L$ and $U(1)_Y$, known as the *Electro Weak Unification* or $SU(2)_L \otimes U(1)_Y$. By using both $U(\omega_i)_L$, for $SU(2)_L$ and $U(\epsilon)_Y$ for $U(1)_Y$ the transformation is done in a following manner

$$\Psi_l^L(x) \to \Psi_l'^L = U(\epsilon)_Y U(\omega_i)_L \Psi_l^L(x) = \exp[(ig'Y\epsilon + ig\omega_j\tau_j/2)]\Psi_l^L(x) \quad (2.37)$$
$$\overline{\Psi}_l^L(x) \to \overline{\Psi}'^L(x) = \overline{\Psi}_l^L(x)U(\omega_i)^\dagger U(\epsilon)_Y^\dagger = \overline{\Psi}_l^L(x)\exp[-(ig'Y\epsilon + ig\omega_j\tau_j/2)]$$
$$\psi_l^R(x) \to U(\epsilon)_Y\psi_l^R(x) = \exp[ig'Y\epsilon]\psi_l^R(x) \quad (2.38)$$

The resulting gauge invariant Lagrangian for massless leptons is then written as

$$\mathcal{L}^l = \overline{\Psi}_l^L i\gamma_\mu(\partial^\mu + ig\frac{\tau_i}{2}W_i^\mu + ig'YB^\mu)\Psi_l^L + \overline{\psi}_l^R(x)i\gamma_\mu(\partial^\mu + ig'YB^\mu)\gamma\psi_l^R \quad (2.39)$$

where the introduction of four new gauge bosons, W_i^μ and B^μ has been introduced. Two of them, $W^\pm$, are charged while the two remaining can be combined into the physical fields Z^0 and γ, and mixing between them is described by the weak mixing, or Weinberg angle, θ_W.

2.3.4 Higgs mechanism and spontaneous symmetry breaking

The Electro weak theory has proved great success in the sense of unification of the two forces. However, something is clearly missing; the particles are massless! We will have a short look at one of the solutions to this, namely the *Higgs mechanism* [26][17]. This mechanism restores the masses of the $W^\pm$ and Z^0 bosons through a process known as spontaneous symmetry breaking. Let's look at the Lagrangian for the Higgs model

$$\mathcal{L} = \frac{1}{2}\partial_\mu\phi^\mu\partial_\mu\phi^\mu - V(\phi) \quad (2.40)$$

[17] Actually known as the Brout-Englert-Higgs mechanism [27]

where the potential $V(\phi)$ is given as

$$V(\phi) = \frac{1}{2}\mu^2\phi^2 + \frac{1}{4}\lambda\phi^4 \tag{2.41}$$

Having a closer look at the Higgs potential enables us to get a schematically view of the symmetry breaking

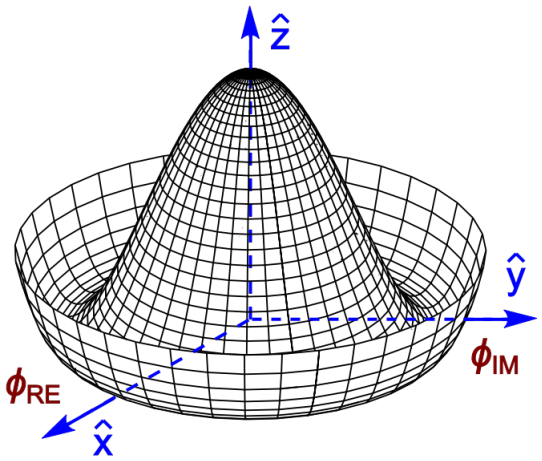

Figure 2.1: Higgs Potential [4]

The overall system in itself is perfectly symmetric, however its lowest energy solution differs by a phase θ. The vacuum expectation value is situated in the trough of the "Mexican hat" and as we can see this state is degenerate making the outcome an asymmetric state. As we want to break the symmetry of the $SU(2)_L \otimes U(1)_Y$ to obtain masses for our gauge bosons we introduce a weak isospin doublet,

$$\Phi(x) = \begin{pmatrix} \phi_\alpha(x) \\ \phi_\beta(x) \end{pmatrix}$$

where complex scalar fields ϕ_α and ϕ_β are known as the Higgs fields. As this $\Phi(x)$ is a doublet it transforms in the same manner as $\Psi_l^L(x)$ in Equation 2.37. The vacuum expectation value of the Higgs field is, as mentioned, not invariant under $SU(2)_L \otimes U(1)_Y$ breaking the symmetry. It is worth noting that it is indeed invariant under $U(1)_{EM}$ leaving an unbroken symmetry for the photons to be kept massless. The $W^\pm$, Z^0 and the spin-0 Higgs boson itself acquire their respective masses from the Higgs mechanism while the fermion masses are obtained from *Yukawa interactions* with the Higgs field. The Yukawa interaction is a coupling between a scalar field ϕ and a Dirac field ψ. On the 4th of July 2012 ATLAS and CMS saw a clear

sign of a scalar boson at a mass ranging from 125-127 GeV/c^2 at 5σ significance. This was shown to be the Higgs boson jointly rewarding Peter W. Higgs and François Englert the Nobel Prize in 2013 [28].

2.3.5 Quark Mixing and the CKM matrix

As realized, leptons can only interact weakly within their own families as can the quarks. Not only do the quarks in the mass eigenstate interact with each other they can also change flavor in a charged current processes, i.e. with the appearance of a $W^{\pm}$ boson. This reveals that, for instance, a bottom quark b may decay into a charm quark c in the presence of a W^{+}[18]. This is due to generation mixing between the *families*. The quarks are separated in families in the following way

$$\begin{pmatrix} u \\ d' \end{pmatrix}, \begin{pmatrix} c \\ s' \end{pmatrix}, \begin{pmatrix} t \\ b' \end{pmatrix}$$

where the d', s', and b' are the weak quark eigenstates and are linear combinations of the quark mass eigenstates. The degree of mixing between the different families are represented by the 3×3 unitary Cabibbo-Kabayashi-Maskawa (CKM) [29] [30] matrix

$$\begin{pmatrix} d' \\ s' \\ b' \end{pmatrix} = \begin{pmatrix} V_{ud} & V_{us} & V_{ub} \\ V_{cd} & V_{cs} & V_{cb} \\ V_{td} & V_{ts} & V_{tb} \end{pmatrix} \begin{pmatrix} d \\ s \\ b \end{pmatrix}$$

The diagonal CKM matrix elements are close to unity and therefore states a higher coupling between quarks inside their own generation. The off diagonal elements are rather small making transitions between families suppressed. CKM elements are determined experimentally and the cleanest procedure for measurement is to study semileptonic decay channels, i.e. $q \to q' l \nu$, whose decay rate is proportional to $|V_{qq'}|^2$.

2.3.6 CP Violation

It has for a long time been believed that particles are symmetric particles, however experiments prove us wrong. In this section we will only look briefly at two of the

[18] Note that in such a process it is the positive charged W^{+} boson that is present. This is crucial to account for the charge difference for the b and c.

known transformations one can do on a particle which leaves the universe unaffected - that is CP symmetry.

Charge conjugation $C(x)$ turns a particle into its respective anti-particle, and can be described as a symmetry between particles and antiparticles. As we know, there is not an equal amount of matter and antimatter, i.e. not a present symmetry, so this has clearly been violated at some point. The operator works in the following manner,

$$C\psi(q) = -\psi(-q) \tag{2.42}$$

Parity transformation $P(x)$ is a mirroring transformation reflecting the particle, or a state ψ with respect to an adjacent arbitrary plane in the following way,

$$P\psi(x) = \psi(-x) \tag{2.43}$$

Such a transformation is conserved in electromagnetism, strong interactions and gravity, but is violated in weak interactions.

For instance, the decay of the pseudoscalar B_s^0 to the vector-vector $J/\psi\phi$ final state results in an admixture of CP-odd and CP-even with the orbital angular momentum $L = 0$, 1 or 2 [31]. The final states corresponding to the orbital angular momentum value $L = 0$ are known as CP-even, whilst the state with $L = 1$ is CP-odd. The final states $J/\psi\phi$ may be produced with the K^+K^--pair in a S-wave configuration - such a final state is CP-odd [32].

Chapter 3

The Experiment

The European Organization for Nuclear Research known as CERN [1] is the largest particle physics laboratory in the world located at the Swiss-French border.

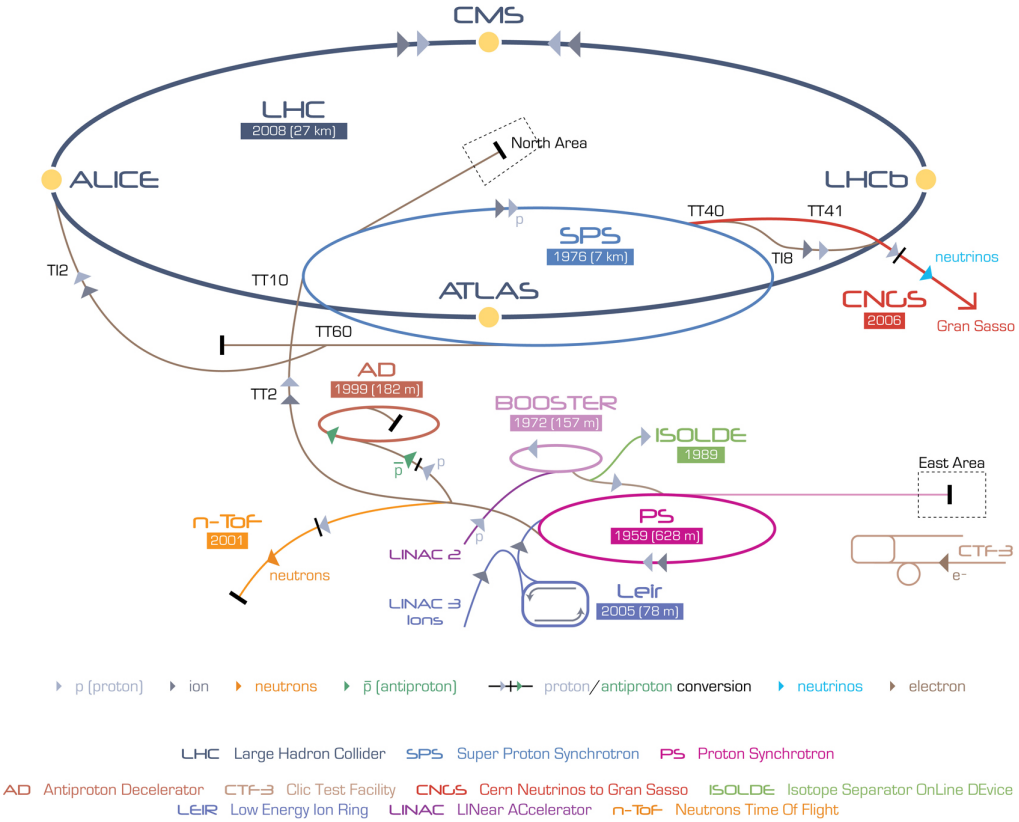

Figure 3.1: The Large Hadron Collider Complex

[1] Conseil Européen pour la Recherche Nucléaire

3.1 Large Hadron Collider

The Large Hadron Collider (LHC) is the largest and most powerful particle accelerator on planet earth. It consists of several experiments and figure 3.1 reveals its complexity. The main goal of the LHC is to gauge a better understanding of the properties of fundamental particles and evaluate the theoretical framework of the Standard Model for different physics scenarios. It does so by accelerating protons close to the speed of light [2] around a 27 km ring located 100 m underground. These protons are accelerated in the opposite direction and are forced to collide at four openings, which accommodate the largest experiments at CERN: LHCb, ALICE, CMS and ATLAS. Later in this chapter we will have a thorough look at the latter one.

As mentioned earlier, the particles of the subatomic world are immensely small, they probably do not have any volumetric structure at all, and their masses are incomparable to our daily life - so why do we need so enormous experiments to probe for answers? It has to do with the physical laws themselves.

Accelerating (charged) particles suffer from energy loss known as *synchrotron radiation*[3]. Even if the charged particle moves with a constant tangential velocity it is still being radially accelerated causing it to radiate photons. The energy loss due to synchrotron radiation can be approximated by

$$-\Delta E \approx \frac{4\pi e^2}{3R}\left(\frac{E}{mc^2}\right)^4 \propto \frac{1}{R}\frac{1}{m^4} \tag{3.1}$$

so by extending the radius, the energy loss descends. Until year 2000 CERN used this 27 km ring to accelerate electrons and positrons (LEP[4]) in opposite directions. As the electron has a mass nearly 2000 times less than the proton the energy loss in comparison due to synchrotron radiation is

$$\frac{-\Delta E_e}{-\Delta E_p} = \left(\frac{m_p}{m_e}\right)^4 \approx 1.6 \cdot 10^{13}$$

which is of orders of magnitudes in separation - explaining why the LHC can reach much higher center-of-mass energy compared to LEP. What is the significance of reaching higher center of energies? Well, as we saw in chapter 1, the famous energy-mass relation postulated by Einsteins famous equation E, there is a pure relation between mass and energy. So by accelerating particles to higher energies they can

[2] E = 6.5 GeV gives 99.999999 % of the speed of light which corresponds to approximately 11 km/h slower than *c*. [33]

[3] Synchrotron radiation is electromagnetic radiation produced by the radial acceleration of a charged particle ($\mathbf{v} \perp \mathbf{a}$).

[4] The Large Electron-Positron Collider

produce particles of higher masses.

3.1.1 Luminosity & Cross Section

One of the most important parameters in accelerator physics are the luminosity $\mathcal{L}$ and cross section σ. The reason is that the luminosity tells us something about the performance of the particle accelerator. For two colliding particles, the cross section σ is the effective transverse interaction area (with respect to the relative motion) in which they must meet in order to scatter from each other.

The number of interactions per second is given by

$$\frac{dN}{dt} = \mathcal{L}\sigma_p$$

where σ_p is the interaction cross section. The luminosity is only dependent on the beam parameters and is given in units of $\mathrm{cm}^{-2}\mathrm{s}^{-1} = 10^{33}\mathrm{nb}^{-1}\mathrm{s}^{-1}$. Projecting the beam distribution onto the cross section plane in two dimensions enables us to calculate $\mathcal{L}$ yielding

$$\mathcal{L} = \frac{n_b f_{rev} N_1 N_2}{4\pi\sigma_x\sigma_y}$$

where f_{rev} is the revolution frequency, n_b is the number of bunches per beam, N_1 and N_2 are the amount of particles in beam 1 and 2, respectively, [5] and σ_x, σ_y are the projected Gaussian widths of the beam in the x- and y-direction, respectively.

The time integral over $\mathcal{L}_{tot}$ is known as the *integrated luminosity* with units $[\mathcal{L}_{tot}] = \mathrm{nb}^{-1}$

$$\mathcal{L}_{tot} = \int \mathcal{L} dt \tag{3.2}$$

For perspective, the ATLAS detector recorded a total of 35.6 fb^{-1}.

The illustrations below are taken from [34].

[5] Practically we want $N_1 = N_2 = N_b^2$ reducing the expression to $\mathcal{L} = \frac{n_b f_{rev} N_b^2}{4\pi\sigma_x\sigma_y}$.

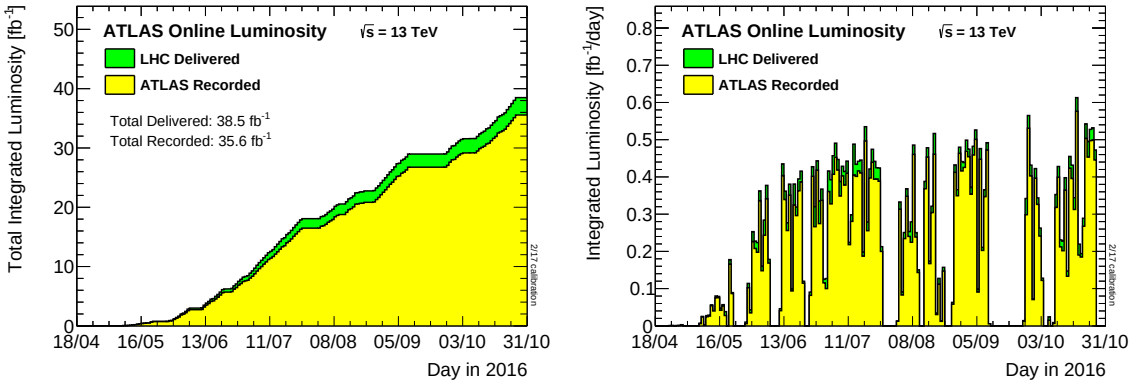

(a) **(b)**

Figure 3.2: a) Cumulative luminosity versus time delivered to (green) and recorded by ATLAS (yellow) during stable beams for pp collisions at 13 TeV center-of-mass energy in 2016. **b)** Integrated luminosity per day time delivered to (green) and recorded by ATLAS (yellow)

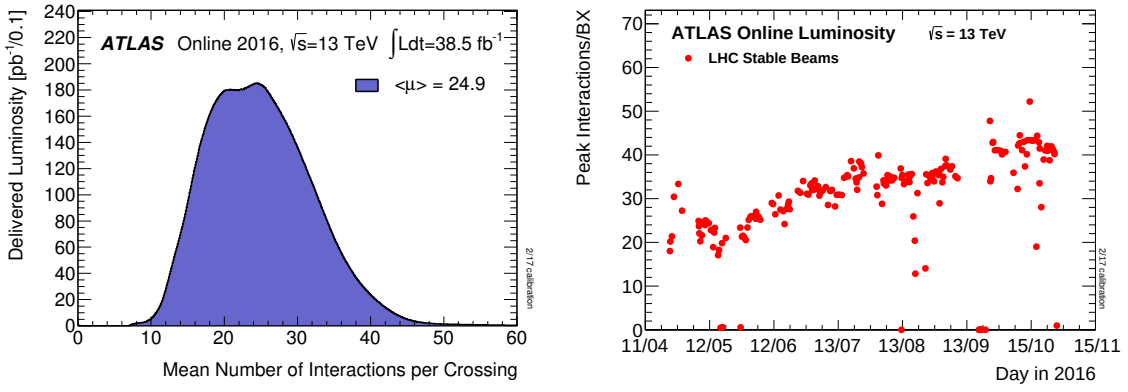

(a) **(b)**

Figure 3.3: a) Luminosity-weighted distribution of the mean number of interactions per crossing $\langle\mu\rangle$ for the 2016 pp collision data at 13 TeV centre-of-mass energy. **b)** The maximum number of inelastic collisions per beam crossing μ.

3.2 The ATLAS Detector

One of the largest experiments at the LHC is the ATLAS detector [6]. It is a multipurpose detector designed to probe a wide range of physics processes emanating from high-energy collisions. The nominal interaction point (IP) is defined to be located at the origin of the coordinate system with the z-axis in the beam direction and the x- and y-axis forming a transverse plane. The positive x-axis points radially inwards to the center of the LHC ring and the positive y-axis upwards. We can from this define the transverse momentum p_T which is an extensively used variable. The reason for its importance can easily be understood from the principle of momentum conservation. Particles traveling along with the z-axis by definition has $\sum \vec{p_T} = \vec{0}$ MeV/c indicating that for produced particles the transverse momenta must add up to zero[7]. For now, we have only been making use the Cartesian coordinate system to describe ATLAS. As the geometry of the detector resembles a cylinder with different detection modules placed as concentric circles around the interaction point, one chooses to make use of the cylindrical coordinate system. For this section, the presented material is based on [35] if not stated otherwise.

The azimuthal angle ϕ is measured around the the beam axis in the xy-plane and the polar angle θ is measured from the beam axis in the yz-plane. A common variable often used, important later on for the analysis, is the pseudorapidity given as

$$\eta = -\ln \tan\left(\frac{\theta}{2}\right) \tag{3.3}$$

Given the case of massive objects such as jets one define the rapidity

$$y = \frac{1}{2}\ln\left(\frac{E + p_z}{E - p_z}\right) \tag{3.4}$$

The azimuthal angle can be expressed in the useful way of the momentums in the x- and y-direction.

$$\phi = \tan^{-1}\left(\frac{p_y}{p_x}\right) \tag{3.5}$$

Angular separation between particle tracks in the (η, ϕ)-space is given as $\Delta R = \sqrt{\Delta\eta^2 + \Delta\phi^2}$.

[6] **A** **T**oroidal **L**HC **A**pparatu**S**

[7] Neutrinos can not be detected due to their extremely low interaction cross section. For these types of particles one makes use of the missing transverse energy E_T^{miss}

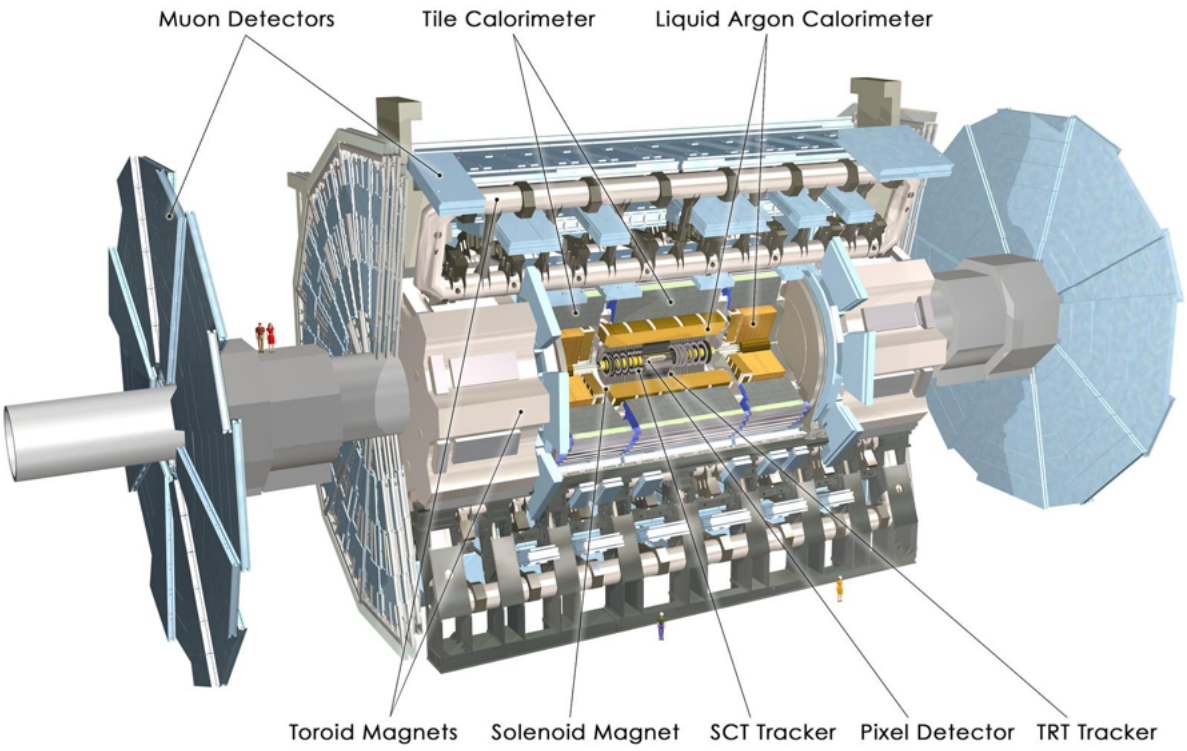

Figure 3.4: An illustration of the ATLAS detector. Its immense size is displayed with the comparison of the two physicists. It has a length of 44 meters, a diameter of 25 meters and an overall weight of approximately 7000 tonnes. [5]

3.2.1 Inner detector

Closest to the beam line we find the inner detector (ID) designed to measure the trajectories, charge and momentum of passing charged particles. The ID consists of three different systems of sensors all immersed in a solenoidal magnetic field parallel to the beam axis operating at the 2T. The outermost system is the Transition Radiation Tracker (TRT) enclosing the Semi-Conductor Tracker (SCT) and the pixel detectors, respectively. The precision tracking detectors (i.e. the pixel detector and the SCT) have a pseudorapidity coverage of $|\eta| \leq 2.5$). In the barrel region they are arranged on concentric cylinders around the z-axis, while in the end-cap regions they are stationed on disks in the xy-plane.

The inner detector is the module closest to the beam line it receives the highest measure of radiation dose causing the tracking resolution to decrease over time. With increasing luminosity the gain of event pile-up is also present leading to readout inefficiencies and suppressing the ability to tag b quarks. Therefore, for Run-2 a new

subsystem was added[8] - the Insertable B-layer (IBL). The IBL is placed between the pixel detectors and the beam pipe and shows great success.

The resolution of the tracking segments is given as

$$\frac{\sigma_{p_T}}{p_T} = 0.05\% p_T \oplus 1\%$$

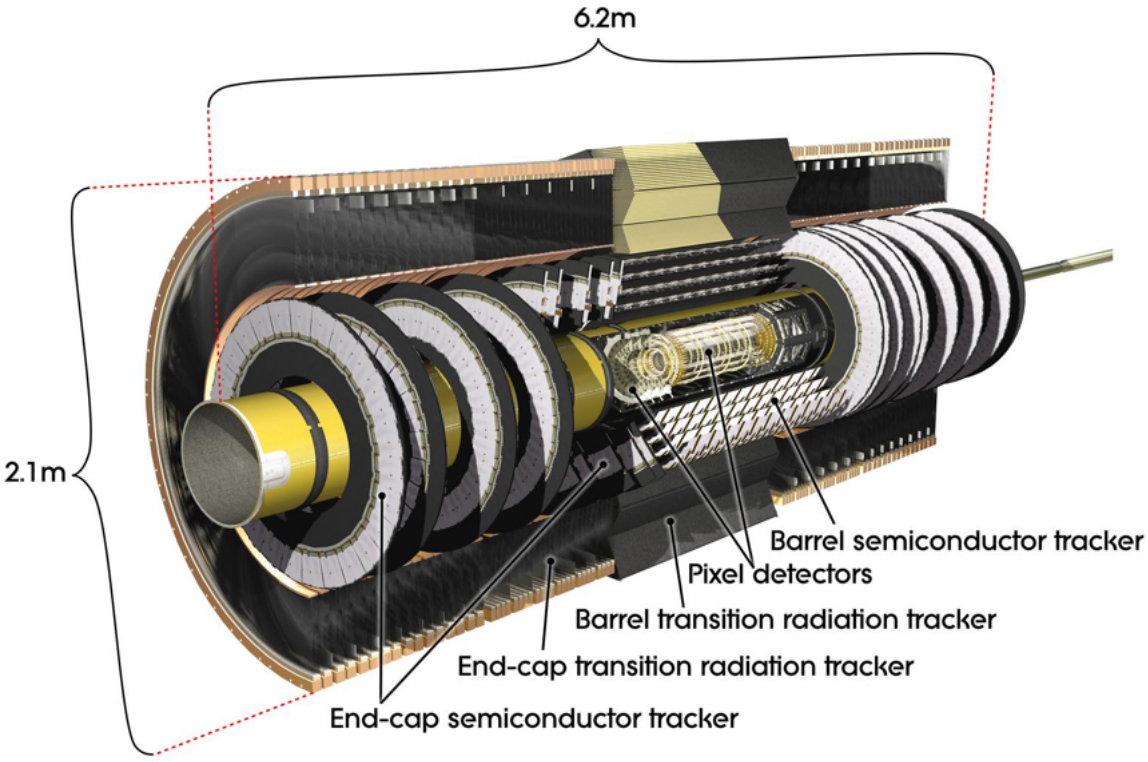

Figure 3.5: An illustration of the inner tracker. [5]

Pixel Detector

As mentioned, closest to the beam line we find the pixel detectors from which we achieve the highest detection granularity. The pixel layers are segmented in the $R\phi$ and z-plane with typically three pixel layers crossed by each track. All the pixel sensors are identical and cover a minimum pixel size of $R\phi \times z = 50 \times 400\mu\text{m}^2$ and a combined resolution of $14 \times 115\mu\text{m}^2$ for the two pseudorapidity regions.

[8] This is crucial for B-physics analysis as the B-mesons of interest typically only travel a few hundreds of μm away from the primary vertex before decaying.

Semi-Conductor Tracker (SCT)

In between TRT and pixel detectors component of the inner detector we find the Semi-Conductor Tracker. It is built up by of long narrow silicon microstrip detectors consisting of 4088 two-sided modules and over 6 million implanted readout strips. As mentioned above, the barrel and the two end-caps cover the same pseudorapidity region as the pixel detector. In the barrel region we can find 4 cylindrical layers with sensors parallel to the z-axis and for the end-caps we have 18 planar discs each holding a total of 60 m^2 silicon. The SCT has readout strips every 80 μm on the silicon allowing the positions of the charged particles to be recorded to an accuracy of 17 μm per layer in the transverse direction to the strips.

Transition Radiation Tracker (TRT)

The outermost device enclosing the SCT and the pixel detector is the Transition Radiation Tracker. The TRT consists of 50000 straw tubes in the barrel and 250000 in both of the end-caps filled with gas. A charged particle traversing the TRT ionizes the gas and is accompanied by the radiated photons. The photons interact with the molecules in the Xe-based[9] gas liberating more electrons which moves towards a gold wire at the center of the tube where it is measured. The precision measurement yields 0.17 mm. The pseudorapidity coverage of the TRT is $|\eta| \leq 2.0$ and only provides measurement in the $R\phi$-plane.

3.2.2 Calorimeter

Moving radially outwards we find the calorimeters surrounding the solenoid magnet and the ID. These devices measure the energy of both charged and neutral particles. Closest to the ID we find the electromagnetic calorimeter (EM). The ATLAS electromagnetic calorimeter is used mainly to measure the energies of electron and photons. Its accordion-shaped structure consists of many layers of lead and stainless steel providing a complete ϕ symmetry without azimuthal cracks. The particle absorbers between them is liquid argon (LAr) cooled to minus 185 Celsius. Immersed in the liquid argon is a copper grid acting as an electrode used to make measurements of particles passing through.
The EM calorimeter is segmented into two parts: a barrel and two end-caps. Each end-cap calorimeter is mechanically divided into two coaxial wheels: an outer wheel and an inner wheel shown at figure 3.6. It has pseudorapidity coverage of $|\eta| \leq 3.2$[10].

[9]The gas consists of 70% Xe, 27% CO_2 and 3% O_2.
[10]Barrel: $|\eta| < 1.475$. Outer (inner) wheel of the end-cap: $1.375 < |\eta| < 2.5$ $(2.5 < |\eta| < 3.2)$.

The resolution of the EM calorimeter is given as

$$\frac{\sigma_E}{E} = \frac{a}{\sqrt{E}} \oplus \frac{b}{E} \oplus c$$

where E is measured in GeV. The first variable a is a stochastic term taking into account statistical fluctuations of the fraction of the shower energy deposited in the liquid argon. It varies between 8-11% depending on the value of η (for $\eta = 0$, a = 10%). The second term is describes the contribution of the electrical noise and b takes a value of 0.5%. The last and constant term accounts for the calibration of the energy scale and local variations in this. Its believed to be around 0.7%. Further on, the longitudinal resolution is

$$\sigma_\theta = \frac{50 \text{ mrad}}{\sqrt{E}}$$

where again, E is measured in GeV.

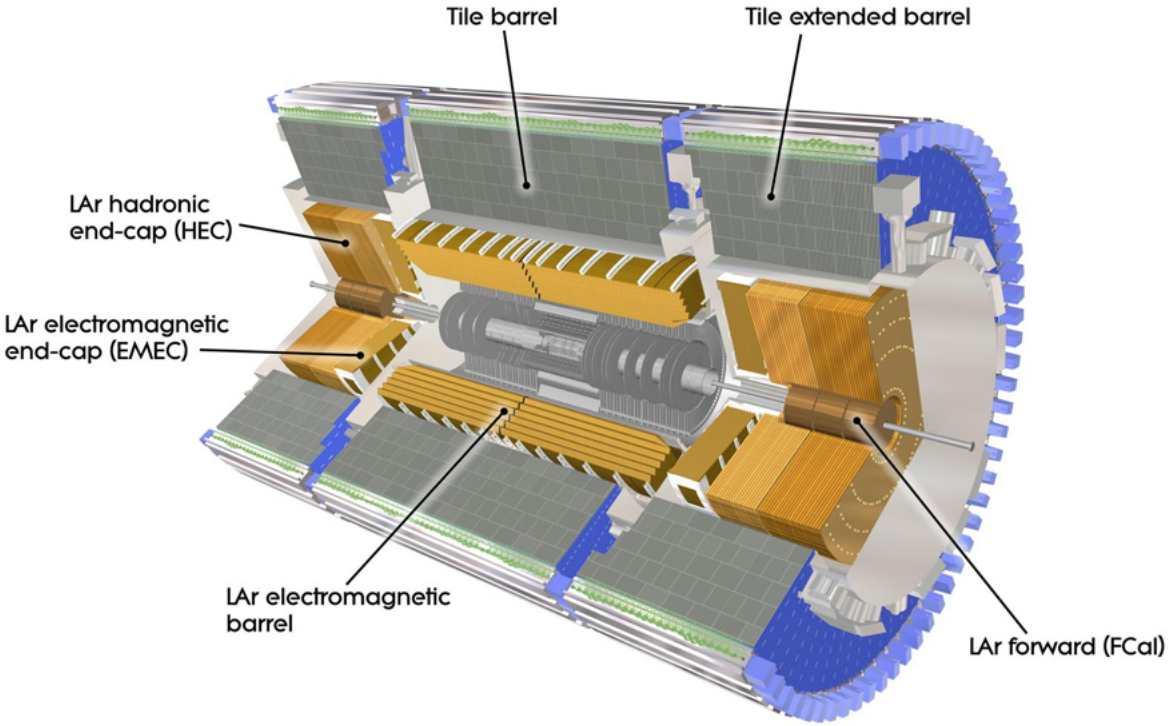

Figure 3.6: An illustration of the inner tracker. [6]

Just outside the electromagnetic calorimeter we find the hadronic calorimeters used to measure the energy deposition of both charged and neutral baryons and

mesons. It is a large array of interleaved steel and scintillators[11] sheets called *tiles*. When a high-energy hadron passes through the steel it interacts with the atomic nuclei. These nuclear reactions lead to the production of more particles which initiate further interactions leading to a shower of particles.

The hadronic tile calorimeter (just outside EM) covers a pseudorapidity region of $|\eta| < 1.0$ for the barrel and $0.8 < |\eta| < 1.7$ for the two extended barrels. In total, ATLAS has three types of different hadronic calorimeters: the tile calorimeter, the LAr hadronic end-cap calorimeter and the LAr forward calorimeter. The hadron end-cap calorimeters share the liquid argon cryostat with the end-cap electromagnetic calorimeters, but instead makes user of copper as the absorbing material. The pseudorapidity region covered by this system is $1.5 < |\eta| < 3.2$. The forward calorimeter is based of LAr-Cu-W and share the same cryostat as the EM and hadron end-cap calorimeters and is designed to have a pseudorapidity coverage all the way up to $|\eta| \leq 4.9$. It consist of three modules where the first is made of LAr alternating with copper (optimized for EM measurents), while the two others are made out of tungsten and measure the energy of the hadrons.

The granularity of hadronic calorimeter is suppressed with respect to the electromagnetic calorimeter. Most of the emitted particles are neutral pions propagating without further nuclear interactions causing a decline in the precision. Further more, the energy converted into excitation and the breakup of a nuclei will not be detected. The resolution of the hadronic calorimeter is η-dependent and is given by

$$\frac{\sigma_E}{E} = \frac{50\%}{\sqrt{E}} \oplus 3\%, \qquad \text{for } |\eta| \leq 3.$$

covering the tile- and the hadronic end-cap calorimeters. And

$$\frac{\sigma_E}{E} = \frac{100\%}{\sqrt{E}} \oplus 10\%, \qquad \text{for } 3 \leq |\eta| \leq 5.$$

covering the forward calorimeters.

3.2.3 Muon Spectrometer

Particles known as muons can penetrate through the calorimeters and reach the outermost part of ATLAS know as the muon spectrometer. They usually leave little or no sign in the ID and the EM- and the hadronic calorimeters. It is based on the magnetic deflection of of muon tracks provided by the large superconducting toroidal

[11] A scintillator is a material which radiates photons when exposed to a charged particle

magnets operating at 4 T. For the pseudorapidity region $|\eta| < 1.4$ magnetic bending is performed by the large barrel toroid shown in figure 3.7. For $1.6 < |\eta| < 2.7$ the muon tracks are deflected by two smaller end-cap magnets encapsulated in each end of the barrel toroid. The pseudorapidity region in between, $1.4 < |\eta| < 1.6$, is referred to as the transition region where the magnetic deflection is provided by a combination of the barrel and end-cap fields.

The area covered by the detectors in the muon spectrometer covers a huge area roughly equal to 5000 m^2. The resolution of the muon spectrometer is given as

$$\frac{\sigma_{p_T}}{p_T} = 10\%, \quad \text{for } p_T = 1 \text{ TeV}$$

having a full pseudorapidity coverage of $\eta < 2.7$.

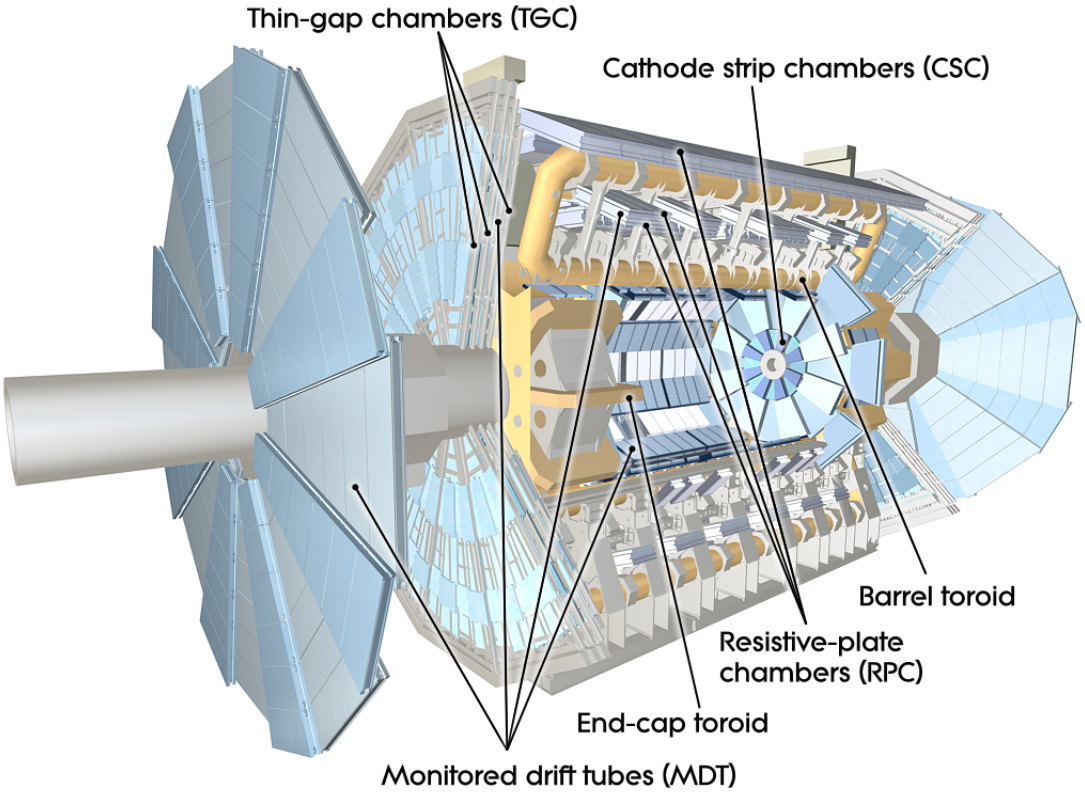

Figure 3.7: An illustration of the muon system. [7]

Chapter 4

B Physics

Weak decays of heavy mesons containing heavy quarks are extensively used to test the Standard Model and measure its parameters. The field of B physics shows the most direct way to measure important parameters as the unitarity of the CKM matrix and, as mentioned, to examine the phenomenon of charge-parity (CP) violation. In this chapter we will have a look at the production and decay mechanisms of B mesons. We will also have a look at the B_s^0 meson system at the end of the chapter.

4.1 Heavy Quark Production

Looking into the scheme of proton-proton pp collisions at the LHC, the leading order for production of heavy quarks Q are light quark annihilation and gluon-gluon-fusion given as

$$q\bar{q} \to Q\bar{Q} \qquad\qquad gg \to Q\bar{Q} \tag{4.1}$$

respectively and are illustrated in figure 4.1. The production of heavy quarks through these two processes are together known as *flavor creation* processes.

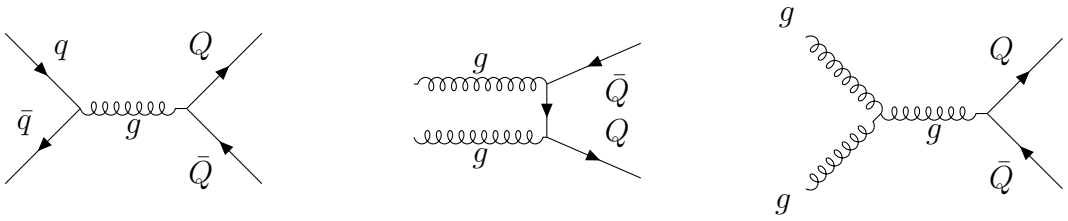

Figure 4.1: Feynman diagrams for flavour creation processes.

Another mechanism where the production of heavy quarks in the end state arises is through through *flavor excitation* processes. In these processes a heavy quark is scattered out of the sea of the incident hadron. Figure 4.1 illustrates these processes. In order to obtain a meaningful calculation of the final states the inclusion of higher-order QCD effects, such as gluon fragmentation or gluon splitting, are crucial as they also involve $g \to Q\bar{Q}$ vertices. It is a clear energy dependence between the ratio of gluon fusion to gluon fragmentation, with the latter being dominant at center-of-mass energies much larger than the mass of the heavy quarks m_Q [36].

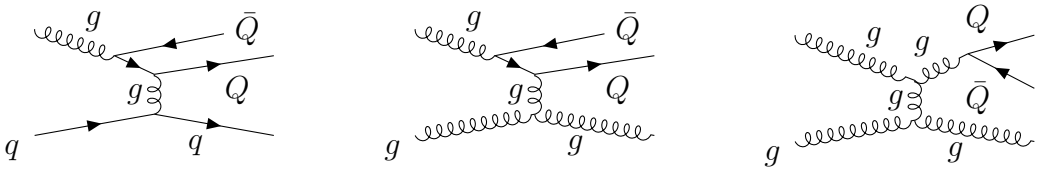

Figure 4.2: Feynman diagrams for flavour excitation processes.

4.2 Heavy Quark Symmetry

The fact that the effective coupling constant of QCD becomes weaker in large momentum transfer, known as asymptotic freedom, helps us explain why the strong interaction of hadrons containing heavy quarks are easier to understand than that of hadrons composed of light quarks. At large distances, corresponding to low momentum transfer, the coupling becomes strong leading to non-perturbative phenomena such as the confinement of quarks and gluons on a length scale given as $R_{had} \sim 1/\Lambda_{QCD} \sim 1$ fm determining the size of the hadrons. [37] The energy scale that separates the regions of large and small coupling constant is defined to be roughly $\Lambda_{QCD} \sim 0.2$ GeV. A quark Q is said to be a *heavy quark* if it is much larger than this scale i.e $m_Q \gg \Lambda_{QCD}$. From this, the quarks naturally fall into two categories; u, d and s to form the *light* quarks, whereas c, b and t form the *heavy* quarks. Free quarks have never been observed which is understood by a long distance confining property of QCD. Up, down, strange, charm and bottom quarks hadronize[1] while the top quark decays before any hadronization processes can take place due to its short lifetime. [38]

As the effective strong coupling constant $\alpha_s(m_Q)$ is energy dependent, it becomes small for heavy quarks Q implying that on length scales comparable to the Compton wavelength $\Lambda_Q \sim 1/m_Q$ the strong interactions are perturbative and similar to electromagnetic interactions. As a comparison, the size of order of the quarkonium systems $Q\bar{Q}$ are given by $\Lambda_Q/\alpha_s(m_Q) \ll R_{had}$ and are comparable to the scale of the hydrogen atom [37].

We now consider a hadron composed of a heavy quark Q and, what we shall

[1]Hadronization is the process of which quarks and gluons form a meson or baryon.

refer to as light degrees of freedom, quarks, anti-quarks and gluons. As we want the heavy quark Q to be significantly heavier than the other constituents in the hadron, we probe the sector were $m_Q \to \infty$. The light degrees of freedom are characterized by momenta of order Λ_{QCD}, which corresponds to the following Compton wavelength $\lambda_l \sim 1/\Lambda_{QCD}$. As $m_Q \gg m_l$ it follows that $\lambda_l \gg \lambda_Q$ the light degrees of freedom cannot resolve features of the heavy quark other than its conserved gauge quantum numbers, and in particular, they can not probe the actual value of λ_Q [39]. Typical momentum transfer exchanged by the light degrees of freedom with each other and the heavy quark are of the orders of Λ_{QCD} which is much smaller than the mass m_Q leaving no recoil of the heavy quark Q. Thus, the the heavy quark becomes irrelevant for the non-perturbative effects of the light degrees of freedom and instead acts as a static source of electric and chromoelectric field.

In the limit where $m_Q \to \infty$ hadronic systems, which differ only in the flavor or spin spin quantum numbers of the heavy quark, have the same configuration of their light degrees of freedom. This observation provides valuable relations between the properties of particles such as the heavy mesons B, D, B^* and D^*. These relations arise from approximate symmetries of the effective strong interactions of heavy quarks at low energies [37].

4.3 Heavy Quark Effective Theory

In the heavy quark effective theory (HQET), the mass of the heavy quark is taken to be $m_Q \to \infty$. The equations of QCD in the vicinity of the isolated heavy quark are those of the light degrees of freedom with the boundary condition that there is a static triplet source of chromoelectric field at the origin. If we have two heavy quarks in our hadron H_Q the boundary conditions will be identical indicating the same solutions for the states of light degrees of freedom in their presence and the heavy quark decouples from the rest of the system. This means that physical quantities needs to be expressed without m_Q, e.g. the four-momentum p_μ is replaced with the four-velocity v_μ.

4.4 Non-leptonic B decays

At the lowest order in the standard model non-leptonic weak decays are governed by a single $W^\pm$-exchange. The strong interaction affects this rather simple picture in a 2-fold way: 1) hard-gluon corrections accounted for by perturbative methods and renormalization group techniques giving rise to new effective weak vertices. 2) Long-distance confinement forces are responsible for the binding of quarks inside the asymptotic hadron states. The three-level diagrams are a rather simple represen-

tation of the actual picture. In the real world, quarks are confined inside hadrons bound by the exchange of soft gluons. As an example, figure 4.4 shows the decay of $\bar{B}^0 \to D^+\pi^-$ at three-level and a more realistic representation of the decay. [37].

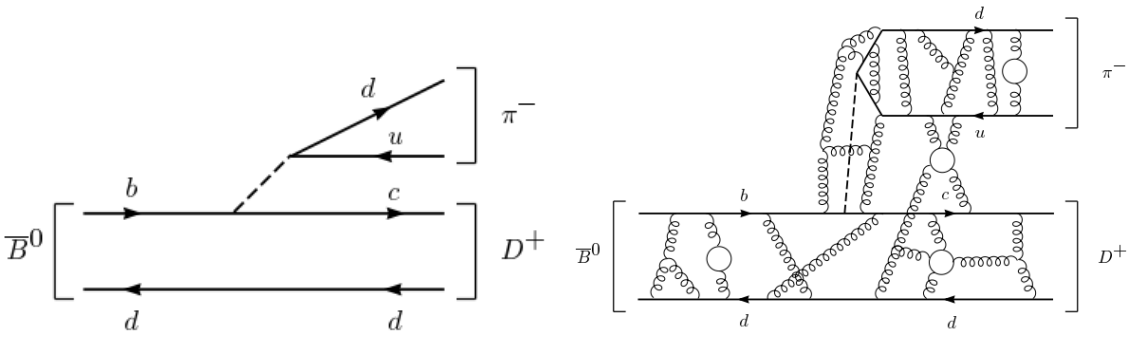

(a) Three-level Feynman diagram **(b)** More realistic representation

Figure 4.3: A simplified illustration and a more realistic interpretation of the real pricture.

4.4.1 Operator Product Expansion

The basic idea is that it is possible to separate the two regimes by means of the operator product expansion (OPE), incorporating all the long-range QCD effects in the hadronic matrix elements of the local 4-quark operators. This approach appears to be well justified due to the large differences in the time and energy scales, which are involved in the weak decays and in the formation of final hadrons. Generally the effective Hamiltonian can be written as

$$H_{eff} = \frac{G_F}{\sqrt{2}} V_{CKM} \sum_i C_i(\mu)\mathcal{O}_i + h.c.$$

where G_F is the Fermi constant V_{CKM} is the CKM matrix element for a given transition. The $C_i(\mu)$ are known as the Wilson coefficients and represents perturbatively calculable short-distance effects and the local operators $\mathcal{O}_i$ describe the non-perturbative long-distance effects of QCD. The Wilson coefficients and the local operators are both functions of the renormalization scale μ. For the decay $b \to \bar{c}s\bar{c}$ the relevant CKM matrix elements are V_{cb} and V_{cs} and the local four-quark operators $\mathcal{O}_i$ can be written in terms of color-singlet currents in the following manner

$$\mathcal{O}_1 = (\bar{c}_i\mu^\nu(1-\gamma^5)b^i)(\bar{s}_j\mu_\nu(1-\gamma^5)c^j)$$

$$\mathcal{O}_2 = (\bar{s}_i \mu^\nu (1-\gamma^5) b^i)(\bar{s}_j \mu_\nu (1-\gamma^5) c^j)$$

When performing calculations using this technique it is stressed that they are only valid at the value of the chosen renormalization scale. Theoretical errors are typically obtained by varying the scale in the range $m_b/2 < \mu < 2m_b$.

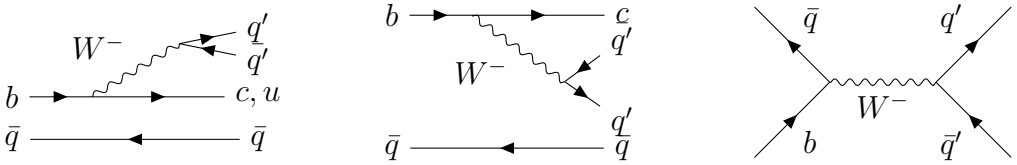

Figure 4.4: a) Spectator **b)** Color-suppressed **c)** Annihilation

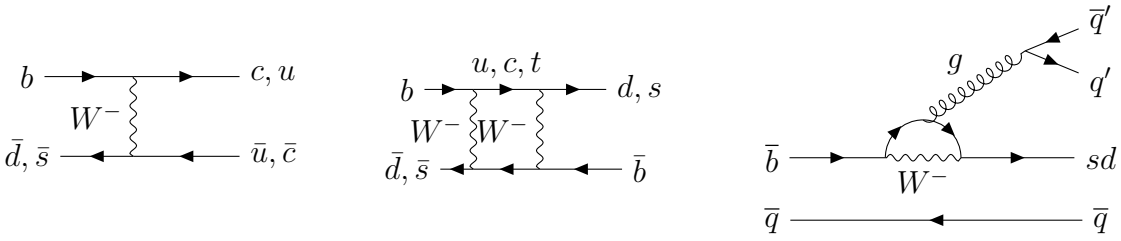

Figure 4.5: a)W^- exchange **b)** Box diagram **c)** QCD penguin

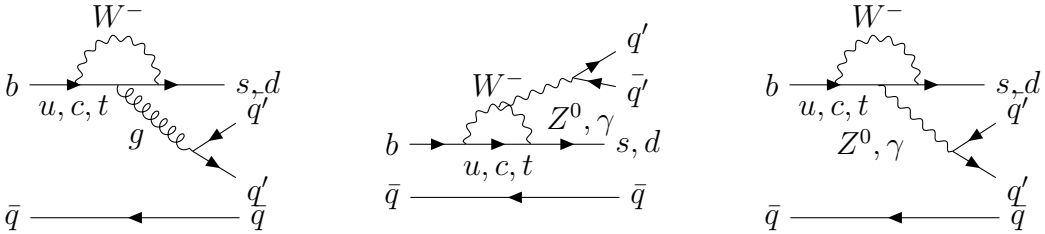

Figure 4.6: a)QCD penguin **b)** EW penguin **c)** EW penguin

Figure 4.7: a) Magnetic dipole penguin **b)** Chromomagnetic dipole penguin

4.4.2 Different non-leptonic B meson decay modes

Hadronic B mesons can undergo decay through several different processes as shown in the figures 4.4-4.7. The predominant diagram is showed in 4.4a) is known as the *spectator* diagram where the B meson either decays to a c or a u quark and a virtual W^-, which decays to a $q'\bar{q}'$. The spectator quark only participates through gluon exchanges. This is a known as a *color-favored* decay because the quark-antiquark pair, which hadronize to form the residual meson, is produced in the requisite color-singlet combination [40]. Such processes are dominated by $\mathscr{O}_1$ and are referred to as class I decays. The decay amplitude $\mathscr{A}$ is proportional to the CKM matrix elements of the quark flavors involved in the decay process, as we shall see in section 4.5.

Processes where the quark-antiquark pair produced end up in different final meson states it is known a *color-suppressed* decay. Such a diagram can be seen in figure 4.4b) and are suppressed by a factor of 3 [40] and also categorized as class II decays where the local-operator $\mathscr{O}_2$ dominates. The signal decays investigated in this thesis $B_s^0 \to J/\psi(\psi(2S))\phi$ is a color-suppressed decay. Figure 4.5 reveals the diagram for the interesting property of $B_{d,s}^0 - \bar{B}_{d,s}^0$ mixing which occurs in neutral B meson systems. The last six diagrams are known as *penguin* diagrams and involve processes where $b \to s$ or $b \to d$ and are known as flavor-changing neutral current (FCNC) processes. Such processes are not allowed at the three-level and must therefore proceed through loop or box diagrams. An example of a FCNC decay is the rare decay $B_s^0 \to \mu^+\mu^-$ measured to have a branching ratio of $2.4^{+0.9}_{-0.7} \times 10^{-9}$. [8].

4.5 The $B_s^0 \to J/\psi\phi$ and $B_s^0 \to \psi(2S)\phi$ decays

In chapter 6 and chapter 7 we perform an analysis of the non-leptonic decay modes $B_s^0 \to J/\psi\phi$ and $B_s^0 \to \psi(2S)\phi$ performed with data with a center-of-mass energy $\sqrt{s} = 13$ TeV collected by the ATLAS detector. This section provides a brief look at the two decay modes.

The B_s^0 meson is composite of a $\bar{b}$ and a s quark. As it is a neutral B meson it is subject to the phenomenon of $B_s^0 - \bar{B}_s^0$ mixing where the mass difference of these two states have been measured to be $\Delta m_{B_s^0} = (1.1688 \pm 0.0014) \times 10^{-8}$ MeV [8]. The Feynman diagram for the two decay channels are shown in figure 4.5 below.

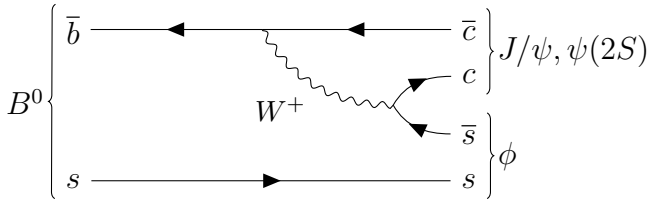

Mentioned in the introduction, we investigate the $B_s^0 \to J/\psi(\psi(2S))\phi$ decay modes where final states are $J/\psi(\psi(2S)) \to \mu^+\mu^-$ and $\phi(1020) \to K^+K^-$, which is referred to as ϕ for brevity. Viewed from the diagram the decay process begins with a $\bar{b} \to \bar{c}$ transition subject to the weak interaction. The virtual W^+ further decays to a quark-antiquark pair $c\bar{s}$ where the $\bar{s}$ hadronize with the spectator s quark to form the $\phi(s\bar{s})$ meson. The residual c quark originating from the W^+ hadronize with $\bar{c}$ quark to form the $J/\psi(c\bar{c})$ or the first excited charmonium state, namely the $\psi(2S)(c\bar{c})$ meson. It is quite evident to see that this is a color-suppressed decay. The transition of $b \to \bar{c}c\bar{s}$ is dependent on the matrix element $|V_{cb}|^2$ and is not a CKM-favored decay [41].

By using the technique of the naïve factorization a calculation of the decay amplitude $\mathscr{A}$ is possible. The following hypothesis makes the assumption that processes subject to a high recoil in both the initial and the final state interactions are suppressed. As the remnants of B decays are energetic, the color transparency argument states that $q\bar{q}$ stay close together and is of the possession of a small chromomagnetic dipole moment till the distance from the other decay products are sufficient [42]. The beauty of this is that we now have two energetic $q\bar{q}$ pairs being transparent to each other thus forming final-state mesons whilst not participating in any soft gluon exchanges. By the presence of soft gluon exchanges we would require an extremely complicated description. The methods below are mainly taken from [43] and [44].

For the decay channel $B_s^0 \to J/\psi\phi$ the decay amplitude $\mathscr{A}^{fact}$ can be expressed as

$$\mathscr{A}^{fact} = \frac{G_F}{\sqrt{2}} V_{cb}V_{cs}^* a_2(\mu) \langle \phi | (\bar{s}\gamma^\mu(1-\gamma_5)c)|0\rangle \langle J/\psi|(\bar{c}\gamma_\mu(1-\gamma_5)b|B_s^0\rangle \tag{4.2}$$

where the G_F is the Fermi constant, $V_{cb}V_{cs}^*$ are the relevant CKM matrix elements. The QCD correction parameter a_2 is relevant for the Class II[2]

$$a_2(\mu) = C_2(\mu) + \frac{1}{N_c} C_1(\mu) \tag{4.3}$$

where N_c is the number of quark colors and $C_{1,2}$ are, again, the Wilson coefficients. In order to obtain values for the matrix elements, further parametrization is needed. For the creation of the ϕ meson from the vacuum we can express the amplitude by

[2]Class III processes are where both the $\mathscr{O}_1$ and $\mathscr{O}_2$ are involved. This could for instance be $b \to \bar{c}c\bar{s}$ decays and may generate the same final states - known as Pauli interference. decays involving color-suppressed processes and takes the value.

the decay constant f_ϕ,

$$\langle \phi | \bar{s}\gamma^\mu\gamma_5 c|0\rangle = -if_\phi q^\mu \tag{4.4}$$

where the momentum transfer q^μ is given as $q^\mu = (p_B + p_{J/\psi})_\mu$ satisfying $q^2 = m_\phi^2$ The matrix element for the $B(J^P = 0^-)$ to $J/\psi(J^P = 1^-)$ transition can be parametrized by the use of four form factor $V(q^2), A_0(q^2), A_1(q^2)$ and $A_2(q^2)$[3] yielding,

$$\langle J/\psi|(\bar{c}\gamma_\mu b|B_s^0\rangle = \frac{2i}{m_B + m_{J/\psi}}\epsilon_{\mu\nu\rho\sigma}\epsilon^{*J/\psi}p_{B_\rho}p_{J/\psi_\sigma}V(q^2) \tag{4.5}$$

for the vector part and for the axial vector part,

$$\begin{aligned}\langle J/\psi|(\bar{c}\gamma_\mu\gamma_5 b|B_s^0\rangle = {} & 2m_{J/\psi}\frac{\epsilon^{*J/\psi}\cdot q}{q^2}q_\mu A_0(q^2) \\ & + (m_B + (m_{J/\psi})(\epsilon^{*J/\psi} - \frac{\epsilon^{*J/\psi}\cdot q}{q^2}q_\mu)A_1(q^2) \\ & + -\frac{\epsilon^{*J/\psi}}{(m_B + m_{J/\psi})}(p_B + p_{J/\psi} - \frac{(m_B^2 - (m_{J/\psi}^2)}{q^2}q_\mu)A_2(q^2)\end{aligned} \tag{4.6}$$

Here we have simply written the B_s^0 as B when appearing as an index such that m_B is the B_s^0 mass and, correspondingly, $m_{J/\psi}$ is the mass of the J/ψ and $\epsilon^{*J/\psi}$ is the polarization vector. Below we can see the current estimation of the branching fractions of $B_s^0 \to J/\psi(\psi(2S))\phi$ decay modes [8]

$$\mathscr{B}(B_s^0 \to J/\psi\phi) = (1.08 \pm 0.08) \times 10^{-3}$$

$$\mathscr{B}(B_s^0 \to \psi(2S)\phi) = (5.4 \pm 0.6) \times 10^{-4}$$

and the relative branching fraction measured by LHCb in 2012 [3]

$$\frac{\mathscr{B}(B_s^0 \to \psi(2S)\phi)}{\mathscr{B}(B_s^0 \to J/\psi\phi)} = 0.489 \pm 0.026(stat) \pm 0.021(syst) \pm 0.012(R_\psi)$$

The uncertainty (R_ψ) is due to the branching ratio of $\psi(2S)$ and J/ψ decaying to $\mu^+\mu^-$.

[3] $V(q^2)$ is the vector form factor and $A_0(q^2), A_1(q^2)$ and $A_2(q^2)$ are the axial vector form factors

Chapter 5

Analysis Tools

This chapter provides an introduction to the data framework used in this analysis. In order to obtain variables to be used for the event selection, a transformation of the raw data using advanced algorithms are needed. These algorithms are implemented at different stages and will be briefly discussed.

5.1 Simulation

The simulated physics events used for this analysis with 2016 tuning, are centrally produced by the ATLAS B physics group by the use of the event generator PYTHIA8 [45]. In this step, simulations such as the interaction between the quarks and gluons inside the colliding protons, subsequent parton showering, hadronization and decays into stable particles are done. PYTHIA version 8 has been completely rewritten from FORTRAN to C++ with the same description of the Standard Model processes. Samples relevant for this analysis, with the presence of a b quark, are produced under the Pythia8B extension.

After the event generation has been successfully completed, the interaction of particles with the detector material and the magnetic field is simulated. This is done with the simulation toolkit Geant4 [46]. Next step is the digitization where the response of the read-out electronics is modeled; here simulated energy deposits is transformed to a detector response, which virtually acts the same as the raw data from the real detector [47]. In the completion of the steps above, the analysis data for Monte Carlo (MC) looks identical to real data expect that information about original generated events are stored in the MC samples. These are, not surprisingly, referred to as *truth-matched* events and are correspondingly stored in the `truthTree` in the NTuples.

5.2 Run 2 Analysis Model

Proceeding from raw data to the ROOT NTuples, used for the final event selection, are performed in several stages. In each stage, uninteresting events, not matching a set criteria of interest, are skipped. A higher level of reconstruction also takes place in each stage. File formats used for this analysis are listed below [48].

- **A**nalysis **O**bject **D**ata (**AOD**), which contains information about the events and reconstructed objects within each event such as tracks, muons, electrons, jets etc. The contents of these file formats are referred to as xAOD[1] and are centrally produced directly after the reconstruction.
- **D**erived **A**nalysis **O**bject **D**ata (**DAOD**) where the DxAOD objects contain further relevant reconstructed objects. The DxAOD object are produced from the xAOD by the use of the derivation framework `AthDerivation`. With the instruction of Adam Barton, from the B physics group, a derivation script, `BPHY2.py`, containing sophisticated reconstruction algorithms were adapted for the analysis presented in this thesis.
- **NTuples** contain only information relevant for the specific analysis. The DxAOD objects are further skimmed, slimmed and thinned[2] to be made into NTuples stored in ROOT trees. The final event selection and statistical analysis are performed on this file format. This was done by the EventLoop framework where the NTupleMaker has been specifically adapted for this analysis.

For Run 2, the AODs produced by the reconstruction and the DAODs from the derivation framework can be immediately read and browsed in ROOT. In Run 1, however, the AODs were not readable by so one had to first convert them to NTuples.

5.3 ROOT and RooFit

ROOT is an object-oriented framework developed by René Brun and Fons Rademarker at CERN [12]. It is, along with framework mentioned above, the main analysis software used in this thesis. Using C++, ROOT has built-in tools for graphics, mathematical libraries and statistical analysis. Performing fits and optimization

[1] The "x" indicates Run 2 event data model (EDM)

[2] The act of skimming refer to the removal of events not passing a specific selection criteria, whilst slimming and thinning refers to the removal of whole/partial containers that are not of interest.

of likelihood functions is done with the implementation of RooFit [49], which was originally developed for the BABAR collaboration, but is now comes as a standard in ROOT.

Chapter 6

Study of $B_s^0 \to J/\psi\phi$ and $B_s^0 \to \psi(2S)\phi$

In this chapter we present the Monte Carlo (MC) study of the two decay channels $B_s^0 \to J/\psi\phi$ and $B_s^0 \to \psi(2S)\phi$. The goal of the analysis is to measure the aforementioned decay channels as well as to determine the relative branching ratio using data collected by the ATLAS detector at $\sqrt{s} = 13$ TeV from 2016.

The analysis makes use of a cut-based strategy to minimize the number of background events whilst keeping the number of event candidates, often referred to as *signal*, as high as possible. After defining specific selection criteria by using the signal sample we proceed by optimizing the signal yields using the sensitivity

$$\frac{S}{\sqrt{S+B}} \tag{6.1}$$

where S and B is the number of signal and background events, respectively.

6.1 Monte Carlo Samples

By performing a study using simulated events according to the theoretical expectations of the standard model, one can extract models expected to be observed in the data. MC studies may also be used to probe new physics when comparing to data. New physics will thus appear as statistically significant deviations from the models derived in the MC study.

The MC samples used in this analysis has been officially generated in PHYTIA by the ATLAS Production Group using 2016 tuning. As we were performing an optimization of the sensitivity to improve our selection criteria and the samples were

produced in unequal amounts, a scaling of the datasets is of utmost importance. All the MC samples have a specific number of generated events N_{gen} associated with a production cross section σ_{gen} calculated by PYTHIA. Further on, we make use of this information to scale the datasets such that the integrated luminosity of these samples matches the integrated luminosity collected by ATLAS. The weight assigned to each sample is then given as

$$w = \frac{\mathcal{L}_{Data}}{\mathcal{L}_{MC}} = \frac{\mathcal{L}_{Data}\sigma_{\text{gen}}}{N_{\text{gen}}} \tag{6.2}$$

where $\mathcal{L}_{MC} = N_{\text{gen}}/\sigma_{\text{gen}}$. MC samples with corresponding σ, N and w are listed in table 6.1.

	Sample	N_{gen}	σ_{gen} [nb^{-1}]	σ_{corr} [nb^{-1}]	w	$\mathcal{L}$ [fb^{-1}]
Signal	$B_s^0 \to J/\psi\phi$	10 000 000	767.38	0.012	0.0043	827.88
	$B_s^0 \to \psi(2S)\phi$	1 000 00	960	0.0010	0.0036	998.69
Background	$pp \to J/\psi X$	5 000 000	3498.9	208.53	148.47	15.82
	$b\bar{b} \to J/\psi X$	10 000 000	19568	13.52	4.81	0.74
	$b\bar{b} \to \mu^+\mu^- X$	49 999 000	78127	3.16	0.22	0.02

Table 6.1: Samples used in the Monte Carlo study. Corrected cross section, σ_{corr}, is obtained by multiplying with the branching fractions to force the decay into the respective channel and the PYTHIA generation cross section with the correction factors shown in table 6.2. The integrated luminosity $\mathcal{L}$ is calculated with the corrected cross section.

The weight w is then calculated according to equation 6.2. The cross section calculated by PYTHIA must be corrected by the actual topology of the decay mode and repeated hadronization effects originating in PYHTIA8B. A generation efficiency of 8.1% is included in the $b\bar{b} \to \mu^+\mu^- X$ sample. The correction parameters used to calculate the weighting are shown below

Sample	Forced decay	$\mathscr{B}$	PHYTIA8B corrections
$B_s^0 \to J/\psi\phi$	$B_s^0 \to J/\psi\phi$ $J/\psi \to \mu^+\mu^-$ $\phi \to K^+K^-$	$(1.08 \pm 0.08) \times 10^{-3}$ $(5.96 \pm 0.03) \times 10^{-2}$ $(48.9 \pm 0.5) \times 10^{-2}$	0.25
$B_s^0 \to \psi(2S)\phi$	$B_s^0 \to \psi(2S)\phi$ $\psi(2S) \to \mu^+\mu^-$ $\phi \to K^+K^-$	$(5.4 \pm 0.6) \times 10^{-4}$ $(7.9 \pm 0.9) \times 10^{-3}$ $(48.9 \pm 0.5) \times 10^{-2}$	0.25
$pp \to J/\psi X$	$J/\psi \to \mu^+\mu^-$	$(5.96 \pm 0.03) \times 10^{-2}$	n/a
$b\bar{b} \to J/\psi X$	$J/\psi \to \mu^+\mu^-$ $b \to J/\psi X$	$(5.96 \pm 0.03) \times 10^{-2}$ 0.0116	0.5
$b\bar{b} \to J/\psi\mu^+\mu^-$	n/a	n/a	0.0005

Table 6.2: Correction factors for the individual samples are shown above. Branching fractions are obtained from [8]

In the signal samples only B_s^0 is generated, thus an additional factor of two is included to account for the missing $\bar{B}_s^0$ contribution. It is worth mentioning that the branching ratio for the inclusive decay[1] $B \to J/\psi X$ is not reliably defined, but PDG [8] states an approximate value.

6.1.1 Signal Samples

The signal samples used for this analysis are summarized in table 6.1. $B_s^0 \to J/\psi\phi$ and $B_s^0 \to \psi(2S)\phi$ and consists of 10 000 000 and 1 000 000 million events. At the EventLoop level, requirements for the reconstruction of the $B_s^0 \to J/\psi(\psi(2S))\phi$ are done in the production of the DAODs. The candidates are reconstructed by first fitting two oppositely charged muons to common vertex forming a J/ψ candidate followed by the reconstruction of two oppositely charged hadron tracks, K^+K^-, forming a ϕ meson. For the fitting of the muon tracks to a common vertex it is required that the χ^2/dof[2] ≤ 8 and is done by reconstruction algorithm, `SelectOnia2mumu`, making use of both the Muon Spectrometer and the Inner Tracking Detector. For the reconstruction of the $\psi(2S) \to \mu^+\mu^-$ the procedure is done in the same manner as with the $J/\psi \to \mu^+\mu^-$ reconstruction only with a different mass hypothesis.

The oppositely charged hadrons, which are to be combined with the $J/\psi(\psi(2S))$ vertex, are required to have a transverse momentum $p_T > 800$ MeV/c and a reconstructed invariant mass of $m_\phi - 100$ MeV/c^2 $< m_{K^+K^-} < m_\phi + 100$ MeV/c^2, where $m_\phi = 1019.445$ is the reference mass of the ϕ meson reported by the Particle Data Group [8]. The χ^2/dof of the vertex fit is the same as for the $J/\psi(\psi(2S))$ vertex

[1] Which has to be corrected for due to the way the job options was implemented. This was needed to account for cascades as $b \to \chi_{c1} \to J/\psi$ etc.

[2] dof = Degrees-of-freedom

reconstruction. Finally, the reconstructed invariant mass of the B_s^0 candidate is required to be within 5000 MeV/c^2 $< m_{B_s^0} <$ 5800 MeV/c^2. All the reconstructed tracks are required to have a pseudorapidity coverage of $|\eta| \leq 3$ in order to remove tracks outside the fiducial volume of the detector.

The signal region is defined as $\pm 3\sigma$ around the signal peak. The invariant mass of the B_s^0 has been modeled by the sum of two Gaussian distributions centered around the same mass $m_{B_s^0}$, denoting the mean. The resulting probability distribution function (PDF) is fitted to unbinned data by maximizing the likelihood function

$$L = \prod_{i=1}^{N} f_{\mathrm{c}} G_{\mathrm{c}}(m^i_{\psi\phi}) + +(1 - f_{\mathrm{c}}) G_{\mathrm{t}}(m^i_{\psi\phi}) \tag{6.3}$$

where f_k (k = c,t[3]) are the fractions of the contributing Gaussian PDFs. The reconstructed invariant mass of the $\psi\phi$ pair is written as $m^i_{\psi\phi}$ where, for simplicity, $\psi = J/\psi, \psi(2S)$. The Gaussians G_k are defined as

$$G_k = (m^i_{\psi\phi}) = \frac{1}{\sigma_k \sqrt{2\pi}} \exp\Big[- \frac{(m^i_{\psi\phi} - m_{B_s^0})}{2\sigma_k^2} \Big] \tag{6.4}$$

where σ_k denotes the widths and its weighted sum is used to determine the signal region. The lower and higher mass regions are referred to as the lower and upper sidebands, respectively. The 3σ signal region is obtained by integrating the PDF to retain 99.7% of all events. The σ_w is the resulting standard-deviation from this integration.

The obtained regions for the B_s^0 is shown in table 6.3.

	$m_{B_s^0}$	σ_w	Signal Region	Lower Sidebands	Upper Sidebands
$B_s^0 \to J/\psi\phi$	5367.74 ± 0.02	$28.3 \pm .8$	$5283 - 5453$	$5084 - 5283$	$5453 - 5782$
$B_s^0 \to \psi(2S)\phi$	5367.45 ± 0.07	$20.5 \pm .8$	$5306 - 5429$	$5093 - 5306$	$5429 - 5774$

Table 6.3: Results of the fitting of the reconstructed invariant B_s^0 mass. All values are given in MeV/c^2.

[3]Indices c and t represent the core and the tail of the Gaussians, respectively.

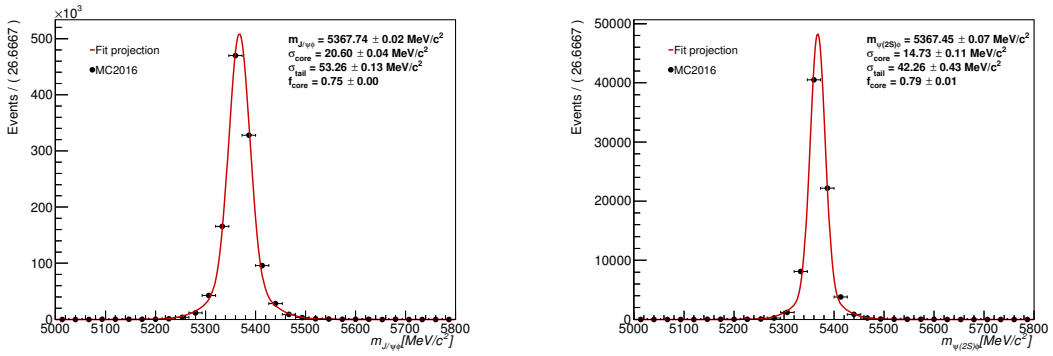

(a) **(b)**

Figure 6.1: Reconstructed invariant B_s^0 mass for **a)** $B_s^0 \to J/\psi\phi$ and **b)** $B_s^0 \to \psi(2S)\phi$

6.2 Background Samples

Before looking at actual data, the MC background samples are used to extract a background model in correspondence to what we might observe in the real dataset collected by the detector. The signals $B_s^0 \to J\psi\phi$ and $B_s^0 \to \psi(2S)\phi$ both have specific signatures enabling us to separate them from background contamination. The background samples are reconstructed in the same manner as the signal samples by reconstructing two oppositely charged muons to a common vertex forming the J/ψ or $\psi(2S)$. Two oppositely charged hadron tracks are then combined to, in practice, the same vertex as the J/ψ or $\psi(2S)$. In order to avoid double counting the signal samples are truth-matched using the `truthTree` stored in the NTuples. The same holds for the combinatorial $b\bar{b} \to \mu^+\mu^- X$ sample where any truth-matched J/ψ or $\psi(2S)$ are removed. Background samples used for this analysis are shown in table 6.1 and are summarized here. Recall that the X represent any possible hadron.

Direct J/ψ production; $pp \to J/\psi X$

The cross section for producing J/ψs in proton-proton collision is rather high, due to the contribution of several QCD processes [50], making this the dominant contribution of the background samples. As the J/ψ has very short lifetime ($\tau = 7.2\times10^{-21}$s) its decay length is close to zero. This can be exploited by the fact that the lifetime of the B_s^0 is, in comparison, rather large ($\tau = 1.5 \times 10^{-12}$s). It therefore has an observable separation between the primary and secondary vertex. Due to the fact that the spatial resolution in the xy-plane in the ATLAS detector is much better

than in the longitudinal z-direction [51], we commonly refer to this separation as L_{xy} or the transverse decay length.

Combinatorial $b\bar{b}$ background; $b\bar{b} \to \mu^+\mu^- X$

In this sample there are no J/ψs present but the two oppositely charged muons, arising from different processes, are combined with two oppositely charged hadron tracks. The main contributing source to the production of muons comes from the semi-leptonic decay of the b-quark proceeding in the following way $b \to c\mu^-\bar{\nu_\mu}$ or $\bar{b} \to \bar{c}\mu^+\nu_\mu$. The produced c-quarks hadronize to form charmed meson or may contribute through the semi-leptonic decay channel $c \to s\mu^-\bar{\nu_\mu}$. If the production of charmed mesons arises they can further contribute to the production of muons through a semi-leptonic decay channel.

Such decays can be separated by investigating the χ^2 distribution as there is no correlation of the goodness of fit for muon reconstruction as they originate from random processes. It is also efficient to place a criterion on the angle between the transverse momentum of the reconstructed B_s^0 meson and the L_{xy} vector, which shall be referred to as the pointing angle α. This is due to the fact that this angle should, in principle, be uniformly distributed as the correlation between p_T and L_{xy} is absent - which is not the case for the signal samples as the boosted B_s^0 leaves a clear signature for the α peaking at zero radians.

Inclusive J/ψ decays; $b\bar{b} \to J/\psi X$

The inclusive sample where $b\bar{b}$ is combined to a J/ψ and a hadron X mimics the signal and are therefore rather difficult to separate. Decay topologies identical to that of the signal mode may occur if the reconstructed hadron is combined with exactly two tracks whereas both of them are charged. For a few modes, the reconstructed four-particle mass may lie in the region of the B_s^0 mass. Such a decay is the $B_s^0 \to J/\psi f_0(980)$ and $B_s^0 \to \psi(2S) f_0(980)$ and is commonly referred to as *peaking background*.

6.3 Selection criteria

6.3.1 Generic requirements

After the requirements imposed at the EventLoop-level, explained in 6.1.1, has been applied selection criteria advised by the Inner Tracking Detector [51] and the Combined Performance (CP) groups [52] are applied at the NTuple level. The sum of all of these selection requirements are referred to as the *generic requirements*. These recommendation have been derived using 2016 reprocessed data, 2017 data from Tier-0 processing, and MC16 Monte Carlo [52]. The generic cuts are summarized in the table below.

	$\lvert\eta\rvert$	p_T	Silicon Hits	SCT Hits
Muons	< 2.3	≥ 4 GeV/c	-	≥ 5
Kaons	< 2.5	≥ 500 MeV/c	≥ 7	-
	Silicone SH[a]	Silicone Holes	Pixel Holes	Pixel Hits
Muons	-	≤ 2	-	≥ 1
Kaons	≤ 1	≤ 2	≤ 1	-

Table 6.4: Generic requirements. Events that satisfy these criteria are kept.

[a]Silicone SH: Shared hits in the Silicone detector

6.3.2 Muon reconstruction

For the reconstruction of the $B_s^0 \to J/\psi\phi$ an event must contain at least one reconstructed primary vertex (PV), which are formed from at least four inner detector tracks. In addition to this, at least one pair of muon candidates of oppositely charge are reconstructed by the use of both the muon system (MS) and the inner detector (ID). The muon candidates are reconstructed by the use of two different algorithms

- **Combined Reconstruction** where the muons are indentified by the use of a combination of the muon system and the inner detector track
- **Segment-tagged Reconstruction** where the muons are formed from a MS track segment which is not associated with a MS track but is rather matched to an ID track and further extrapolated to the MS.

After the reconstruction of two oppositely charged muons to a common vertex, the invariant mass of the muon pair is calculated form the refitted track parameters

[31]. As the J/ψ and the $\psi(2S)$ mass resolution varies in different parts of the detector, the candidates are divided three different subsets according to the di-muon pseudorapidity η. The regions are as follows

- **B**arrel-**B**arrel (**BB**) where both muons have a $|\eta| < 1.05$
- **E**nd-cap-**B**arrel (**EB**) where one muon have a $1.05 < |\eta| < 2.5$ (end-cap) and the other $|\eta| < 1.05$ (barrel)
- **E**nd-cap - **E**nd-cap (**EE**) where both muons have a $|\eta| < 1.05$ and the other $1.05 < |\eta| < 2.5$

Where the invariant di-muon mass is poorest in the **EE** region as these muons covers a larger distance before being stopped in the MS.

6.3.3 J/ψ and $\psi(2S)$ candidate selection

After passing the generic requirements an unbinned maximum-likelihood fit is performed for each pseudorapidity class to extract fit parameters as the weighted standard deviation and the J/ψ and the $\psi(2S)$ invariant mass. The signal J/ψ and $\psi(2S)$ events are modeled with two Gaussian functions, defined by

$$G_i = (m^i_{\mu\mu}) = \frac{1}{\sigma_i\sqrt{2\pi}} \exp\Big[- \frac{(m^i_{\mu\mu} - m_\psi)}{2\sigma_i^2}\Big] \tag{6.5}$$

where the same notation for fit parameters apply here as well. The $m^i_{\mu\mu}$ is the mass of the J/ψ ($\psi(2S)$) candidate and m_ψ is the mass of the fitted invariant J/ψ ($\psi(2S)$) mass. We require both Gaussian functions to be constraint by the same mean m_ψ. An optimization of the Likelihood function

$$L = \prod_{i=1}^{N} f_{\rm c} G_{\rm c}(m^i_{\mu\mu}) + (1 - f_{\rm c}) G_{\rm t}(m^i_{\mu\mu}) \tag{6.6}$$

yields the following fit parameters

	$m_{J/\psi)}^{MC}$ [MeV/c^2]	$\sigma_w^{J/\psi}$ [MeV/c^2]	$m_{\psi(2S)}^{MC}$ [MeV/c^2]	$\sigma_w^{\psi(2S)}$ [MeV/c^2]
BB	3098.00 ± 0.05	40.9 ± 0.2^a	3683.75 ± 0.16	57.2 ± 0.4
EB	3098.89 ± 0.14	54.3 ± 1.7	3684.27 ± 0.4	72.7 ± 2.1
EE	3099.69 ± 0.10	74.1 ± 1.1	3684.39 ± 0.32	95.3 ± 1.6
All η	3098.96 ± 0.05	58.2 ± 0.2	3684.39 ± 0.32	65.85 ± 1.1

Table 6.5: Fit results extracted from maximizing the likelihood function

[a]Uncertainties are calculated according to $\delta\sigma_w^{\psi} = \sqrt{\left(\frac{\partial\sigma_w^{\psi}}{\partial\sigma_c}\delta\sigma_c\right)^2 + \left(\frac{\partial\sigma_w^{\psi}}{\partial\sigma_t}\delta\sigma_t\right)^2 + \left(\frac{\partial\sigma_w^{\psi}}{\partial f_c}\delta f_c\right)^2}$

	BB [MeV/c^2]	**EB** [MeV/c^2]	**EE** [MeV/c^2]
J/ψ Signal Region	$2977 - 3212$	$2939 - 3255$	$2895 - 3302$
$\psi(2S)$ Signal Region	$3512 - 3855$	$3465 - 3902$	$3398 - 3970$

Table 6.6: Signal region for the J/ψ and $\psi(2S)$. These regions are set to retain 99.73 % of all J/ψ and $\psi(2S)$.

After performing the fit we define a signal region for the invariant mass of the J/ψ and the $\psi(2S)$ of $\pm 3\sigma_w$ chosen to retain $\sim$99.7% of all signal candidates. This requirement is then applied to both the signal and the background samples. The invariant mass distributions for the different pseudorapidity classes for J/ψ and $\psi(2S)$ are shown in figure 6.2 and 6.3, respectively.

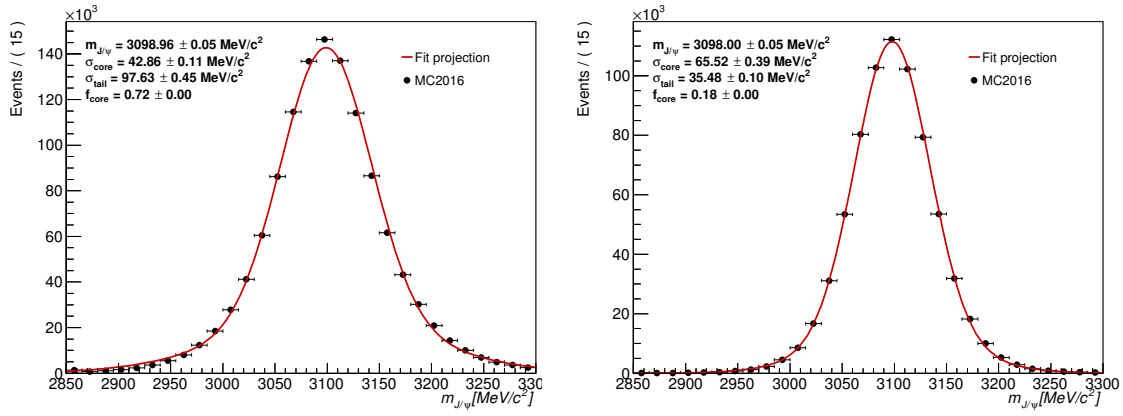

(a) Full $|\eta|$ coverage **(b)** Barrel-barrel region

Figure 6.2: **(a)** Shows the reconstructed invariant mass distribution of the J/ψ resonance for the full pseudorapidity coverage and **(b)** for the **BB** subset.

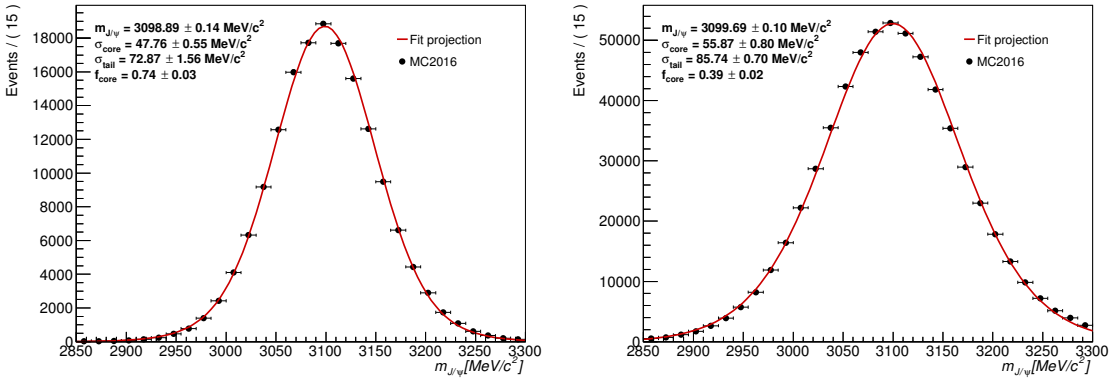

(a) End-cap barrel region **(b)** End-cap end-cap region

Figure 6.3: Shows the reconstructed invariant mass distribution for the J/ψ resonance for the **(a)** EB subset and for the **(b)** EE subset - clearly displaying the decrease in the resolution as the width broadens.

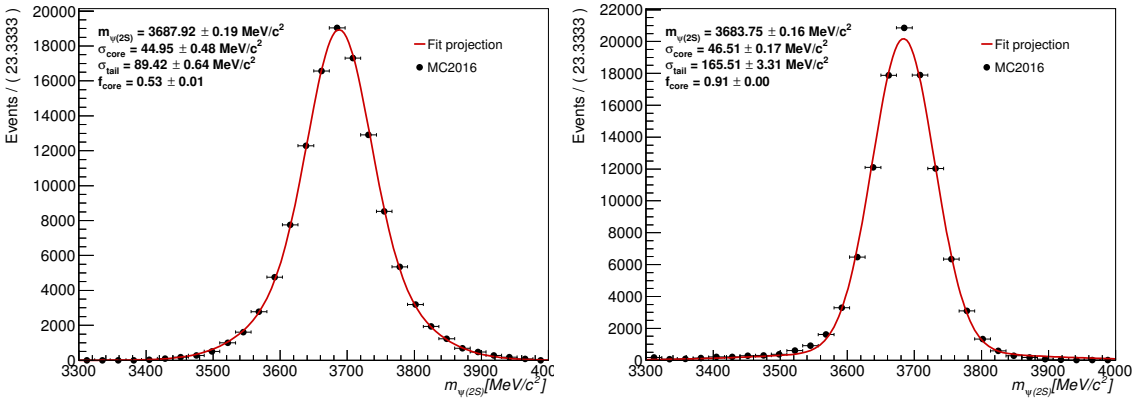

(a) Full $|\eta|$ coverage **(b)** Barrel-barrel region

Figure 6.4: **(a)** Shows the reconstructed invariant mass distribution for the $\psi(2S)$ resonance for the full pseudorapidity coverage and **(b)** for the **BB** subset.

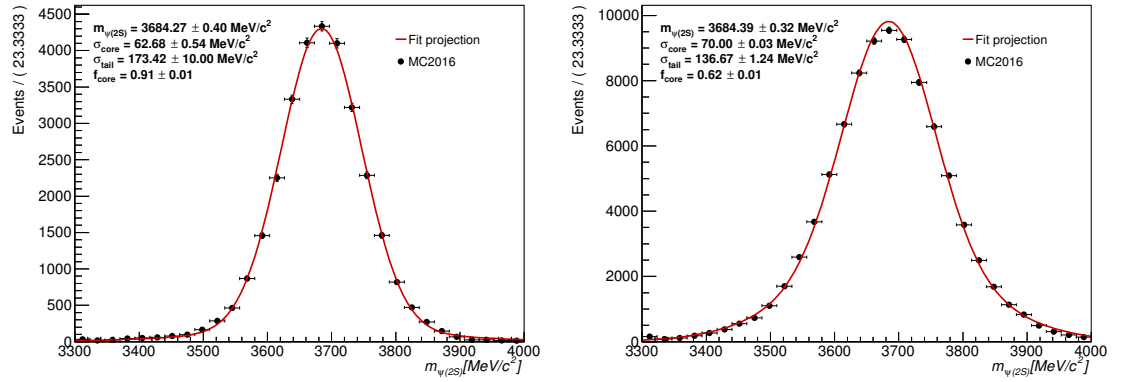

(a) End-cap barrel region **(b)** End-cap end-cap region

Figure 6.5: Shows the reconstructed invariant mass distribution for the $\psi(2S)$ resonance for the **(a)** EB subset and for the **(b)** EE subset - clearly displaying the decrease in the resolution as the width broadens.

6.3.4 ϕ Mass Candidate Selection

As described above, the $B_s^0 \to J/\psi(\psi(2S))$ are reconstructed by fitting candidate tracks from both $J/\psi \to \mu^+\mu^-$, $\psi(2S) \to \mu^+\mu^-$ and $\phi \to K^+K^-$ to a common vertex where the reconstructed invariant mass of $\mu^+\mu^-$-pair is constrained to the world averages $m_{J/\psi} = 3096.900 \pm 0.006$ MeV/c^2 and $m_{\psi(2S)} = 3686.097 \pm 0.025$ MeV/c^2 [8] for the J/ψ and $\psi(2S)$ resonance mode, respectively. To reject potential peaking background such as the $B_s^0 \to J/\psi f_0(980)$ or the $B_s^0 \to \psi(2S) f_0(980)$ mode we impose a constraint on the reconstructed invariant mass of the K^+K^- pair. This is done by the use of the MC signal sample after all the generic cuts have been applied.
The decay width of the ϕ resonance is well described by the a Breit-Wigner function convolved with a Crystal Ball[4] function when experimental effects as detector resolutions are considered.

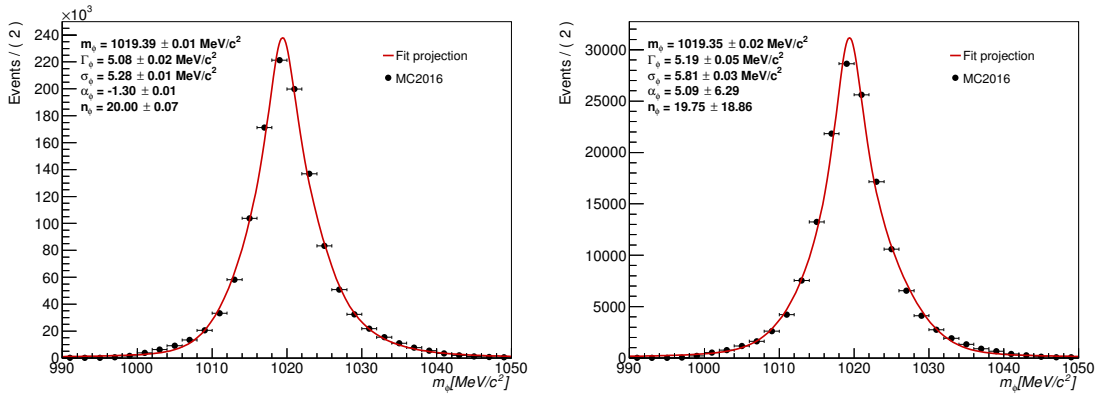

(a) $B_s^0 \to J/\psi K^+K^-$ **(b)** $B_s^0 \to \psi(2S)K^+K^-$

Figure 6.6: Reconstructed invariant mass of the K^+K^- pair fitted with after the generic requirements.

The relativistic Breit-Wigner distribution is given as

$$F_1(m_{KK}) = \frac{m_{KK}^2}{(m_{KK}^2 - m_\phi^2)^2 + \left(m_\phi^2 * \Gamma_\phi^2\right)^2} \tag{6.7}$$

where the m_{KK} is the ϕ mass candidate, m_ϕ is the fitted mean and Γ_ϕ is the width of the distribution. Further on, the Crystal Ball function combining a Gaussian core

[4]Named after the Crystal Ball collaboration, hence the capital letters

with a power law tail is given by

$$F_2(m_{KK}) = \begin{cases} \frac{1}{\sqrt{2\pi}\sigma_\phi} \exp[-\frac{(m_{KK}-m_\phi)^2}{2\sigma^2}] & \text{if } \frac{m_{KK}-m_\phi}{\sigma} > -\alpha \\ \frac{1}{\sqrt{2\pi}\sigma_\phi} \left(\frac{n_\phi}{|\alpha|}\right)^{n_\phi} \exp\left(-\frac{|\alpha|^2}{2}\right)\left(\frac{n_\phi}{|\alpha|} - |\alpha| - \frac{m_{KK}-m_\phi}{\sigma}\right) & \text{if } \frac{m_{KK}-m_\phi}{\sigma} \leq -\alpha \end{cases} \tag{6.8}$$

where the α determines the crossover between the Gaussian core and the power law distribution and n_ϕ describes length of the tail. By performing the fit of $F_1(m_{KK}) \otimes F_2(m_{KK})$ we obtain the distributions shown in figure 6.6. All parameters are left free in the fit and yields and m_ϕ is constrained to be the same for both F_1 and F_2.

	J/ψ mode	$\psi(2S)$ mode
m_ϕ	1019.38 ± 0.01	1019.35 ± 0.02
Γ_ϕ	5.08 ± 0.2	5.19 ± 0.05
σ_ϕ	5.28 ± 0.01	5.81 ± 0.03
α_ϕ	-1.3 ± 0.01	5.09 ± 6.29
n_ϕ	20.00 ± 0.07	19.75 ± 18.86

Table 6.7: Fit results for the invariant ϕ mass distribution. The mean m_ϕ, width Γ_ϕ and the standard deviation of the Gaussian core σ_ϕ are all given in units of MeV/c^2.

The fit yields a $m_\phi = 1019.38 \pm 0.01$ MeV/c^2 and $m_\phi = 1019.35 \pm 0.02$ MeV/c^2 for the J/ψ and $\psi(2S)$ mode respectively. We impose a signal region around the mean of the ϕ mass to be given as $\sim \pm 3\sigma_\phi$ rejecting a substantial amount of background events. For the J/ψ mode this implies a $3\sigma_\phi$ region of $m_\phi \in [1006\text{MeV}/c^2, 1034\text{MeV}/c^2]$ MeV/c^2 and $m_\phi \in [1002\text{MeV}/c^2, 1036\text{MeV}/c^2]$ for the $\psi(2S)$ mode. These regions have been obtained by requiring to retain 99.7% of all ϕ candidates. From the 2D scatter distributions, shown in figure 6.7b and figure 6.8b, it is quite evident that a great fraction of the background events fail to match the criteria of being within this signal region.

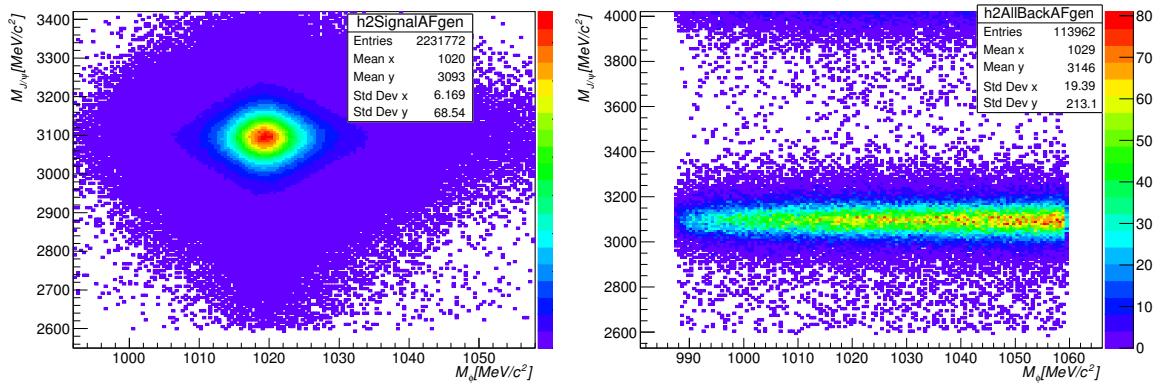

(a) Signal Sample **(b)** All the background model

Figure 6.7: Scatter plot of $m_{J/\psi}$ on y-axis and m_{ϕ} on the x-axis for **(a)** truth matched signal sample and **(b)** the combined background sample. Both after generic cuts.

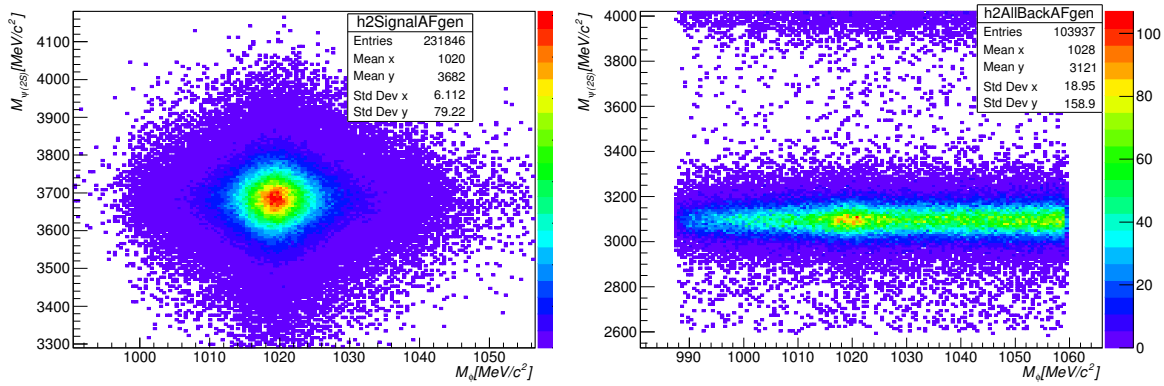

(a) Signal Sample **(b)** All the background model

Figure 6.8: Scatter plot of $m_{\psi(2S)}$ on y-axis and m_{ϕ} on the x-axis for **(a)** truth matched signal sample and **(b)** the combined background sample. Both after generic cuts.

These scatter plots gives a summary of the mass of the J/ψ and $\psi(2S)$ with respect to the ϕ mass after the generic requirements have been applied. As mentioned, quite a lot of the backgrounds are removed by requiring an event to be within the respective signal regions of the J/ψ, $\psi(2S)$ and ϕ. Looking at figure 6.8b it is rather clear to see that there are few events contaminating the $B_s^0 \to \psi(2S)\phi$ mode as there were no dedicated inclusive $B \to \psi(2S)X$ background sample available, which is evident to see in section 6.4. In order to further improve the sensitivity we perform an optimization of four discriminating variables discussed in section 6.4.

6.4 Sensitivity Study

In order to further suppress the background with respect to the signal events, four discriminating observables are chosen

- The transverse momentum of the B_s^0 meson, B_{pT}
- The χ^2/dof representing the goodness-of-fit for the four track vertex reconstruction
- The transverse decay length L_{xy} being the transversal separation between the primary and secondary vertex
- The pointing angle α

Due to the relatively long lifetime of the b quark, we make use of the fact that its distance from the primary vertex to the secondary vertex is separated by an observable decay length L. Since the position resolution in the xy-plane of the ATLAS detector is much better than the longitudinal, we chose only to investigate the transverse decay length L_{xy}. In the case of several primary vertexes, the one having the highest sum of the squares of the transverse momenta of the constituent tracks $\sum p_T^2$ is chosen. The transverse decay length may take negative values if its vector $\vec{L}_{xy}$ points in the opposite direction with respect to the B momentum vector $\vec{p}_T$. It then appears as the secondary vertex has been reconstructed behind the primary vertex.

In the reconstruction of the two oppositely charged hadron tracks and the two oppositely charged muon tracks to a common origin the associated χ^2 of the fit of these reconstructed tracks are calculated.

Another discriminating observable is the pointing angle α, equation 6.9, representing the angle between the B momentum vector $\vec{p}_T$ and the transverse decay length vector $\vec{L}_{xy}$

$$\alpha = |\phi_{p_T} - \phi_{L_{xy}}| \tag{6.9}$$

For signal events, we expect that the pointing angle is close to zero. Typically, for background events the correlation between the $\vec{p}_T$ and $\vec{L}_{xy}$ is absent resulting in a rather uniform distribution.

Below we can see the distributions for the observables before any cuts have been applied for the J/ψ mode. For the $\psi(2S)$ mode, see the appendix.

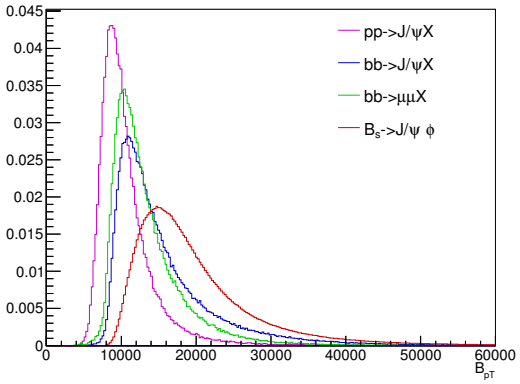

(a) Transverse momentum B_{pT} of the B meson

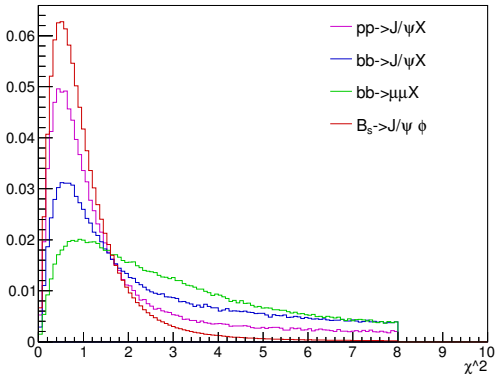

(b) Goodness-of-fit χ^2/dof

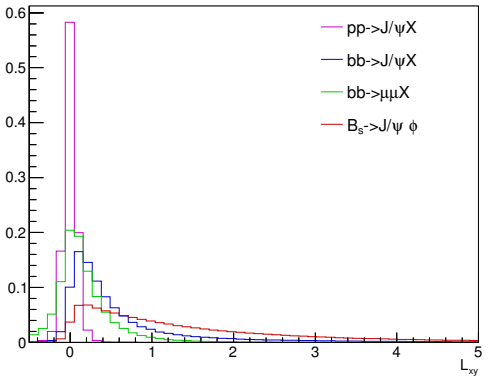

(c) Transverse decay length L_{xy}

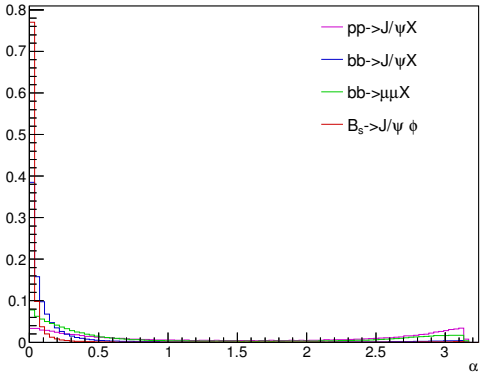

(d) Pointing angle α

Figure 6.9: Distribution of the observables for the Monte Carlo samples. All histograms are normalized to unity.

In figure b) we can see that the χ^2/dof is not uniformly distributed for the generic $b\bar{b} \to \mu^+\mu^- X$ sample even though the muons do not necessarily originate from the same vertex. However, this is to be expected as events, such as, $B \to \mu DX$, where subsequently the $D \to \mu X$ where the two resulting muons might still be reconstructed to the same vertex due to the shorter lifetime of the D meson. Another contribution may be events with the two muons arising from the same real vertex, e.g. form semileptonic $B \to \mu^+\mu^- X$ decays.

6.4.1 Optimization

The sensitivity study has been performed by the use of both MC signal and background samples and by the use of MC signal and data sidebands. At first the sensitivity $S/\sqrt{S+B}$ was optimized by the use of MC signal and MC background only and hence scaled respectively according to table 6.1. The procedure is as follows

1. first investigate the highest sensitivity of one of the discriminating observable with respect to the cut value
2. perform this optimized cut value on the next observable and redo 1.
3. determine the efficiency of the tested order and redo 1. and 2.

The order yielding the highest efficiency whilst suppressing the largest amount of background is chosen. In practice, this procedure begins with optimizing the sensitivity of the transverse momenta of the B_{pT}. The cut value yielding the highest signal to background separation is further imposed on the χ^2/dof. The sensitivity of χ^2/dof is then optimized with after imposing the best selection of B_{pT}. Next, the selection of L_{xy} is optimized after imposing the optimal selection criteria of the preceding observables. Finally, the pointing angle α is optimized after imposing the best selection criteria for B_{pT}, χ^2/dof and the L_{xy}.

The sensitivity plots for the $B_s^0 \to J/\psi\phi$ mode are shown below.

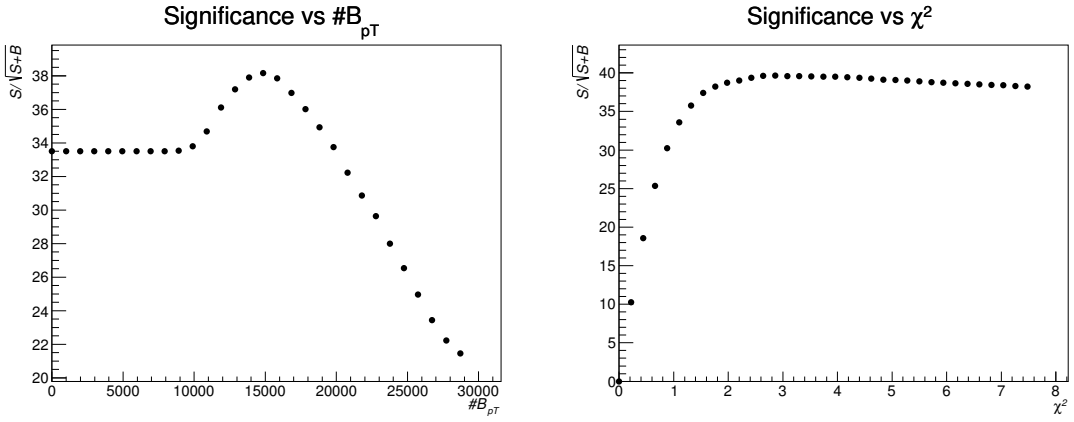

(a) B_{pT} for the J/ψ mode. **(b)** χ^2/dof for the J/ψ mode.

Figure 6.10: Distribution of the significance with respect to the cut value of the observable.

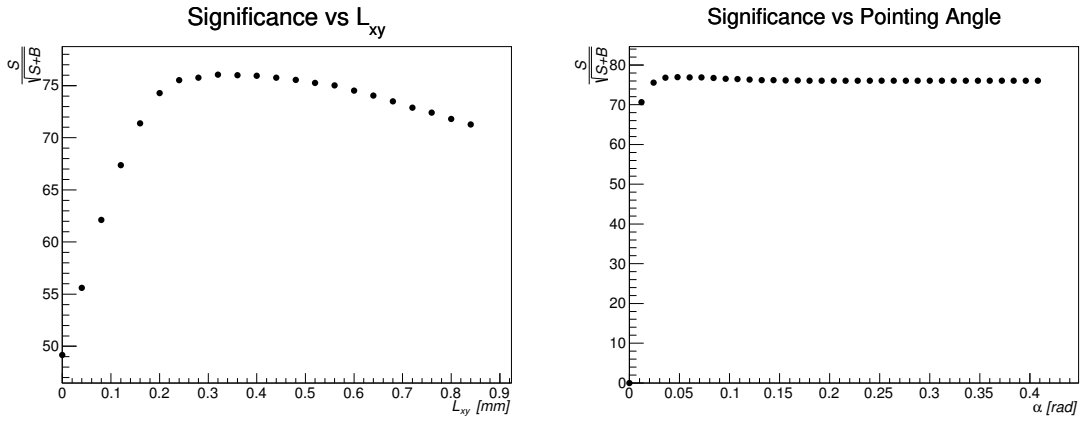

(a) L_{xy} for the J/ψ mode **(b)** α for the J/ψ mode

Figure 6.11: Distribution of the significance with respect to the cut value of the observable.

Briefly discussed in the last subsection, there is rather few background events contaminating the $B_s^0 \to \psi(2S)\phi$. Displayed in fig 6.8b, showing the scatter plot of the background events after the generic requirements, it is quite evident to see that most of the background events are thrown out by requiring a $\pm 3\sigma$ signal region for the invariant mass of the $\psi(2S)$. This makes it rather difficult to perform an optimization of the significance as there are too few background events to work with to obtain a clear distribution. The significance plot for the $\psi(2S)$ mode by the use of MC signal and background are shown below displaying the effects of low residual background statistics.

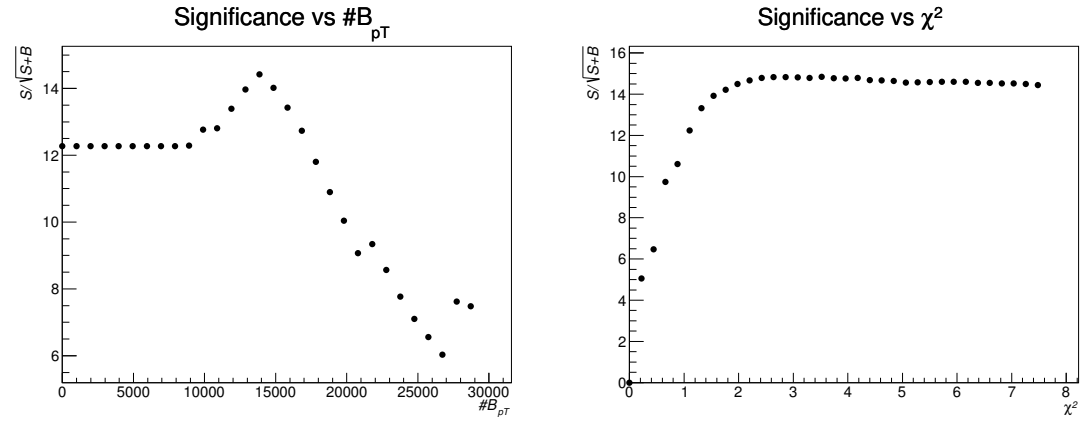

(a) B_{pT} for the $\psi(2S)$ mode. **(b)** χ^2/dof for the $\psi(2S)$ mode.

Figure 6.12: Distribution of the significance with respect to the cut value of the observable.

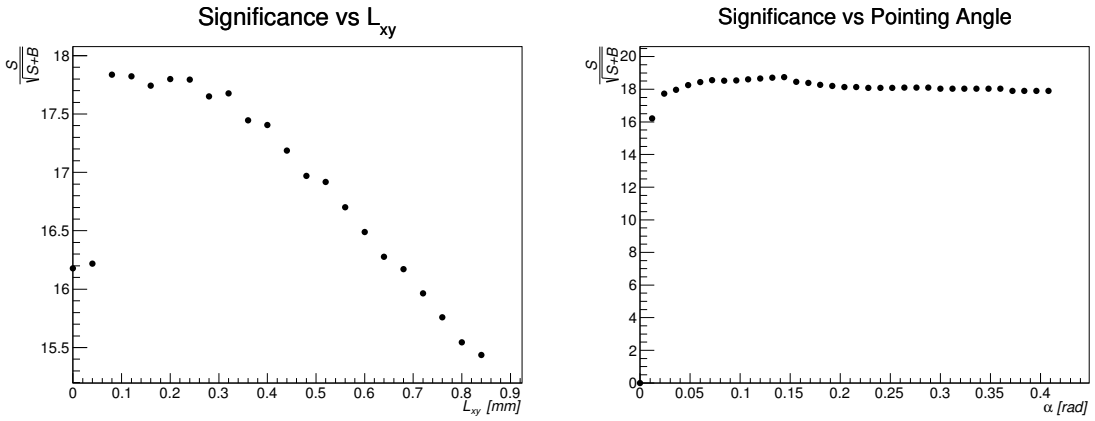

(a) L_{xy} for the $\psi(2S)$ mode. **(b)** All the background model

Figure 6.13: Distribution of the significance with respect to the cut value of the observable.

We can see a clear fluctuation for these distribution due to the low abundance of background events. Especially for the L_{xy} it is demanding to choose an optimal cut value. Motivated by this fluctuation we decided to use data sidebands instead for the background as it contains a larger range of processes and much higher statistics. This was done by selecting a $\pm 3\sigma_{SR}$ signal region for the invariant mass of the B_s^0 explained in detail in section 6.3.3. The beginning/end of the lower/upper sidebands were chosen by requiring the same amount of events in the lower and upper region. The signal Monte Carlo samples are scaled respectively to the integrated luminosity calculated by the ATLAS LumiCalc [53].

For the data sideband regions we fitted the J/ψ mass and performed a 3σ mass cut. As the ϕ has no present peak for the data sidebands we fitted the ϕ mass in the sidebands for the MC signal samples and further performed cuts on the data sidebands. Summarized below are the optimization plots for the J/ψ and $\psi(2S)$ mode in figure 6.14.

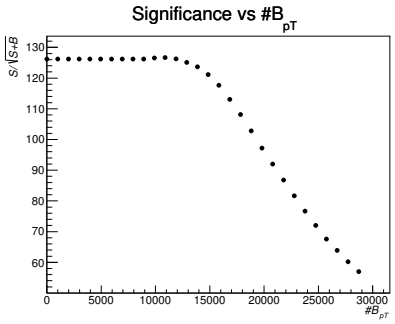

(a) B_{pT} for the J/ψ mode.

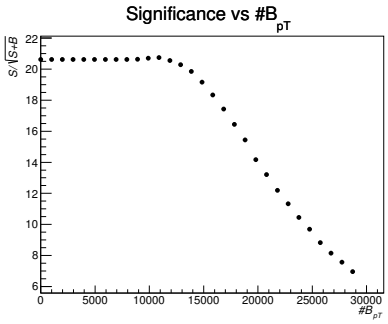

(b) B_{pT} for the $\psi(2S)$ mode.

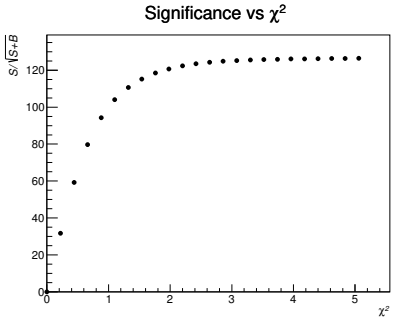

(c) χ^2/dof for the J/ψ mode.

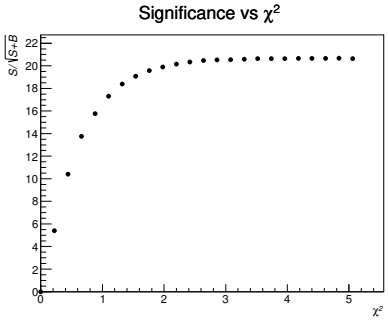

(d) χ^2/dof for the $\psi(2S)$ mode.

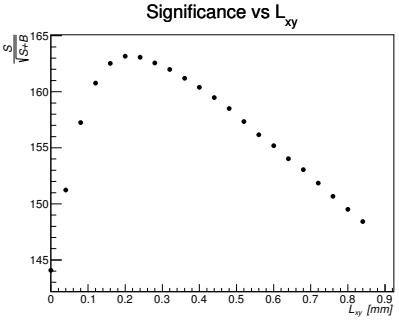

(e) L_{xy} for the J/ψ mode.

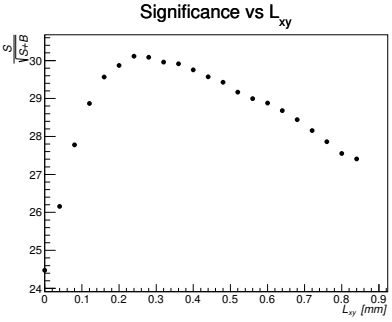

(f) L_{xy} for the $\psi(2S)$ mode.

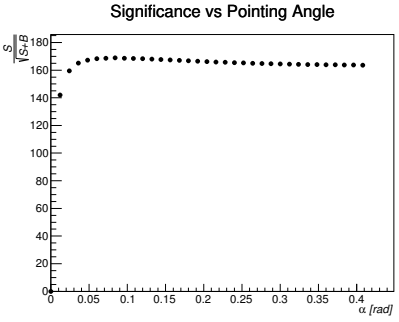

(g) α for the J/ψ mode.

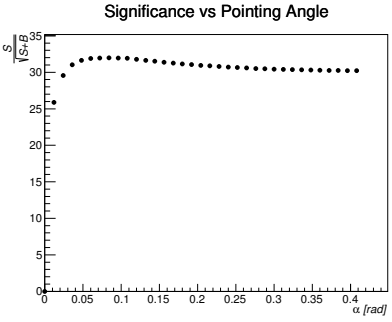

(h) α for the $\psi(2S)$ mode.

Figure 6.14: Distribution of the significance with respect to the cut values for the evaluated observables.

From this study we can obtain the optimal cut values for the discriminating variables. The results are summarized below.

	J/ψ mode	$\psi(2S)$ mode
B_{pT}	> 13000 MeV/c	> 13000 MeV/c
χ^2/dof	< 2.8	< 2.8
L_{xy}	> 0.26 mm	> 0.26 mm
α	$< .1$ rad	$< .1$ rad

Table 6.8: Values obtained from the optimization study. Both $B_s^0 \to J/\psi\phi$ and $B_s^0 \to \psi(2S)\phi$ yield the same values, which is to be expected.

6.4.2 Signal efficiency

In order to estimate the relative branching fraction information about the signal yield efficiency for each mode is needed. By making use of the truth-matched information of the generated MC events we can extract the signal efficiency ε by dividing the amount of events n passing the described requirements by the amount of generated events N

$$\varepsilon = \frac{n}{N} \tag{6.10}$$

with the corresponding uncertainty estimated by a binomial model [54],

$$\sigma_\varepsilon = \sqrt{\frac{\varepsilon(1-\varepsilon)}{N}} \tag{6.11}$$

Results of the efficiency for each cut for each mode is shown in table 6.9.

	Type of Cut	$B_s^0 \to J/\psi\phi$	$B_s^0 \to \psi(2S)\phi$
		Efficiency ε	
After EventLoop		$63.05\% \pm 0.02\%$	$65.06\% \pm 0.05\%$
Trigger	`HLT_mu6_mu4_bJpsimumu_delayed`	$21.1\% \pm 0.01\%$	$22.47\% \pm 0.04\%$
Generic Cuts	Truth Matching	$20.66\% \pm 0.01\%$	$21.72\% \pm 0.04\%$
	K^+K^- η Cut	$20.57\% \pm 0.01\%$	$21.66\% \pm 0.04\%$
	$\mu^+\mu^-$ p_T Cut	$20.00\% \pm 0.01\%$	$21.08\% \pm 0.04\%$
	$\mu^+\mu^-$ pixel & SCT	$19.89\% \pm 0.01\%$	$20.97\% \pm 0.04\%$
	K^+K^- pixel & SCT	$19.56\% \pm 0.01\%$	$20.60\% \pm 0.04\%$
	K^+K^- SH	$19.55\% \pm 0.01\%$	$20.60\% \pm 0.04\%$
	K^+K^- Silicon Holes	$19.55\% \pm 0.01\%$	$20.60\% \pm 0.04\%$
	$\mu^+\mu^-$ η Cut	$19.01\% \pm 0.01\%$	$19.93\% \pm 0.04\%$
Mass Cut	ϕ Mass	$18.44\% \pm 0.01\%$	$19.55 \pm 0.04\%$
	$J/\psi, \psi(2S)$ EE region	$18.34\% \pm 0.01\%$	$19.45\% \pm 0.04\%$
	$J/\psi, \psi(2S)$ BB region	$18.08\% \pm 0.01\%$	$19.26\% \pm 0.04\%$
	$J/\psi, \psi(2S)$ EB region	$18.05\% \pm 0.01\%$	$19.23\% \pm 0.04\%$
Optimized cuts	B_{pT}	$17.82\% \pm 0.01\%$	$18.9\%6 \pm 0.04\%$
	χ^2	$16.96\% \pm 0.01\%$	$18.05\% \pm 0.04\%$
	L_{xy}	$14.77\% \pm 0.01\%$	$15.71\% \pm 0.04\%$
	α	$14.70\% \pm 0.01\%$	$15.63\% \pm 0.04\%$
	After All Cuts	$14.70\% \pm 0.01\%$	$15.63\% \pm 0.04\%$

Table 6.9: Showing the efficiencies for each cuts applied for the signal samples.

After all the selection criteria has been applied the efficiency yield is $14.70\% \pm 0.01\%$ and $15.63\% \pm 0.04\%$ for the J/ψ mode and the $\psi(2S)$ mode, respectively. The largest contribution is the from the is from the `HLT_mu6_mu4_bJpsimumu_delayed` trigger and must therefore be accounted properly. The generic requirements, making sure we have a quality track, reduces the efficiency by a few %. The mass cuts are highly efficient with regards to the removal of background events and only reduces the efficiency by $\sim 0.3\% - 0.4\%$ for the signal samples. This is an especially efficient cut for the $\psi(2S)$ mode. In the next section we investigate the signal and background model of the events passing the requirements shown in table 6.9. The efficiency ratio obtained after all the selection criteria have been applied is $\varepsilon_{\psi(2S)\phi}/\varepsilon_{J/\psi\phi} = 94.05 \pm 0.25\%$.

6.4.3 Signal Model

After all the aforementioned cuts have been applied we can extract a signal model for the B_s^0. The signal model for the B_s^0 for the J/ψ and $\psi(2S)$ mode have been modeled by two Gaussian PDF's constraint to the same mean $m_{B_s^0}$. Below we can see the signal model for the J/ψ and $\psi(2S)$ mode

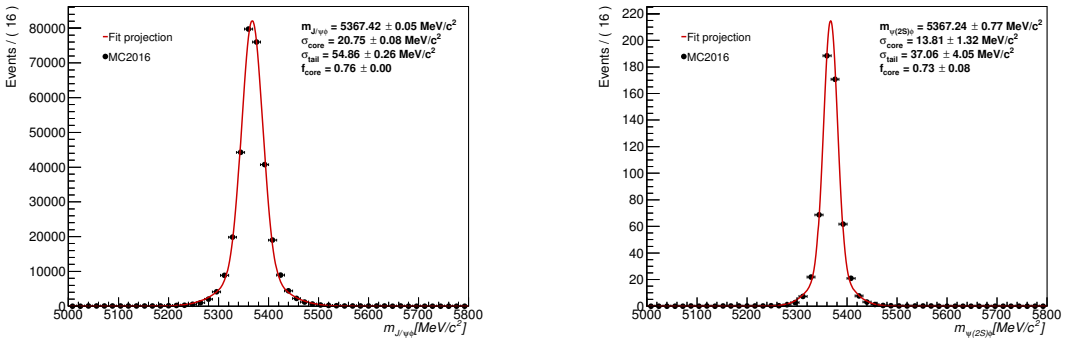

(a) **(b)**

Figure 6.15: Reconstructed invariant B_s^0 mass for **a)** $B_s^0 \to J/\psi\phi$ and **b)** $B_s^0 \to \psi(2S)\phi$

where the same PDF distribution as in equation 6.3 is used. We notice the differences in the resolution of the invariant B_s^0 mass for the J/ψ and $\psi(2S)$ mode. This is consistent with the energy released in the decays and is to be expected in the data as well.

The contribution of the non-truth matched events to the full signal model has also been studied. This is the case where at least one of the tracks fails to be picked up correctly by the reconstruction algorithm. As this only occurs $\sim$ .44% and $\sim$ .42% of all correctly reconstructed J/ψ and $\psi(2S)$ events, respectively, it does not significantly contribute to the full signal model and our signal distribution is still described well by the double Gaussian function. This has been investigated thoroughly both on MC and data.

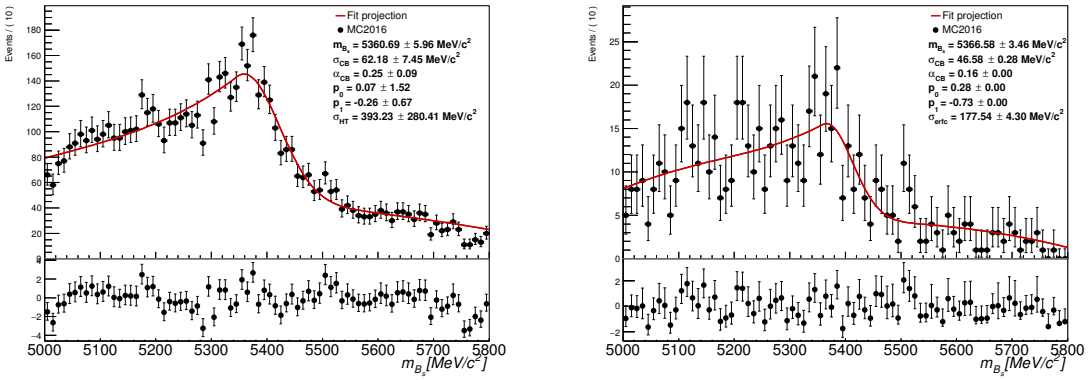

(a) **(b)**

Figure 6.16: Non-truth matched B_s^0 mass for **a)** $B_s^0 \to J/\psi\phi$ and **b)** $B_s^0 \to \psi(2S)\phi$

The non-truth matched B_s^0 events are modeled by a set of two different PDFs. The J/ψ mode is described by a second order Chebychev polynomial of the first kind , a Crystal Ball function equation (6.8) and a hyperbolic tangent function. The second order Chebychev polynomial [55] of the first kind is given by

$$F^{chev}(m_{\psi\phi}) = 2p_1(m_{\psi\phi})^2 - p_0 m_{\psi\phi} \tag{6.12}$$

where we use the same notatation, $\psi = J/\psi,\ \psi(2S)$. The non-truth matched B_s^0 events for the $\psi(2S)$ modeled by the Chebychev, Crystal Ball and a complementary error function (ERFC) given by

$$\mathrm{erfc}(x) = \frac{2}{\sqrt{\pi}} \int_x^\infty e^{-t^2} dt, \qquad x = \frac{m_{\psi\phi} - \mu_{\mathrm{erfc}}}{\sigma_{\mathrm{erfc}}} \tag{6.13}$$

The origin of the visible peak seen in 6.16 may be due to background events, such as the $B_d^0 \to J/\psi K^*$, which passes the non-truth matching and the selection criteria. Another contribution may be due to sudden change of the J/ψ PDG code [5] for the MC16 sample used for this analysis. Although the signal samples has been generated with the present PDG code, secondary events with the old PDG code may still be present and will not be identified correctly by the truth-matching. This happens rather rarely and only occurs in 0.013‰ of the cases for the J/ψ mode and none of the cases for $\psi(2S)$ mode.

[5]The PDG code is a Monte Carlo numbering scheme for particles intended to facilitate interfacing between event generators (e.g. HERWIG, PYTHIA and SHERPA), detector simulations and analysis packages [56]

6.4.4 Background Model

The residual background events passing all criteria are further studied to extract a background model. Due to the poor statistics of the MC background after applying all the requirements, discussed above, for the $\psi(2S)$ mode, we decided to perform sideband studies of data to extract a model. For the J/ψ mode we are left with enough events after all the requirements to develop a simple model. Data sideband study is then performed to verify the extracted model for the J/ψ mode.

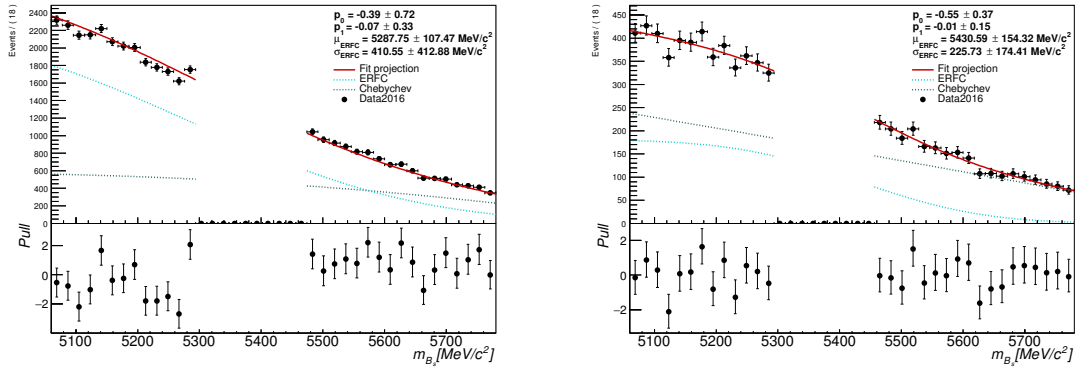

(a) $B_s^0 \to J/\psi\phi$ data sideband **(b)** $B_s^0 \to \psi(2S)\phi$ data sideband

Figure 6.17: Data sidebands for B_s^0 mass for **a)** $B_s^0 \to J/\psi\phi$ and **b)** $B_s^0 \to \psi(2S)\phi$

The background distribution is modeled on the sideband regions due to the low statistics of the remaining Monte Carlo simulated background events. The fit model describing the distributions shown in 6.4.4 are given by

$$F_{\text{back}}(m_{\psi\phi}) = f_{chev} F_{back}^{chev}(m_{\psi\phi}) + f_{ERFC} F_{back}^{ERFC}(m_{\psi\phi}) \tag{6.14}$$

where $F_{back}^{chev}(m_{\psi\phi})$ is the second order Chebychev polynomial of the first kind given in eq. 6.12 and $F_{back}^{ERFC}(m_{\psi\phi})$ is the complementary erfc(x) given by eq. 6.13. Further on, f_{chev} and f_{ERFC} is the fraction of the contributing PDFs.[6] .

Illustrated in figure 6.18 we see the MC residual background distribution for the J/ψ mode. Due to the low statistics after applying all selection criteria it is hard to determine a rather complex background model which may be more suitable description of the actual data. The background distribution developed from MC studies is a second order Chebychev polynomial of the first kind yielding the best χ^2 of 1.28. This background model is investigated in the systematic uncertainties 7.3.3.

[6]The fractions of the contributing PDFs sums to unity $f_{chev} + f_{ERFC} = 1$

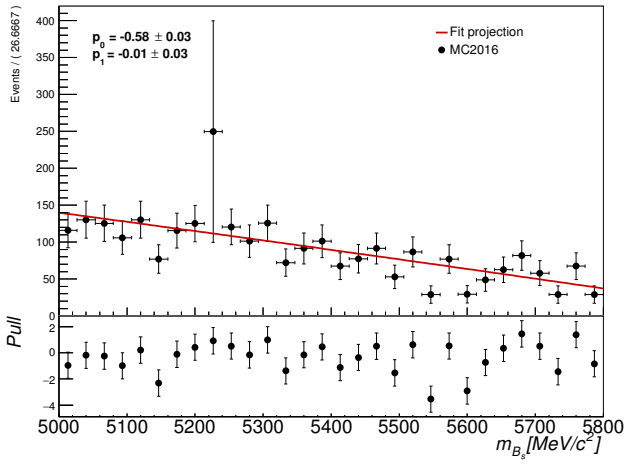

Figure 6.18: Monte Carlo background sample for the J/ψ mode

The fit parameters for the data sidebands yield $p_0 = -0.39 \pm 0.72$, $p_1 = -0.07 \pm 0.33$ for the J/ψ mode and $p_0 = -0.55 \pm 0.37$ and $p_1 = -0.01 \pm 0.15$ for the $\psi(2S)$ mode for the Chebychev fit. In fig 6.19 we can see the combined model with the use of Monte Carlo signal and data sidebands.

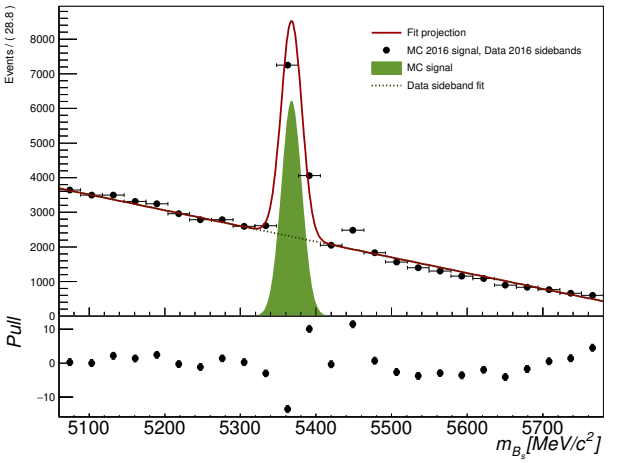

Figure 6.19: Combined model for the J/ψ mode

The total model for both modes, which in section 7.3.3 will be referred to as the base model, is given as

$$F_{B_s^0}(m_{\psi\phi}) = N_{sig}F_{sig}(m_{\psi\phi}) + N_{back}F_{back}(m_{\psi\phi}) \tag{6.15}$$

where $F_{sig}(m_{\psi\phi})$ and $F_{back}(m_{\psi\phi})$ are defined above and N_{sig} and N_{back} are the signal and background yields, respectively.

Chapter 7

Measurement of the Relative Branching Fraction

After extracting suitable selection requirements from the simulated Monte Carlo samples we proceed with the study on data originating from proton-proton collisions collected by the ATLAS detector. This chapter presents the first measurement of the relative branching fraction

$$\frac{\mathcal{B}(B_s^0 \to \psi(2S)\phi)}{\mathcal{B}(B_s^0 \to J/\psi\phi)} = \frac{N_{\psi(2S)\phi}}{N_{J/\psi\phi}} \frac{\mathcal{B}(J/\psi \to \mu^+\mu^-)}{\mathcal{B}(\psi(2S) \to \mu^+\mu^-)} \frac{\epsilon_{J/\psi\phi}}{\epsilon_{\psi(2S)\phi}} \tag{7.1}$$

with the use of Run 2 data corresponding to an integrated luminosity 4.08 fb^{-1}. The B_s^0 mass is also measured for each mode. Using truth-matched Monte Carlo signal samples the efficiency ratio $\epsilon_{J/\psi\phi}/\epsilon_{\psi(2S)\phi}$ is extracted. Further on, the signal yields $N_J/\psi\phi$ and $N_{\psi(2S)\phi}$ are extracted from the fit models discussed in section 6.4.4.

7.1 J/ψ extraction and $\psi(2S)$, ϕ evaluation

Described in section 6.3.2, the J/ψ candidates are divided into three classes according to the pseudorapidity of the muons. Before applying all the selection criteria obtained from the MC study on the actual data, we compare the J/ψ mass distribution from the MC with the one from the data. This is done by performing an unbinned fit of the maximized likelihood function explained in more detail in

section 6.3.2. We use the same signal model as for the MC, but introduce a first order polynomial as the linear background model for the J/ψ.

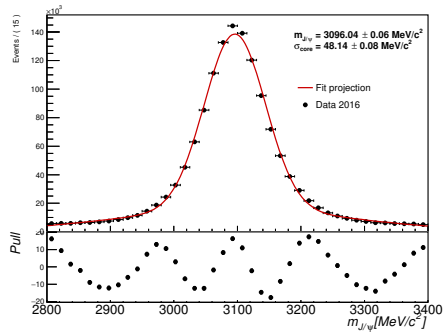

(a) Full η coverage

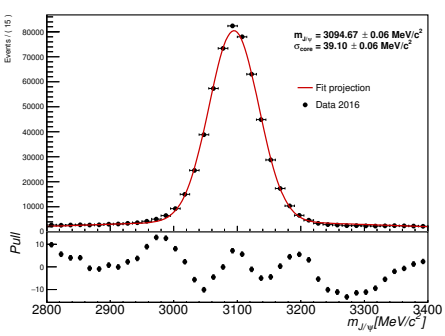

(b) Barrel Barrel region

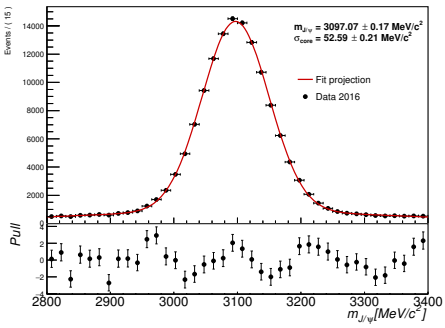

(c) End-cap Barrel region

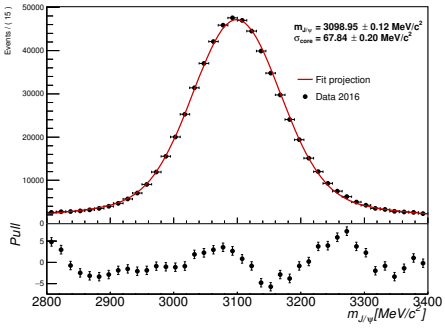

(d) End-cap End-cap region

Figure 7.1: Fit of J/ψ invariant mass distributions for data 2016.

Figure 7.1 shows the distribution and the fit projection of the J/ψ for each pseudorapidity class. The fit results are shown in table 7.1.

	BB	EB	EE	All η
$m_{J/\psi}$ [MeV/c^2]	3094.67 ± 0.06	3097.07 ± 0.17	3098.95 ± 0.12	3096.04 ± 0.06
$\sigma_w^{J/\psi}$ [MeV/c^2]	39.10 ± 0.06	52.59 ± 0.20	67.84 ± 0.20	48.14 ± 0.08

Table 7.1: Fit results extracted for the J/ψ for data 2016.

The fit results for the J/ψ mass and σ_w are in good agreement with the MC values. Next we define a 3σ region requiring the reconstructed invariant J/ψ mass to be within a signal window of 2977 MeV/c^2 $< m_{J/\psi} <$ 3212 MeV/c^2 for the barrel-barrel region, 2939 MeV/c^2 $< m_{J/\psi} <$ 3255 MeV/c^2 for the end-cap barrel region and, finally, 2895 MeV/c^2 $< m_{J/\psi} <$ 3302 MeV/c^2 for the end-cap end-cap region. For the $\psi(2S)$ mode, however, the signal region is defined by $\pm 3\sigma^{MC}_{\psi(2S)}$ signal region obtained from the MC study. For the ϕ mass, we use the signal region obtained from

the MC study as its peak is highly contaminated by surrounding processes. This is shown in figure 7.3a and figure 7.3b for the J/ψ and $\psi(2S)$ mode, respectively. The fit is performed with a linear background fit equation (7.2), same as for the $\psi(2S)$ mode, and a Breit-Wigner distribution, equation (6.7).

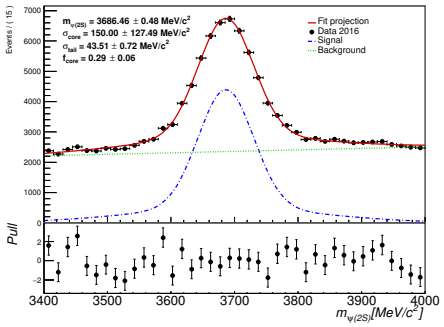

(a) Barrel barrel region

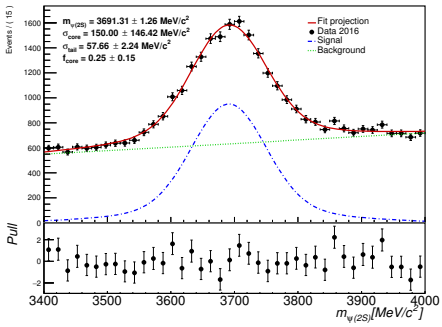

(b) End-cap barrel region

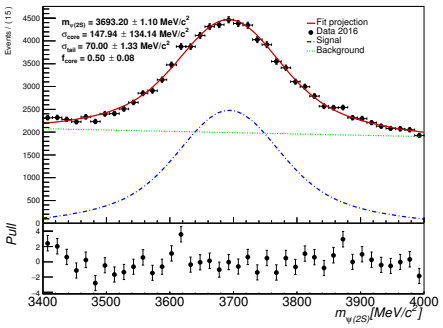

(c) End-cap end-cap region

Figure 7.2: Fit of $\psi(2S)$ invariant mass distributions for data 2016.

A fit of the $\psi(2S)$ mass distribution, shown in figure 7.2 has been performed by the use of two Gaussian functions constrained to the reconstructed di-muon mass and a second order polynomial of the form

$$B(m_{\mu^+\mu^-}) = 1 + \alpha m_{\mu^+\mu^-} + \beta(m_{\mu^+\mu^-})^2 \tag{7.2}$$

where the α and β are free fit parameters. The muon pair reconstructed to form the $\psi(2S)$ are required to be within following signal window 3512 MeV/c^2 $< m_{\psi(2S)} <$ 3855 MeV/c^2 for the barrel-barrel region, 3465 MeV/c^2 $< m_{\psi(2S)} <$ 3902 MeV/c^2 for the end-cap barrel region and, finally, 3398 MeV/c^2 $< m_{\psi(2S)} <$ 3970 MeV/c^2 for the end-cap end-cap region.

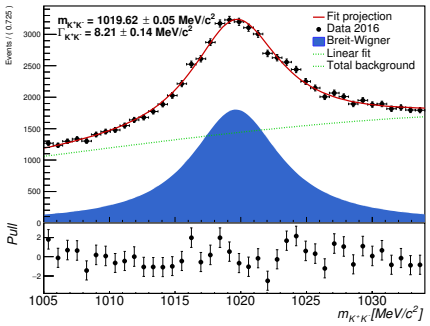

(a) Invariant-mass distribution for the reconstructed K^+K^- pair for the J/ψ mode.

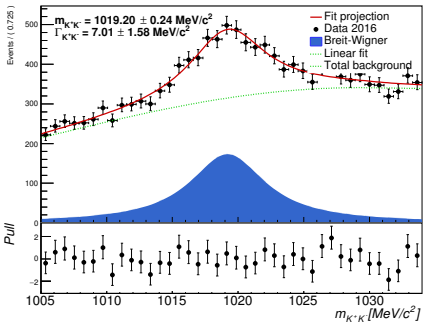

(b) Invariant-mass distribution for the reconstructed K^+K^- pairfor the $\psi(2S)$ mode.

Figure 7.3: Invariant-mass distribution for the reconstructed K^+K^- pair for the two decay modes.

In figure 7.4 we can see the scatter plot for data before any cuts have been applied, figure 7.4a, and after all the selection requirements have been applied for the J/ψ and $\psi(2S)$ mode, figure 7.4b and 7.4c, respectively.

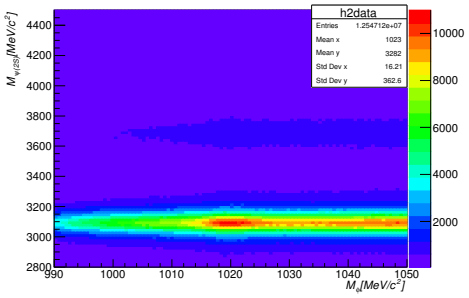

(a) Before any selection requirements have been applied.

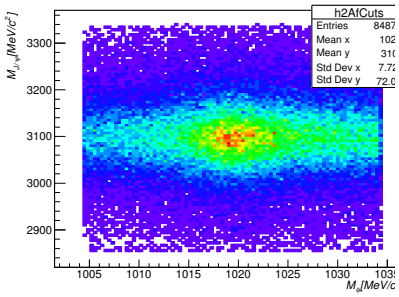

(b) J/ψ mode after all the cuts have been applied.

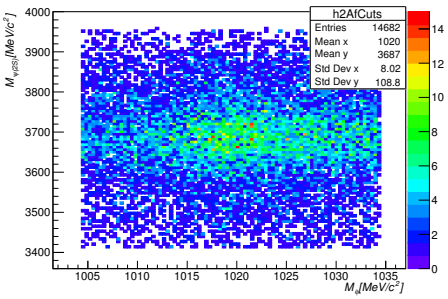

(c) J/ψ mode after all the cuts have been applied.

Figure 7.4: Scatter plot for the two modes with m_ψ, $\psi = J/\psi, \psi(2S)$ on the y-axis and m_ϕ on the x-axis.

7.2 Results of $B_s^0 \to J/\psi\phi$ and $B_s^0 \to \psi(2S)\phi$

After passing the generic requirements, the defined J/ψ,$\psi(2S)$ and ϕ $\pm 3\sigma$ signal regions and the optimization criteria, the residual events are fitted by the fit model described in section 6.4.4. In order to extract the mass and the amount of signal candidates for the B_s^0 an extended unbinned maximum-likelihood fit is performed. The contribution of fit model for non-truth matched or fake B_s^0, discussed in section 6.4.3, has been investigated on data. However, the contribution of this model on data is as negligible as on MC.

Figure 7.5 and 7.6 shows the invariant mass distribution of events passing all the aforementioned criteria for the J/ψ and $\psi(2S)$ mode, respectively.

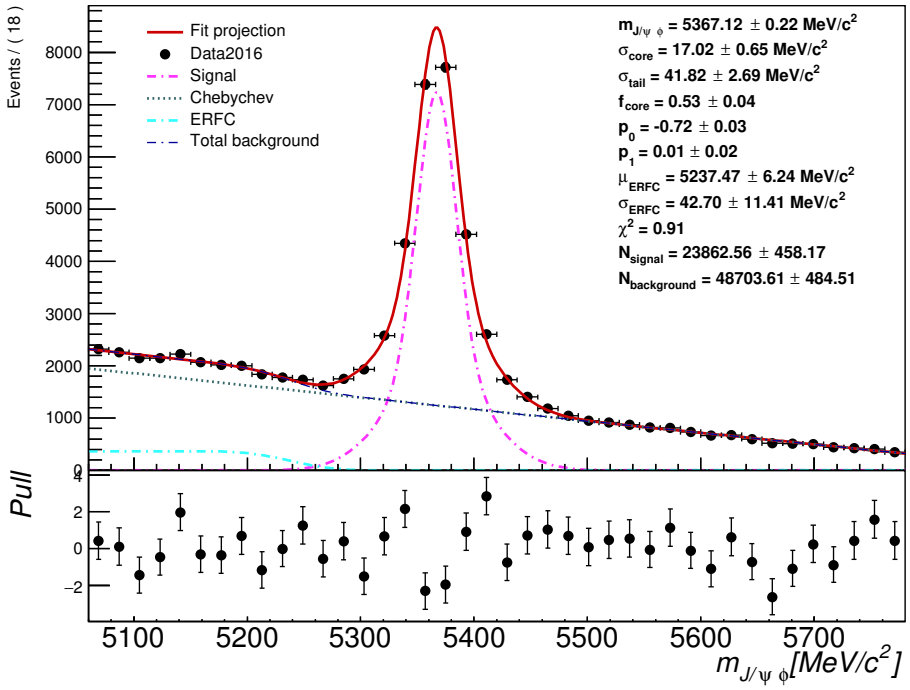

Figure 7.5: $B_s^0 \to J/\psi\phi$ mode

All parameters in the fit model defined in section 6.4.4 are left free in the fit. The parameters describing the signal shape of the fit model are the mean $m_{J/\psi\phi}$, the standard deviations for the tail σ_t and core σ_c of the gaussians and the corresponding fraction f_c. The parameters describing the background distribution are the Chebychev parameters p_0, p_1 and the mean and standard deviation of the complementary error function μ_{ERFC} and σ_{ERFC}, respectively. From this fit we extract a mass for the J/ψ mode of $m_{J/\psi\phi} = 5367.12 \pm 0.22$ MeV/c^2 and a signal yield of 23862.56 ± 458.17 and $m_{\psi(2S)\phi} = 5367.31 \pm 0.43$ MeV/c^2 and a signal yield of 1858 ± 13808 for the $\psi(2S)$ mode being in good agreement with the world average

stated by the Particle Data group $m_{B_s^0} = 5366.84 \pm 0.30$ MeV/c^2. The fit parameters are summarized in table 7.2.

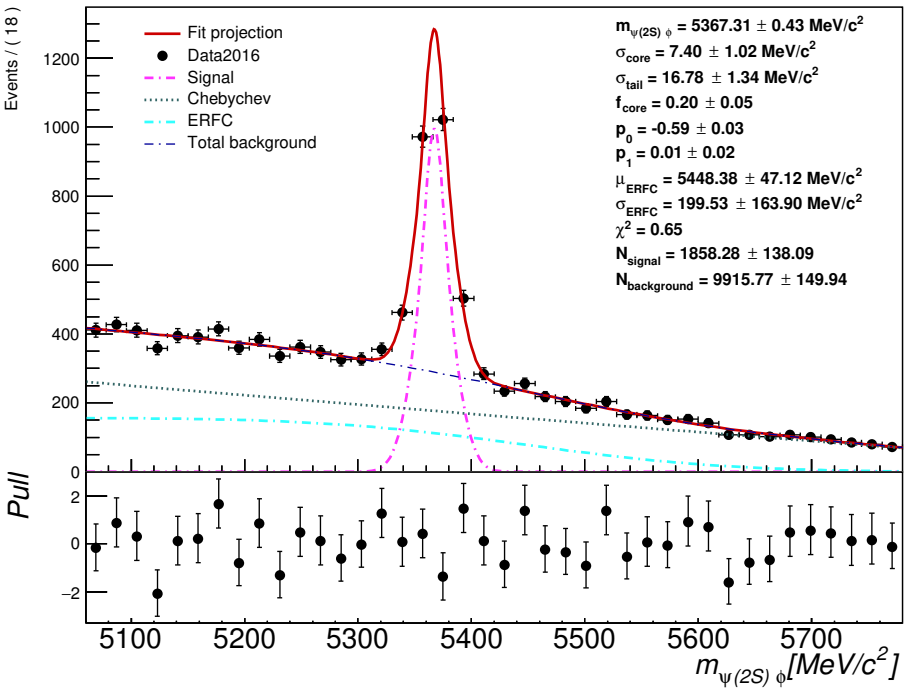

Figure 7.6: $B_s^0 \to \psi(2S)\phi$ mode

	$B_s^0 \to J/\psi\phi$	$B_s^0 \to \psi(2S)\phi$
$m_{\psi\phi}$ [MeV/c^2]	5367.12 ± 0.22	5367.31 ± 0.43
σ_c [MeV/c^2]	17.02 ± 0.65	7.40 ± 1.02
σ_t [MeV/c^2]	41.82 ± 2.69	16.78 ± 1.34
f_c	0.53 ± 0.04	0.20 ± 0.05
p_0	-0.72 ± 0.03	-0.59 ± 0.03
p_1	0.01 ± 0.02	0.01 ± 0.02
μ_{HT} [MeV/c^2]	5237.47 ± 6.24	5448.38 ± 47.12
σ_{HT} [MeV/c^2]	42.70 ± 11.41	199.53 ± 163.90
χ^2/dof	0.91	0.65
N_{signal}	23862.56 ± 458.17	1858.28 ± 138.09
$N_{\text{background}}$	48703.61 ± 484.51	9915.77 ± 149.94

Table 7.2: Fit results for the nominal fit model on data 2016.

Again, we notice a clear difference in the resolution of the invariant-mass of the B_s^0 of the different modes. This is also predicted in the MC and is consistent with the difference in the energy released in the decay of the $B_s^0 \to J/\psi\phi$ (∼1250

MeV) mode and the $B_s^0 \to \psi(2S)\phi$ (∼660 MeV) mode [3]. The choice of fit models imposes a substantial uncertainty as the signal yield is extracted from maximizing the extended unbinned likelihood function

$$L = \prod_{i=1}^{N} \frac{N_{sig}F_{sig}(m_{\psi\phi}) + N_{back}F_{back}(m_{\psi\phi})}{N_{sig} + N_{back}} \tag{7.3}$$

where F_{sig} and F_{back} are signal and background models and N_{sig} and N_{back} denoting the number of signal and background events, and are left free in the fit. In section 7.3, different fit models are investigated to extract values for the invariant-mass and signal yield for the two modes. The fit yields a χ^2/dof of 0.91 for the J/ψ mode and 0.65 for $\psi(2S)$ and the pull distribution fluctuates around zero indicating good agreement between the data and the fit projection. The pull [57] is defined by

$$g = \frac{m^i_{\psi\phi} - m_{\psi\phi}}{\sigma^{\psi\phi}} \tag{7.4}$$

where the same notation as previous is used. Assuming that the $m^i_{\psi\phi}$ is distributed as a Gaussian around the mean $m_{\psi\phi}$ with the corresponding width $\sigma^{\psi\phi}$, it is evident that the pull g will be distributed as a standard Gaussian with unity width and a mean located at zero.

7.3 Systematic Uncertainties

The uncertainty observed in the fit model are introduced due to statistical fluctuations in the data samples. This section discusses the uncertainty arising from factors as the experimental setup, branching fraction assumptions and from the analysis method itself. Contributions to the systematic uncertainty are

7.3.1 Uncertainty on mass measurement

- **The choice of fit model**. As the N_{signal} and $N_{\text{background}}$ are left free in the fit and describing the contribution of signal model F_{signal} and background model $F_{\text{background}}$ of choice varying these models introduce different signal and background yields. This is discussed in section.

- **Momentum scale calibration** If the calibration of the momentum of the reconstructed tracks are incorrect it can lead to a shift of the mass peak. This should also be the case for the charged hadron tracks. However, in a recent

study this effect was not accounted for [58]. For the muon momentum scale we impose a relative systematic uncertainty of 0.05% [59]

7.3.2 Uncertainty on $\mathcal{B}(B_s^0 \to \psi(2S)\phi)/\mathcal{B}(B_s^0 \to J/\psi\phi)$

The different uncertainties imposed for the relative branching fraction are summarized below [60] [2].

- Branching fractions of the charmonium mesons to the dimuons.
- As the $B_s^0 \to J/\psi\phi$ and $B_s^0 \to \psi(2S)\phi$ are topologically identical the uncertainties on the muon reconstruction, vertex finding efficiency and J/ψ trigger efficiency cancel in the ratio [1].
- Systematics of the individual signal yield determinations. This is closely investigated in section 7.3.3.
- Determination of the efficiencies $\varepsilon_{J/\psi\phi}$ and $\varepsilon_{\psi(2S)\phi}$. The uncertainties of these are determined through equation (6.11) and are highly dependent on the sample size of the MC. For the $\varepsilon_{\psi(2S)\phi}$ we arrive at a higher uncertainty as the sample size is 1/10 of the size as that of the J/ψ mode.

In the ratio many systematic uncertainties cancel out such as the integrated luminosity, b quark production and fragmentation and the uncertainty due to the reconstruction of B_s^0 candidates for both modes [2].

7.3.3 Uncertainty imposed due to the choice of fit models

The signal yield N_{signal} is obtained by fitting the invariant-mass distribution and is the main contributor to the systematic uncertainty. Therefore, the choice of fit models have been thoroughly investigated.

Our nominal fit model is compared to alternative models where we require the $\chi^2/dof < 2.5$ to be considerable. As the signal and background models are uncorrelated sources of systematic uncertainties they can be interchanged independently.

The first test model have the same double Gaussian as the signal distribution F_{sig} but the background Chebychev polynomial of the first kind is combined with a hyperbolic tangent function

$$F_{back}^{HT}(m_{\psi\phi}^i) = \tanh\big(\frac{m_{\psi\phi}^i - \mu_{HT}}{\sigma_{HT}}\big) \tag{7.5}$$

to form

$$F^{I}_{back}(m_{\psi\phi}) = f_{back}F^{HT}_{back}(m_{\psi\phi}) + (1 - f_{back}F^{Chev}_{back}(m_{\psi\phi})) \tag{7.6}$$

where F^{Chev}_{back} is defined in eq. 6.12, and F^{I}_{back} denotes the background model for test I.

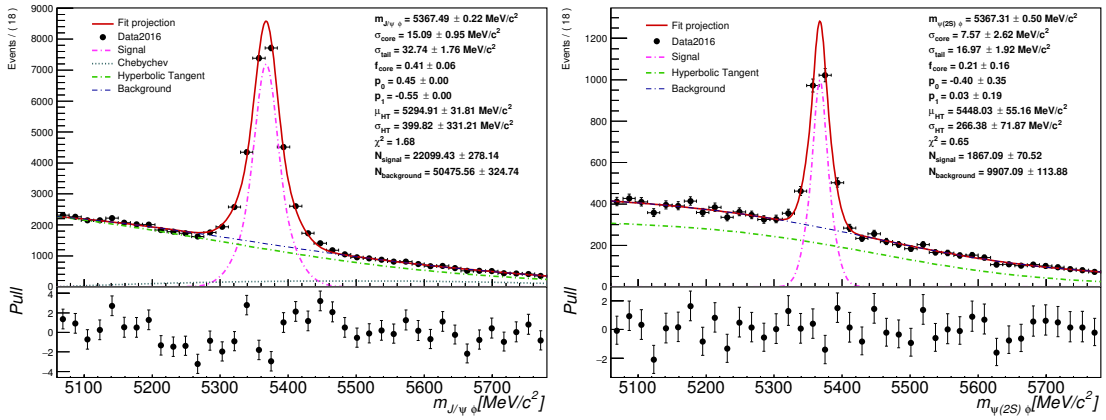

(a) $B^0_s \to J/\psi\phi$ **(b)** $B^0_s \to \psi(2S)\phi$

Figure 7.7: Model I for the invariant mass of B^0_s fitted on data 2016. The green dotted line represent the hyperbolic tangent fit and the background is represented by the blue line.

The fit for model I are shown in figure 7.7 yielding the following fit results.

	$B^0_s \to J/\psi\phi$	$B^0_s \to \psi(2S)\phi$
$m_{\psi\phi}$ [MeV/c^2]	5367.49 ± 0.22	5367.31 ± 0.50
σ_c [MeV/c^2]	15.09 ± 0.95	7.57 ± 2.62
σ_t [MeV/c^2]	32.74 ± 1.76	16.97 ± 1.92
f_c	0.41 ± 0.01	0.21 ± 0.16
p_0	0.45 ± 0.00	-0.40 ± 0.35
p_1	-0.55 ± 0.00	0.03 ± 0.19
μ_{HT} [MeV/c^2]	5294.91 ± 31.81	5448.03 ± 55.16
σ_{HT} [MeV/c^2]	399.82 ± 331.21	266.38 ± 71.87
χ^2/dof	1.68	0.65
N_{signal}	22099.43 ± 278.14	1867.09 ± 70.52
$N_{\text{background}}$	50475.56 ± 324.74	9907.09 ± 113.88

Table 7.3: Fit results for model I on data 2016.

It is evident, especially for the $\psi(2S)$ mode, that this model imposes a better

χ^2/dof. It estimates a slightly lower signal yield for both the J/ψ mode and slightly higher for the $\psi(2S)$ mode.

Next we investigate model II where the signal distribution is the same double Gaussians constrained to a common mean as the nominal fit model and the background model is simply a second order Chebychev polynomial of the first kind. This is the background model briefly discussed in section 6.4.4 being the fit yielding the best χ^2 distribution for the residual Monte Carlo simulated background events for the J/ψ mode.

$$F_{back}^{II}(m_{\psi\phi}) = F_{back}^{chev}(m_{\psi\phi}) \tag{7.7}$$

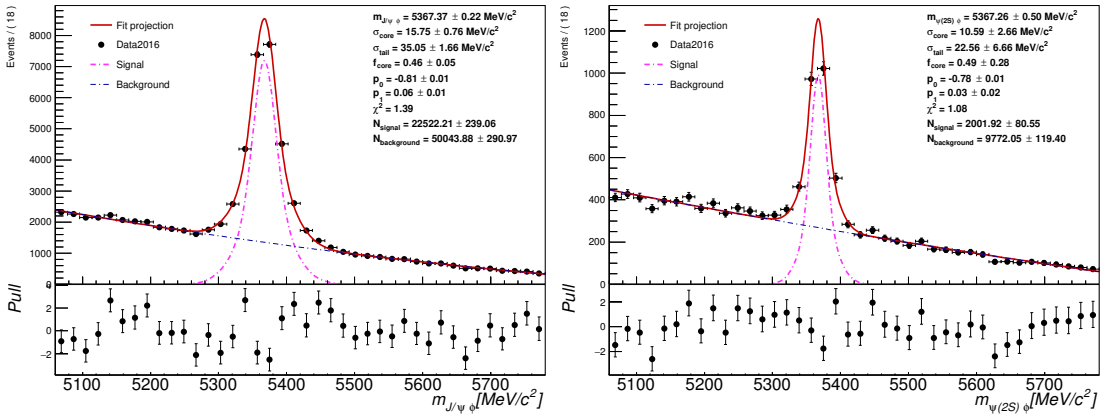

(a) $B_s^0 \to J/\psi\phi$ **(b)** $B_s^0 \to \psi(2S)\phi$

Figure 7.8: Model II for the invariant mass of B_s^0 fitted on data 2016.

The fit for model II are shown in figure 7.8 yielding the following fit results.

	$B_s^0 \to J/\psi\phi$	$B_s^0 \to \psi(2S)\phi$
$m_{J/\psi\phi}$ [MeV/c^2]	5367.37 ± 0.22	5367.26 ± 0.50
σ_c [MeV/c^2]	15.75 ± 0.76	10.59 ± 2.66
σ_t [MeV/c^2]	35.05 ± 1.66	22.56 ± 6.66
f_c	0.46 ± 0.05	0.49 ± 0.28
p_0	-0.81 ± 0.01	-0.78 ± 0.01
p_1	0.06 ± 0.01	0.03 ± 0.02
χ^2/dof	1.39	1.08
N_{signal}	22522.21 ± 239.06	2001.92 ± 80.55
N_{back}	50043.88 ± 290.7	9772.05 ± 119.40

Table 7.4: Fit results for model II on data 2016.

The background model obtained from MC shows to be in rather well agreement with the data having a χ^2/dof of 1.39 and 1.08 for the J/ψ and $\psi(2S)$ mode, respectively. It seems to underestimate the amount of signal events for the J/ψ mode, but overestimates the signal yield for the $\psi(2S)$ mode.

At last, we alter only the signal model, previously described by the double Gaussians, and replace it by a triple Gaussian function given by

$$F_{sig}^{III}(m_{\psi\phi}^i) = f_{\mathrm{c}} G_{\mathrm{c}}(m_{\psi\phi}^i) + f_{\mathrm{c}2} G_{\mathrm{c}2}(m_{\psi\phi}^i) + (1 - f_{\mathrm{c}} - f_{\mathrm{c}2}) G_{\mathrm{t}}(m_{\psi\phi}^i) \tag{7.8}$$

The background model is the same as the one for the nominal model. A test model with the use of a single Gaussian was tested, however, it does not give a proper description of the distribution. The following fit projection is obtained for model III. With the same notation as before.

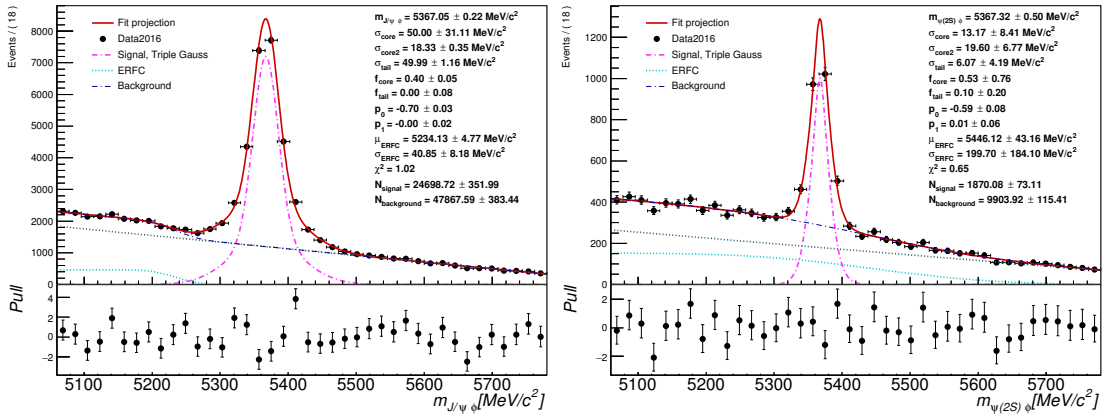

(a) $B_s^0 \to J/\psi\phi$ **(b)** $B_s^0 \to \psi(2S)\phi$

Figure 7.9: Model III for the invariant mass of B_s^0 fitted on data 2016.

The fit for model III is shown in figure 7.9 yielding the following fit results.

	$B_s^0 \to J/\psi\phi$	$B_s^0 \to \psi(2S)\phi$
$m_{J/\psi\phi}$ [MeV/c^2]	5367.05 ± 0.22	5367.32 ± 0.50
σ_c [MeV/c^2]	50.00 ± 31.11	13.17 ± 8.41
σ_{c2} [MeV/c^2]	18.33 ± 0.35	19.60 ± 6.77
σ_t [MeV/c^2]	49.99 ± 1.16	6.07 ± 4.19
f_c	0.40 ± 0.05	0.53 ± 0.76
f_t	0.00 ± 0.08	0.10 ± 0.20
p_0	-0.70 ± 0.03	-0.78 ± 0.01
p_1	-0.00 ± 0.021	-0.59 ± 0.08
μ_{ERFC}	5234.13 ± 4.77	5446.12 ± 43.16
σ_{ERFC}	40.85 ± 8.18	199.70 ± 184.10
χ^2/dof	1.02	0.65
N_{signal}	24698.72 ± 351.99	1870.08 ± 73.11
N_{back}	47867.59 ± 383.44	9903.92 ± 115.41

Table 7.5: Fit results for model III on data 2016.

Model III seems to be in good agreement with the nominal fit model. This overestimates the signal yield for both modes with respect to the nominal model. A test was also performed by using a Crystal Ball function, however, an asymmetric signal fit does not seem to be a proper description of the resonance. See the appendix for this fit.

The relative systematic uncertainty in the signal yields and invariant mass estimate is investigated by the comparing the nominal model, model I, II and III. The relative yield difference is estimated by

$$\frac{\Delta N_{B_s^0}}{N_{B_s^0}^{Nominal}} = \frac{N_{B_s^0}^{Test} - N_{B_s^0}^{Nominal}}{N_{B_s^0}^{Nominal}} \tag{7.9}$$

where $N_{B_s^0}^{Test}$ refers to the estimated signal yield obtained from the test models, while $N_{B_s^0}^{Nominal}$ is the signal yield from the nominal model from section 6.4.4. The relative mass difference is estimated in a similar manner. Table 7.6 and 7.7 summarizes the relative yield differences due to the choice of fit models for the J/ψ and $\psi(2S)$ mode.

$$\frac{\Delta m_{B_s^0}}{m_{B_s^0}^{Nominal}} = \frac{m_{B_s^0}^{Test} - m_{B_s^0}^{Nominal}}{m_{B_s^0}^{Nominal}} \tag{7.10}$$

With the same notation as for the signal yield difference. The relative differences

are listed as systematic uncertainties.

Model		$N_{B_s^0}$	$\Delta N_{B_s^0}$	$\frac{\Delta N_{B_s^0}}{N_{B_s^0}^{Nominal}}$	χ^2/dof
Nominal		23862.56	-	-	0.91
Background	Test Model I	22099.44	-1763.12	-7.4%	1.68
	Test Model II	22522.21	-1340.35	-5.6%	1.39
Signal	Test Model III	24698.72	836.16	3.5%	1.02

Table 7.6: Signal yield difference due to choice of fit models for $B_s^0 \to J/\psi\phi$ on data 2016.

Model		$N_{B_s^0}$	$\Delta N_{B_s^0}$	$\frac{\Delta N_{B_s^0}}{N_{B_s^0}^{Nominal}}$	χ^2/dof
Nominal		1858.28	-	-	0.65
Background	Test Model I	1867.09	8.81	0.5%	0.65
	Test Model II	2001.92	143.64	7.7%	1.08
Signal	Test Model III	1870.08	11.8	0.64%	0.65

Table 7.7: Signal yield difference due to choice of fit models for $B_s^0 \to \psi(2S)\phi$ on data 2016.

In table 7.6 and 7.7 we can see the signal yield, yield difference and relative yield difference as well as the goodness-of-fit χ^2/dof for the J/ψ mode and $\psi(2S)$ mode respectively, for each model. In order to obtain the systematic uncertainty for the signal yield introduced due to the choice of fit model, we take the largest estimated relative uncertainty amongst the background models, test model I and II, and add it in quadrature with relative uncertainty for the signal model, test model III.

For the $B_s^0 \to J/\psi\phi$ channel this contribution is 8.19% and for the $B_s^0 \to \psi(2S)\phi$ channel we obtain 7.73%.

Model		$m_{B_s^0}$ [MeV/c^2]	$\Delta m_{B_s^0}$ [MeV/c^2]	$\frac{\Delta m_{B_s^0}}{m_{B_s^0}^{Nominal}}$ [MeV/c^2]
Nominal		5367.12 ± 0.22	-	-
Background	Test Model I	5367.49 ± 0.22	0.37	0.007%
	Test Model II	5367.37 ± 0.22	-0.25	-0.005%
Signal	Test Model III	5367.05 ± 0.22	-0.07	-0.001%

Table 7.8: Mass difference due to choice of fit models for $B_s^0 \to J/\psi\phi$ on data 2016.

Model		$m_{B_s^0}$ [MeV/c^2]	$\Delta m_{B_s^0}$ [MeV/c^2]	$\frac{\Delta m_{B_s^0}}{m_{B_s^0}^{Nominal}}$ [MeV/c^2]
Nominal		5367.31 ± 0.43	-	-
Background	Test Model I	5367.31 ± 0.50	0	0%
	Test Model II	5367.26 ± 0.50	-0.05	0.001%
Signal	Test Model III	5367.32 ± 0.50	0.01	0.002‰

Table 7.9: Mass difference due to choice of fit models for $B_s^0 \to \psi(2S)\phi$ on data 2016.

In table 7.8 and table 7.9 the invariant mass estimation, mass difference yield and relative uncertainty for each model is shown for the J/ψ and $\psi(2S)$ mode, respectively. Several different signal, *e.g.* Breit-Wigner and Gaussian contributions, Crystal Ball (see appendix), double Crystal Ball, PDFs have also been evaluated, however these are not included in the systematic uncertainty as they fail to describe the data properly and are therefore not included.

The total systematic uncertainty due to the choice of fit models used for the mass measurement are shown in table 7.10

Source	Relative Uncertainty
Fit Model for J/ψ mode	0.007%
Fit Model for $\psi(2S)$ mode	0.001%
Momentum Scale	0.050%

Table 7.10: Systematic uncertainties for the mass measurement.

Yielding a combined relative uncertainty of 0.051% for the J/ψ mode and 0.050% for the $\psi(2S)$ mode. The relative uncertainties present in the calculation of the relative branching fraction is shown in table 7.11.

	Source		Relative Uncertainty
Systematic	Branching fractions	$\sigma_{\mathscr{B}_{J/\psi\phi}}/\mathscr{B}_{J/\psi\phi}$	0.55%
		$\sigma_{\mathscr{B}_{\psi(2S)\phi}}/\mathscr{B}_{\psi(2S)\phi}$	11.39%
	Signal Yield	$\sigma_{N_{J/\psi\phi}}/N_{J/\psi\phi}$	8.19%
		$\sigma_{N_{\psi(2S)\phi}}/N_{\psi(2S)\phi}$	7.73%
	Efficiency	$\sigma_{\varepsilon_{J/\psi\phi}}/\varepsilon_{J/\psi\phi}$	0.07%
		$\sigma_{\varepsilon_{\psi(2S)\phi}}/\varepsilon_{\psi(2S)\phi}$	0.24%
Statistical	Signal Yield	$\sigma_{N_{J/\psi\phi}}/N_{J/\psi\phi}$	2.03%
		$\sigma_{N_{\psi(2S)\phi}}/N_{\psi(2S)\phi}$	7.43%

Table 7.11: Systematic uncertainties for the relative branching fraction measurement

The total relative systematic uncertainty for the two modes are 8.21% for the J/ψ mode and 13.77% for the J/ψ mode. The signal yield for these two modes are $N_{J/\psi\phi} = 23863 \pm 458(\text{stat}) \pm 1952(\text{syst})$ and $N_{\psi(2S)\phi} = 1858 \pm 138(\text{stat}) \pm 144(\text{syst})$.

7.4 Mass Measurement of B_s^0

From the nominal fit model we extract a mass for the $B_s^0 \to J/\psi\phi$ and $B_s^0 \to \psi(2S)\phi$ mode shown below. The systematic uncertainty are 0.051% for the J/ψ mode and 0.050%.

Decay mode	$m_{B_s^0}$ [MeV/c^2]	Combined Mass Estimate [MeV/c^2]
$B_s^0 \to J/\psi\phi$	$5367.12 \pm 0.22(\text{stat}) \pm 2.74(\text{syst})$	$5367.22 \pm 0.24(\text{stat}) \pm 1.92(\text{syst})$
$B_s^0 \to \psi(2S)\phi$	$5367.31 \pm 0.43(\text{stat}) \pm 2.68(\text{syst})$	

Table 7.12: Summary of the mass measurement

This is in good agreement with the world average of $m_{B_s^0} = 5366.84 \pm 0.30$ MeV/c^2 stated by the Particle Data Group [8]. The combined mass values were estimated by the use of methods outlined in [61], [62] and [63].

7.5 Determination of the Relative Branching fraction

In this section we present the relative branching fraction given in equation 7.1 along with the systematic and statistical uncertainties. The efficiency obtained from MC studies yield the following values $\varepsilon_{J/\psi\phi} = 14.70\% \pm 0.01\%(\text{stat})$ $\varepsilon_{\psi(2S)\phi} = 15.63\% \pm 0.04\%(\text{stat})$. The signal yield obtained from the BPhysDelayed stream with a luminosity of xx fb^{-1} is $N_{J/\psi\phi} = 23863 \pm 458(\text{stat}) \pm 1952(\text{syst})$ and $N_{\psi(2S)\phi} = 1858 \pm 138(\text{stat}) \pm 144(\text{syst})$ signal events. The world averages for the charmonium branching fractions are $\mathscr{B}(J/\psi \to \mu^+\mu^-) = 5.96\% \pm 0.03\%(\text{syst})$ and $\mathscr{B}(\psi(2S) \to \mu^+\mu^-) = 0.79\% \pm 0.09\%(\text{syst})$ [8]. With these values we measure a relative branching fraction for the $B_s^0 \to \psi(2S)\phi$ over $B_s^0 \to J/\psi\phi$ of

$$\frac{\mathscr{B}(B_s^0 \to \psi(2S)\phi)}{\mathscr{B}(B_s^0 \to J/\psi\phi)} = 0.55 \pm 0.04(\text{stat}) \pm 0.09(\text{syst}) \tag{7.11}$$

A large contribution to the systematic uncertainty arises from the branching fraction $\mathscr{B}(\psi(2S) \to \mu^+\mu^-)$. The first uncertainty is due to the statistical uncertainty and the latter is due to the systematic uncertainty. This ratio has been also been measured by the CDF II [1] in 2006, the D0 experiment [2], both at the Fermilab Tevtron, and by the LHCb collaboration in 2012 [3]. The measurements are presented in the table measurements seem to be in good agreement with the measured values from the experiments shown in table 7.13 below.

Experiment	$\mathscr{B}(B_s^0 \to \psi(2S)\phi)/\mathscr{B}(B_s^0 \to J/\psi\phi)$	$\sqrt{s}$
CDF II	$0.52 \pm 0.13(\text{stat}) \pm 0.04(\text{syst}) \pm 0.06(\text{BR})$	1.96 TeV
D0	$0.53 \pm 0.10(\text{stat}) \pm 0.07(\text{syst}) \pm 0.06(\text{BR})$	
LHCb	$0.489 \pm 0.026(\text{stat}) \pm 0.021(\text{syst}) \pm 0.012(\text{BR})$	8 TeV
Our Measurement	$0.55 \pm 0.04(\text{stat}) \pm 0.09(\text{syst})$	13 TeV

Table 7.13: Measurements of the relative branching fractions. BR denotes the uncertainty due to the ratio of the branching fraction of $J/\psi \to \mu^+\mu^-$ and $\psi(2S) \to \mu^+\mu^-$.

Using this result, we can also obtain the branching fraction for the $B_s^0 \to \psi(2S)\phi$ mode by multiplying equation 7.11 by the branching of $B_s^0 \to J/\psi\phi$ giving

$$\mathscr{B}(B_s^0 \to \psi(2S)\phi) = (5.94 \pm 0.43(\text{stat}) \pm 1.06(\text{syst})) \cdot 10^{-4} \tag{7.12}$$

being in rather good agreement with the current world average of $\mathscr{B}(B_s^0 \to \psi(2S)\phi) = (5.4 \pm 0.6) \cdot 10^{-4}$ [8].

7.6 Future work

Due to the limited residual statistics of the simulated Monte Carlo background samples, we determined the optimal cuts of the observables, outlined in section 6.4, and extracted a background model by the use of data sidebands. The trigger we chose to use was the `HLT_mu6_mu4_bJpsimumu_delayed` in imposing a requirement on the transverse momentum $p_T > 4$ GeV/c and $p_T > 6$ GeV/c on the dimuons. By the use of this trigger and the selection criteria, viewed in table 6.9 we obtain a selection efficiency of $14.70\% \pm 0.01\%$ and $15.63\% \pm 0.04\%$. Just recently, we discovered that this trigger was heavily prescaled and thus only gathered a total of 4.08 fb^{-1}. Another trigger was tested, `HLT_2mu6_bJpsimumu_delayed`, imposing a cut of $p_T > 6$ GeV/c for both muons. After applying all the new selection criteria[1] after the introduction of this new trigger the total efficiency after all cuts were 7.2% and 7.8% for the $\psi(2S)$ mode and J/ψ mode, respectively. However, this trigger was not prescaled and therefore having a luminosity of 26.4 fb^{-1}. Even if the overall efficiency is much lower, the signal yield was measured to be roughly 3.3-3.5 times higher due to the increase in the integrated luminosity. However, due to time constraints, a thorough systematic error analysis was not performed and hence we decided to stay with the original trigger. See the appendix for the distribution with the use of `HLT_2mu6_bJpsimumu_delayed` trigger.

It would also have been interesting to perform measurements in different pseudorapidity regions, especially in the barrel-barrel region due to the improved resolution, and see how this affects the result of the relative branching fraction. In the attachment the invariant-mass distribution of the B_s^0 in the barrel-barrel region are shown.

[1] The 3 σ signal regions were altered and new optimization cuts obtained. The whole analysis was redone with the use of this trigger except evaluating the systematic errors, as time could not be found.

Chapter 8

Conclusion

In this thesis we present the measurement of the relative branching fraction of the two decay channels $B_s^0 \to \psi(2S)\phi$ and $B_s^0 \to J/\psi\phi$. The analysis uses Run-2 data collected by the ATLAS detector with a center-of-mass energy of $\sqrt{s} = 13$ TeV with a luminosity of 4.08 fb^{-1}. Through the study of centrally produced Monte Carlo signal samples for the two decays of interest, we determine selection criteria through the optimization, extract fit models and the efficiency ratio $\varepsilon_{J/\psi\phi}/\varepsilon_{\psi(2S)\phi}$ through truth-matched events. When this is completed, the study on actual data is performed. The selection criteria obtained from the MC study is then applied to the full dataset. Due to time constraints only the BPhysDelayed stream has been investigated.

Mass estimation using the nominal fit model and three test models to determine the systematic uncertainty for the B_s^0 has been performed for the two decay modes yielding a combined averaged result of $m_{B_s^0} = 5367.22 \pm 0.24(\text{stat}) \pm 1.92(\text{syst})$ MeV/c^2. This estimate is in well agreement with the world average stated by the Particle Data Group. Making use of the obtained signal yields through the nominal fit model, effiency ratio and world average values of the branching fractions of charmonium mesons to di-muon, we determine the following relative branching fraction

$$\frac{\mathscr{B}(B_s^0 \to \psi(2S)\phi)}{\mathscr{B}(B_s^0 \to J/\psi\phi)} = 0.55 \pm 0.04(\text{stat}) \pm 0.09(\text{syst}) \tag{8.1}$$

being in good agreement by measurements performed by the CDF II, D0 and LHCb experiment.

Bibliography

[1] CDF Collaboration. Observation of Bs to Psi(2S)phi and Measurement of Ratio of Branching Fractions $\mathscr{B}(B_s^0 \to \psi(2S)\phi)/\mathscr{B}(B_s^0 \to J/\psi\phi)$. 2 2006.

[2] V. M. Abazov and others. Relative rates of B meson decays into $\psi(2S)$ and J/ψ mesons. *Physical Review D*, 79(11):111102, 6 2009.

[3] LHCb Collaboration. Measurement of relative branching fractions of B decays to $\psi(2S)$ and J/ψ mesons. 5 2012.

[4] Wikimedia Commons. Mexican hat potential polar with details. File:Mexican hat potential polar with details.svg - Wikimedia Commons. `https://commons.wikimedia.org/wiki/File:Mexican_hat_potential_polar_with_details.svg`.

[5] ATLAS Experiment - Photos. `http://atlasexperiment.org/photos/inner-detector-combined.html`, 2018.

[6] Joao Pequenao. Computer Generated image of the ATLAS calorimeter. `https://cds.cern.ch/record/1095927`, 3 2008.

[7] E. Diehl and for the ATLAS muon collaboration. ATLAS Muon Detector Commissioning. 10 2009.

[8] J. Bertinger and others. Particle Data Group. Particle Physics Booklet. *Physical Review D*, 2017.

[9] Carl D. Anderson. The Positive Electron. *Physical Review*, 43(6):491–494, 3 1933.

[10] CDF Collaboration. Observation of $B_s^0 - \overline{B_s^0}$ Oscillations. 9 2006.

[11] Isard Dunietz and Ulrich Nierste. In pursuit of new physics with B_s^0 decays. *Physical Review D*, 63(11):114015, 2001.

[12] Rene Bruna and Fons Rademakersh. ROOT -An object oriented data analysis framework. *Nuclear Instruments and Methods in Physics Research A*, 389:81–86, 1997.

[13] J. J. Thomson. XL. Cathode Rays. *The London, Edinburgh, and Dublin Philosophical Magazine and Journal of Science*, 44(269):293–316, 10 1897.

[14] E. Rutherford. The scattering of α and β particles by matter and the structure of the atom. *The London, Edinburgh, and Dublin Philosophical Magazine and Journal of Science*, 21(125):669–688, 5 1911.

[15] J. Chadwick. The Existence of a Neutron. *Proceedings of the Royal Society A: Mathematical, Physical and Engineering Sciences*, 136(830):692–708, 6 1932.

[16] Max Planck. Treatise on Thermodynamics. `https://books.google.no/books?id=r4sJAAAAIAAJ&printsec=frontcover&dq=Treatise+on+Thermodynamics&redir_esc=y`, 1903.

[17] Albert Einstein. On a Heuristic Point of View about the Creation and Conversion of Light. *Annalen der Physik*, 17:132–148, 1905.

[18] G Rajasekaran. The story of the neutrino. 2016.

[19] P. A. M. Dirac. The Quantum Theory of the Electron. *Proceedings of the Royal Society A: Mathematical, Physical and Engineering Sciences*, 117(778):610–624, 2 1928.

[20] A. Einstein. Zur Elektrodynamik bewegter Körper. *Annalen der Physik*, 322(10):891–921, 1905.

[21] M Gell-Mann. The Eightfoldway; A theory of strong interaction symmetry. Technical report, Divison of Technical Information Extension, U.S. Atomic Energy Commission, 3 1961.

[22] G. Zweig. An SU3 model for strong interaction symmetry and its breaking. 8182/TH.401, 1964.

[23] David J. (David Jeffery) Griffiths. *Introduction to elementary particles*. Wiley-VCH, 2008.

[24] F Mandl and G Shaw. *Quantum Field Theory*. 2010.

[25] Xianhao Xin. Glashow-Weinberg-Salam Model: An Example of Electroweak Symmetry Breaking. 2007.

[26] Peter W. Higgs. Broken Symmetries and the Masses of Gauge Bosons. *Physical Review Letters*, 13(16):508–509, 10 1964.

[27] F. Englert and R. Brout. Broken Symmetry and the Mass of Gauge Vector Mesons. *Physical Review Letters*, 13(9):321–323, 8 1964.

[28] The Nobel Prize in Physics 2013. `https://www.nobelprize.org/nobel_prizes/physics/laureates/2013/`.

[29] Makoto Kobayashi and Toshihide Maskawa. CP -Violation in the Renormalizable Theory of Weak Interaction. *Progress of Theoretical Physics*, 49(2):652–657, 2 1973.

[30] Nicola Cabibbo. Unitary Symmetry and Leptonic Decays. *Physical Review Letters*, 10(12):531–533, 6 1963.

[31] ATLAS ATLAS Collaboration. Measurement of the CP-violating phase ϕ_s and the B_s^0 meson decay width difference with $B_s^0 \to J/\psi\phi$ decays in ATLAS. 1 2016.

[32] Sheldon Stone and Liming Zhang. S-waves and the Measurement of CP Violating Phases in Bs Decays. 12 2008.

[33] D Deboy, R W Assmann, F Burkart, M Cauchi, and D Wollmann. Acoustic measurements at LHC collimators -Overview and First Results.

[34] ATLAS. Luminosity Public Results Run2. `https://twiki.cern.ch/twiki/bin/view/AtlasPublic/LuminosityPublicResultsRun2`, 2017.

[35] G. et al. Aad. The ATLAS Experiment at the CERN Large Hadron Collider. *Journal of Instrumentation*, 2008.

[36] K. (Konrad) Kleinknecht. *Detectors for particle radiation*. Cambridge University Press, 1998.

[37] Matthias Neubert. Introduction to B physics. *Arxiv preprint hep-ph/0001334*, (January):0–52, 2000.

[38] Frederic Deliot. Top Quark Physics At Hadron Colliders. 11 2011.

[39] Adam F Falk. Introduction to Hadronic B Physics Published as Chapter 2 of The BaBar Physics Book – Physics at an Asymmetric B Factory SLAC Report SLAC-R-504. 1998.

[40] Helen Quinn. B Physics and CP Violation. 11 2001.

[41] S J Brodsky and S Gardner. Evading the CKM Hierarchy: Intrinsic Charm in B Decays *. 2001.

[42] D Boutigny and et. al. The BABAR physics book: Physics at an asymmetric B factory. `http://inspirehep.net/record/479871/`, 1998.

[43] N. Brambilla and others. Heavy Quarkonium Physics. 12 2004.

[44] A. J. Bevan and others. The Physics of the B Factories. 6 2014.

[45] Torbjörn Sjöstrand, Stefan Ask, Jesper R. Christiansen, Richard Corke, Nishita Desai, Philip Ilten, Stephen Mrenna, Stefan Prestel, Christine O. Rasmussen, and Peter Z. Skands. An Introduction to PYTHIA 8.2. 10 2014.

[46] S. Agostinelli and others. Geant4—a simulation toolkit. *Nuclear Instruments and Methods in Physics Research Section A: Accelerators, Spectrometers, Detectors and Associated Equipment*, 506(3):250–303, 7 2003.

[47] I Vukotic, R W Gardner, and L A Bryant. Big Data Tools as Applied to ATLAS Event Data. 2017.

[48] James Catmore, Lukas Heinrich, Karsten Köneke, and Eric Torrence. The ATLAS data processing chain: from collisions to papers.

[49] W Verkerke and D Kirkby. RooFit Users Manual v2.91. pages 91–33, 2008.

[50] Steffen Georg Weber. Measurement of J/ψ production in pp collisions at LHC energies with ALICE. 4 2017.

[51] Antonio Salvucci. Measurement of muon momentum resolution of the ATLAS detector. 1 2012.

[52] ATLAS Collaboration. Tracking CP Recommendations for Early 2018 Analyses AtlasProtected TWiki. `https://twiki.cern.ch/twiki/bin/view/AtlasProtected/TrackingCPRecsEarly2018`.

[53] ATLAS Collaboration. ATLAS Luminosity Calculator.

[54] Justas Zalieckas. Determination of the ratio of b-quark fragmentation fractions f_s/f_d and study of the higgs boson production and couplings with the atlas detector in pp collisions. 2016.

[55] J. C. Mason and D. C. (David Christopher) Handscomb. *Chebyshev polynomials*. Chapman & Hall/CRC, 2003.

[56] S. Navas (U. Granada) P. Richardson (Durham U.) T. Sjöstrand (Lund U.) L. Garren (Fermilab), C.-J. Lin (LBNL) and T. Trippe (LBNL). 35. Monte Carlo Particle Numbering Scheme. 2009.

[57] Luc Demortier and Louis Lyons. Everything you always wanted to know about pulls. 2002.

[58] B mass reconstruction in $B^{\pm} \to J/\psi K^{\pm}$ decay at atlas at 13 tev pp collisions at the lhc.

[59] ATLAS Collaboration. Muon reconstruction performance of the ATLAS detector in proton–proton collision data at $\sqrt{s} = 13$TeV . March 2016.

[60] The LHCb collaboration. Measurement of relative branching fractions of B decays to ψ(2S) and J/ψ mesons.

[61] M.K Bugge, A.L. Read, and O.M. Røhne. Mean or average of two partially correlated measurements. *Metrologia*, 43(4):S268–S275, 8 2006.

[62] Louis Lyons, Duncan Gibaut, and Peter Clifford. How to combine correlated estimates of a single physical quantity. *Nuclear Instruments and Methods in Physics Research Section A: Accelerators, Spectrometers, Detectors and Associated Equipment*, 270(1):110–117, 7 1988.

[63] M G Cox, C Eiø, G Mana, and F Pennecchi. The generalized weighted mean of correlated quantities. *Metrologia*, 43(4):S268–S275, 8 2006.

Appendices

Appendix I

Fit Results using Crystal Ball Function

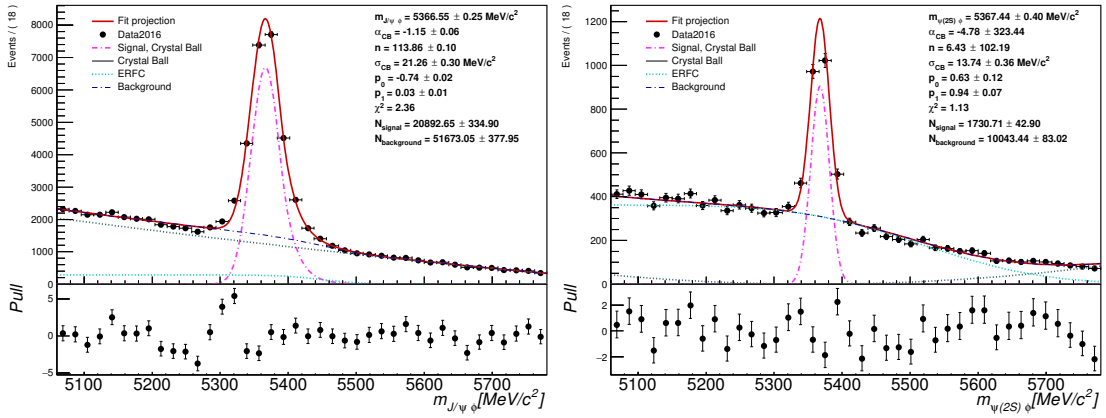

(a) $B_s^0 \to J/\psi\phi$ **(b)** $B_s^0 \to \psi(2S)\phi$

Figure 1: Fit model with the Crystal Ball function 6.8 for the signal distribution and the nominal background model describing the background distribution.

	$B_s^0 \to J/\psi\phi$	$B_s^0 \to \psi(2S)\phi$
$m_{J/\psi\phi}$ [MeV/c^2]	5366.55 ± 0.25	5367.44 ± 0.40
α_{CB}	-1.15 ± 0.05	-4.78 ± 323.44
n	113.86 ± 0.10	6.43 ± 102.19
σ_{CB}	21.26 ± 0.30	13.74 ± 0.36
p_0	-0.74 ± 0.02	0.63 ± 0.12
p_1	0.03 ± 0.01	0.94 ± 0.07
χ^2/DoF	2.36	1.36
N_{signal}	20892.65 ± 239.06	1730.71 ± 42.90
N_{back}	51673.05 ± 377.95	10043.44 ± 83.02

Table 1: Fit results extracted for the J/ψ for data 2016.

Distribution with the use of 2mu6 trigger

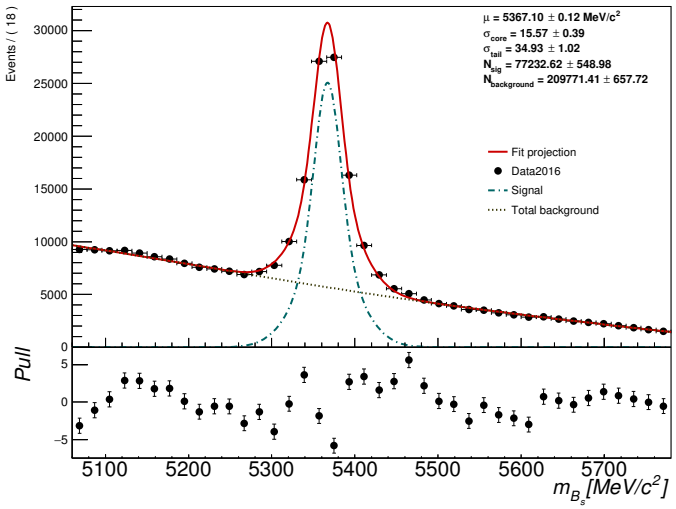

(a) $B_s^0 \to J/\psi\phi$

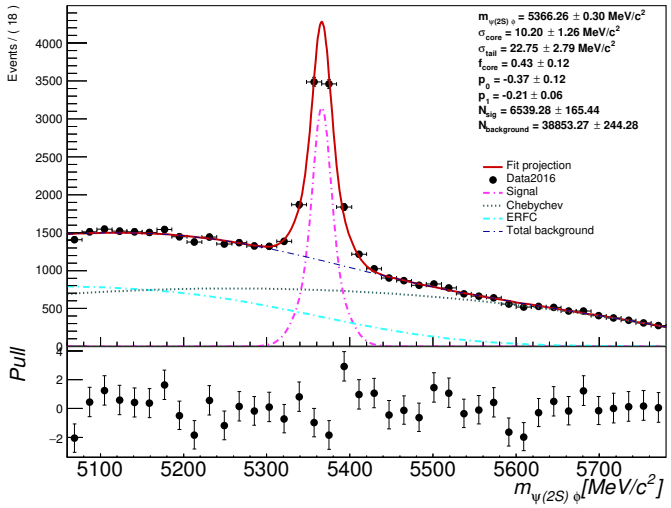

(b) $B_s^0 \to \psi(2S)\phi$

Figure 2: Invariant mass distribution of B_s^0 on data with the use of `HLT_2mu6_bJpsimumu_delayed` trigger. (a) Uses fit model II and (b) uses the nominal fit model.

Appendix II

Observables for the $\psi(2S)$ mode

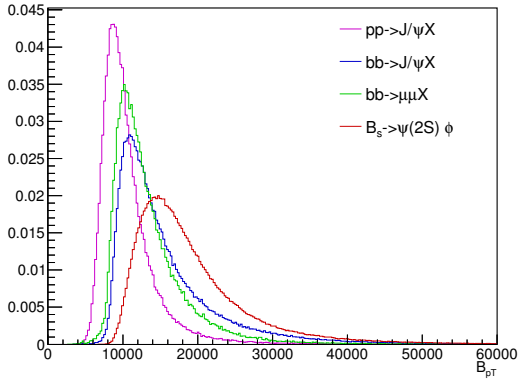

(a) Transverse momentum of the B meson

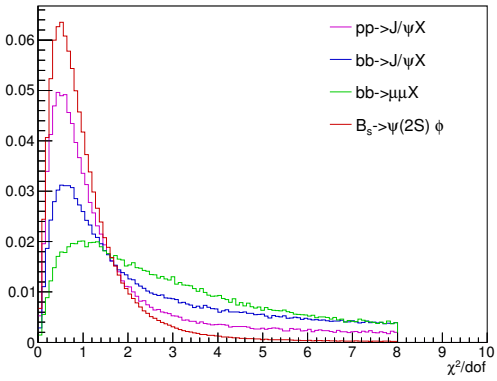

(b) Goodness-of-fit χ^2/dof

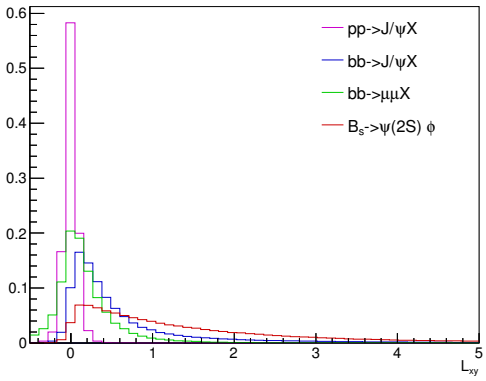

(c) Transverse decay length L_{xy}

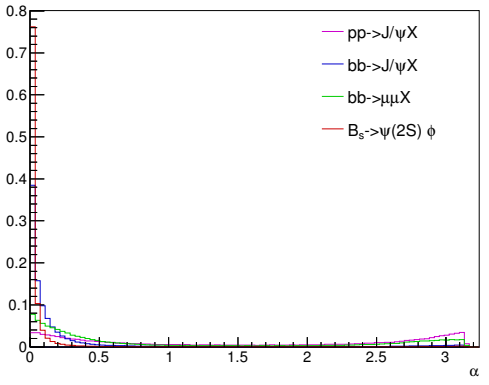

(d) Pointing angle α

Figure 3: Distribution of the observables for the Monte Carlo samples. All histograms are normalized to unity.

Fit of the invariant-mass of the B_s^0 in barrel-barrel region for data.

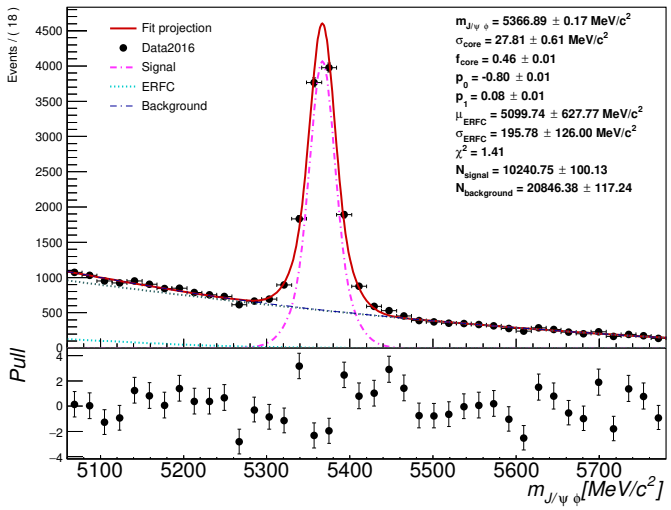

(a) $B_s^0 \to J/\psi\phi$

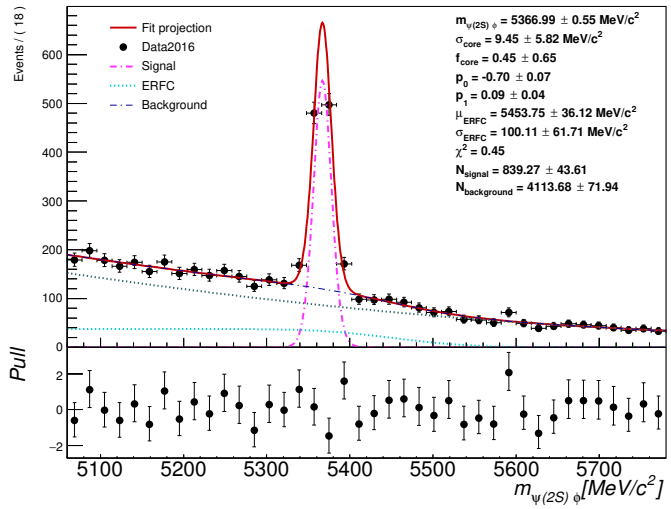

(b) $B_s^0 \to \psi(2S)\phi$

Figure 4: Fit of the invariant-mass of the B_s^0 in the barrel-barrel region. Using the nominal fit model we extract a mass fair close to the world average.

Fit of MC signal samples in EE and BB region

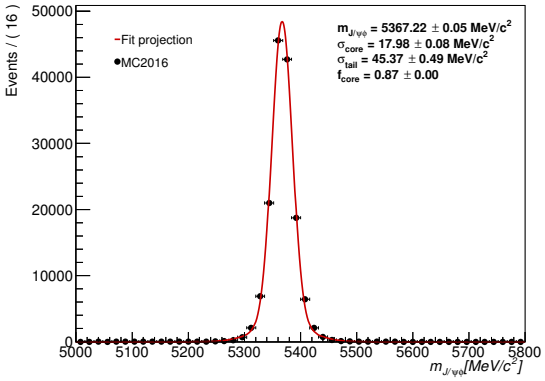

(a) Invariant B_s^0 mass with di-muon in BB region for J/ψ mode.

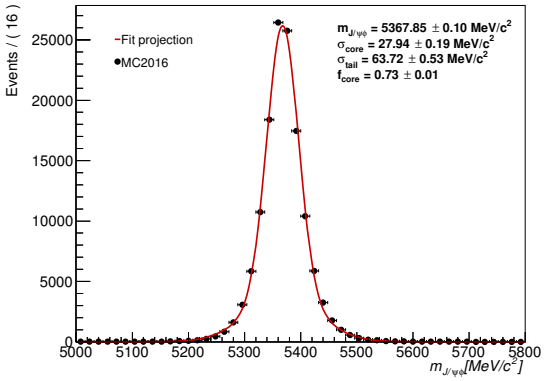

(b) Invariant B_s^0 mass with di-muon in EE region for J/ψ mode.

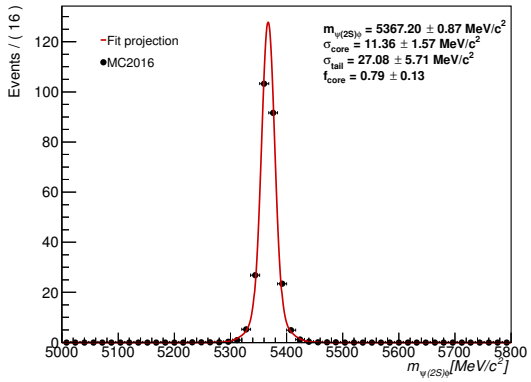

(c) Invariant B_s^0 mass with di-muon in BB region for $\psi(2S)$ mode.

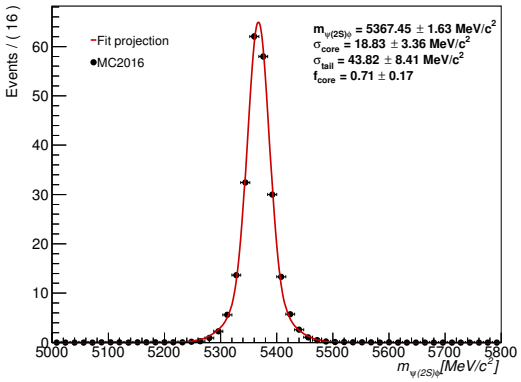

(d) Invariant B_s^0 mass with di-muon in EE region for $\psi(2S)$ mode.

Figure 5: Fit of the invariant-mass of the B_s^0 in the barrel-barrel region and in the end-cap end-cap region for both modes.